UNIVERSTITY OF OSLO

Department of Chemistry

Defects and Transport in Ba-doped $La_{27}W_5O_{55.5}$

Master Thesis in Materials, Energy and Nanotechnology

Xuemei Cui

June 2013

Preface

This thesis is based on the research work and experiments I carried out to fulfill my Master of Science degree at the Department of Chemistry, University of Oslo. The experimental work was conducted at the Center for Materials Science and Nanotechnology (SMN) during the time from August 2011 to May 2013.

I would first of all like to thank my supervisor, associate professor Reidar Haugsrud for his valuable advice and patiently, friendly guide throughout the entire period. I appreciate all the helpful support from professor Truls E.Norby.

I would like to make a grateful acknowledgement for the entire research group. I especially want to give thanks to Camilla Vigen for offering a lot help on my research work and thesis. I appreciate all the professional discussions with Anna Magraso Sola and Wen Xing. Thanks to my co-supervisor Ragnhild Hancke for your concerns during the writing time. I am grateful to Nadya for providing general help on my studies and life in Norway.

Lastly, I want to thank Xiaoqing, my “sister”. Thank you for your encouragement and cheering me up in some hard time.

University of Oslo, May 2013

Xuemei Cui

Abstract

La_6WO_{12} shows relatively high proton and mixed proton-electron conductivity and the stoichiometry is modified to $La_{28-x}W_{4+x}O_{54+1.5x}v_{2-1.5x}$ (La/W=5.3-5.7) to synthesize single phase. Acceptor doping this material may help the formation of oxygen vacancies and thus increase the transport of proton.

In this work, Ba as an acceptor is studied in attempt to substitute La site. 2% and 0.5% Ba-doped $La_{27}W_5O_{55.5}$, donated as LBaWO-2% and LBaWO-0.5%, respectively, were synthesized by wet chemical method. Following sintering, XRD, SEM and EPMA were carried out to check impurities and to study the composition. The solubility of Ba in $La_{27}W_5O_{55.5}$ was observed ~0.4%.

The conductivity was studied by AC impedance measurements in temperature range from 300 °C to 1000 °C. It shows that the conductivity of LBaWO-2% is dominated by grain boundary. The defect structure was investigated by measuring the conductivity as a function of pH_2O and pO_2. For LBaWO-0.5%, the conductivity is dominated by proton conductivity below ~700 °C under oxidizing condition, and the maximum proton conductivity is observed to be $2.3 \cdot 10^{-3}$ Scm^{-1} at 700 °C. Above ~800 °C, it exhibits mixed ionic and electronic conductivity under oxidizing condition. The effect on proton conductivity from acceptor doping is barely seen, in the contrast, the conductivity has a steeper pO_2 dependency, indicated n-type conductivity under reducing condition due to inherent $W_{La}^{\bullet\bullet\bullet\bullet}$.

Impedance spectroscope was conducted in the temperature from 200 °C to 1000 °C. LBaWO-2% (with secondary phase) and LBaWO-0.5% (relatively pure) both demonstrated huge resistive grain boundaries. Except for impurity blocking, it was suspected to be the presence of inherent space layer, which depleted the positively charged charge carriers.

Based on thermogravimetry (TG), the proton concentration as a function of the inverse temperature were modeled to obtain the standard hydration enthalpy and entropy change. The water uptake of the two samples with different doping level did not show significant change. The thermodynamics parameters are in agreement with

the values from the literature, with ΔH^0_{hydr} =~-100 kJ/mol and ΔS^0_{hydr} =~-125 J/molK for LBaWO-0.5% and with ΔH^0_{hydr}=~-125 kJ/mol and ΔS^0_{hydr}=~-140 J/molK for LBaWO-2%. Both the standard hydration enthalpy and entropy were observed to be more negative with increasing Ba doping level.

Table of Contents

1. Introduction

1.1. Background

With the development of human civilization, the worldwide energy consumption has increased drastically, especially during the recently 30-40 years. For instance, the annual worldwide energy consumption increased by 39% from 1990 to 2007, and this increase is primarily from increased fossil fuels use (the main three being oil, coal and natural gas). A finite supply of fossil fuels and CO_2 emission have been the two main problems that people have to face when being dependent on fossils fuels. First, the coal reservoirs are reported to eventually dwindle by 2112 and coal will be the only fossil fuel available after 2042[1]. Second, International Energy Agent (IEA) reported that 99% CO2 emission is from fossil fuel combustion (with 43% from coal, 36% from oil, and 20% from natural gas)[2].

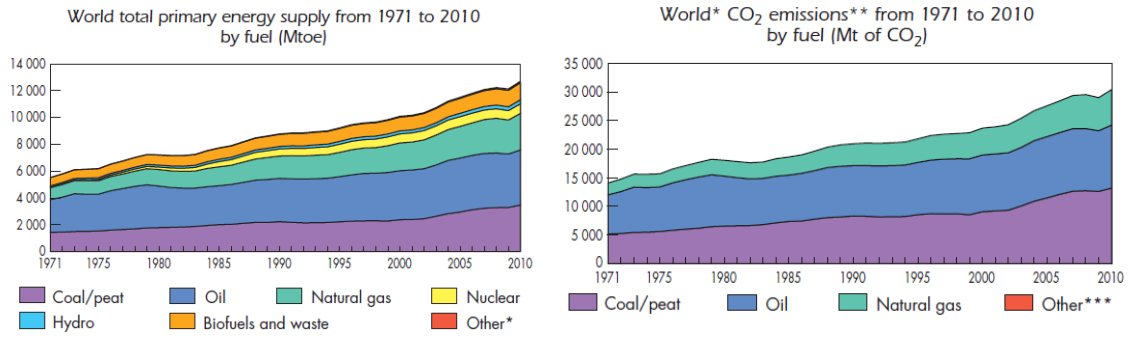

(a) (b)

Fig.1.1 (a) World energy consumption by source (b) CO_2 emission by source. Figures taken from[3].

With the global demand of increased energy supply and the urgent need to avoid the environmental deterioration from use of fossil fuels, the only way forward is to gradually replace fossil fuel as the major energy source, especially by those renewable, environmental-friendly technologies.

Many types of renewable energy resources such as power generated from the nearly infinite elements of nature will never run out, for instance, sunshine, wind, wave, tide,

geothermal heat, etc. However, none of them could keep a good balance between practicality, cost and efficiency. Therefore, these technologies are only used at a small scale so far.

Fuel cell was invented over a century ago, and it is a device that converts chemical energy from a fuel directly into electricity through electrochemical reaction with oxygen or another oxidizing agent. Fuel cells can produce electricity continuously as long as it is supplied with fuels and air. Solid oxide fuel cells (SOFCs) have attracted much attention, because they are fuel flexible and are the most efficient devices for the electrochemical conversion of chemical energy.

1.2. Solid Oxide Fuel Cells (SOFCs)

A solid oxide fuel cell consists of two solid electrodes and with a ceramic electrolyte in between. In traditional solid oxide fuel cells (Fig.1.2 (a)), oxygen (from air) is reduced to oxide ions at the cathode. These oxide ions migrate through the pure oxygen ion conducting electrolyte and react with fuel forming H_2O and/or CO_2 at the anode. Meanwhile, electrons flow from anode to cathode.

The reactions of traditional SOFCs are thus:

Cathode:

$$\frac{1}{2}O_2(g) + 2e^- \rightarrow O^{2-} \tag{1.1}$$

Anode:

$$H_2(g) + O^{2-} \rightarrow H_2O(g) + 2e^- \tag{1.2}$$

Proton conducting fuel cells (PC-SOFCs) is one type of SOFCs, it is the electrolyte which is proton conducting and making the reaction to water happen at the oxygen side. Comparing with traditional SOFCs, PC-SOFCs is with lower operation temperature[4], which is an essential advantage for reality use. The working principle is very similar as traditional SOFCs as shown in Fig.1.2 (b). Here, protons produced

from the anode diffuse through the proton conducting electrolyte to the cathode. Product water forms at cathode instead of at anode, avoiding water diluting the fuel at the anode which would decrease the efficiency of the energy convention.

The reactions of PC-SOFCs are thus:

Cathode:

$$\frac{1}{2}O_2(g) + 2e^- \rightarrow O^{2-} \tag{1.3}$$

Anode:

$$H_2(g) \rightarrow 2H^+ + 2e^- \tag{1.4}$$

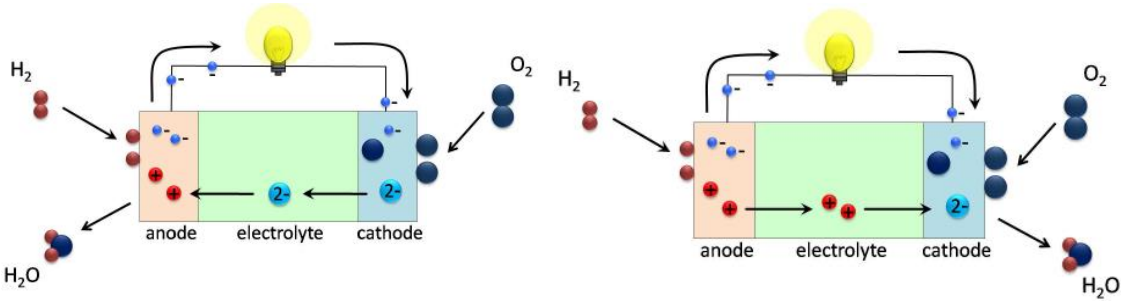

(a) (b)

Fig.1.2 Basic principle of working progress. Figures are taken from[5]. (a) for traditional SOFC. (b) for PC-SOFCs.

1.3. Objective of the thesis

A number of proton conducting materials have been studied and the most promising ones are mainly perovskite structure oxides, which exhibit high proton conductivity. However, these perovskite structure oxides face the problem of being vulnerable to CO_2 containing atmosphere. A lot of non-perovskite oxides have also been studied as promising candidates of fuel cells. Rare-earth tungstates ($REXW_YO_Z$) as one of these oxides, have also been reported to exhibit proton conductivities and be with CO2

stability. Previous works demonstrate that Ln_2WO_6 (Ln=La, Nd, Gd and Er) exhibit interesting transport properties [6-8]. Undoped La_6WO_{12} was reported to exhibit proton conductivity with ~$5 \cdot 10^{-3}$ S/cm in wet hydrogen at 900 °C by Shimura et al.[9]. Also La_6WO_{12} with stoichiometry modified to $La_{28-x}W_{4+x}O_{54+1.5}v_{2-1.5x}$ (La/W=5.3-5.7) shows proton conductivity with ~$3 \cdot 10^{-3}$ S/cm at ~800 °C. The Proton conductivity is lower than the best perovskite structured oxides. The materials in this work are based on $La_{28-x}W_{4+x}O_{54+1.5x}v_{2-1.5x}$ (La/W=5.3-5.7) and the defect structure and transport properties of Ba acceptor doped lanthanum tungstates are studied.

2. Theory

The theory of this master thesis is mainly concerned with defect chemistry and electrical measurements, also touching upon space-charge layer theory. For defect chemistry, it is including notation, formation, thermodynamics and electrochemical transport. Formation mechanisms of different defects and how they contribute to conductivity can be distinguished by measurement in different atmosphere. The underlying theory in this chapter is based on parts of Defects and Transport in Crystalline Solids by Per Kofstad and Truls Norby[10] and Electrical Measurement by Truls Norby[11].

2.1. Defect Chemistry

2.1.1. Defect in Crystalline Materials

All crystalline solids at any temperature above 0 K will contain defects and will exhibit deviations from the ideal structure. In light of dimension, defects in crystalline can be classified into point defects, line defects, planar defects and volume defects, which have 0-dimensions, 1-dimensions, 2-dimensions and 3-dimensions respectively. Point defects are where an atom is missing or is in an irregular place in the lattice structure, which include vacancies, self-interstitial atoms, interstitial foreign atoms and substitutional foreign atoms. Misalignment of ions or presence of vacancies along a line form line defects, such as dislocation. Planar defects are along a 2-dimensional surface such as grain boundaries, internal interfaces and external surfaces. Besides structural defects, crystals also contain electronic defects like electrons and electron holes. In this work, only point defects, electronic defects and grain boundaries are relevant.

2.1.2. Acceptor-and donor-doping

In material synthesis, contamination by unwanted foreign elements is always tried to avoid. The deliberate addition of carefully chose impurity to a host

material is called doping. Foreign atoms can significantly beneficially affect the materials property by introducing charged defects. Foreign atoms have the same valence as the native atom they replace are called homovalent, while, having unequal as the native atom they replace are called heterovalent or aliovalent.

Doping atoms in a host lattice with atoms with lower valence is called acceptor-doping. These foreign atoms are named acceptor, which can accept electrons form the valence band. Electrons from the full valance band can be promoted to fill the bond, leaving holes in the valence band, which contribute to the conductivity. On the Contrary, doping with higher valence is called donor-doping and. Foreign atoms here are named donor, which will give the extra electron to the conduction band.

2.1.3. Kröger-Vink notation

Today Kröger-Vink(K-V) notation[12] is the most widely adopted system to describe point defects and it describes any entity in a structure, including defects and "perfects". The K-V notation is denoted as A_s^c. The main symbol A tells what the species consist of, normally chemical element or vacancy (v). Subscript s tells which lattice site it is on, normally a chemical element occupying the lattice site in perfect crystal or interstitial site (i). Superscript c represents charge, when turning to point defects, the charge should be related with effective one. The effective charge of a species is described as: the actual charge of the species minus the actual charge that the ideal perfect structure would have had in the same structural element. Dot (•), slash (/), or an "X" are used to denote effective positive, negative, or no charge respectively. Electrons and electron holes have specified notations, which are $e^{/}$ and $h^{\bullet}$.

Point defects dissolve in the host lattice, including the introduced impurities or the inherent defects. The defect equilibrium may be treated in terms of the

thermodynamics of chemical reactions and solutions. There are three rules for writing and balancing defect chemical reaction equations as follow:

Conservation of mass – mass balance: the defect reaction must balance with respect to the mass, i.e. the number and types of atoms involved in the defect reaction must be the same before and after the defect formation or annihilation. Vacancies mean empty, which do not count and electronic defects are commonly not considered in mass balance.

Conservation of charge – charge balance: the composition should remain electrically neutral, which means that the effective charge on the left and right sides of a reaction equation must be the same.

Conservation of host structure – site ratio balance: this rule is special to defect chemistry in crystalline solids. The ratio(s) of the number of cation and anion structure sites in a crystalline compound is constant. For instance, in a compound M_2O_3 the ratio of regular cation to anion sites is 2:3, and if 3 oxygen sites are created in M_2O_3 through a defect reaction, two regular M-sites - vacant or filled - in the metal sublattice must also simultaneously be created.

2.1.4. Kröger-Vink compatible notation

Some materials are pure, unsubstituted compounds, but are still inherently disordered. For instance, the material used in this thesis is lanthanum tungstates $La_{28-x}W_{4+x}O_{54+1.5x}v_{2-1.5x}$[13], which has an incompletely filled disordered oxygen. Traditional K-V notation could not appropriately express such charge compensating defect, instead, a K-V compatible notation developed by Norby[12] is introduced to express these disordered sublattice.

In $La_{28-x}W_{4+x}O_{54+1.5x}v_{2-1.5x}$, "x" refers to W on La sites and v refers to a vacant site that can be occupied by oxygen. When x=0, it is the perfect parent structure, which contains 2 vacancies. The perfect oxygen sites are statistically occupied by 54/56 oxygen ions and 2/56 vacancies. In this case, oxygen site can be written as $\frac{54}{56}$O and

the statistical charge of this site is -108/56. Since the real charge of oxygen ion is -2, the effective charge of compatible oxygen site is: (-2)-(-108/56) = -4/56. Therefore, the compatible oxygen site can be denoted as $O_{\frac{54}{56}O}^{\frac{4}{56}/}$. In a similar way, the real charge of vacancy is 0, the effective charge of compatible oxygen vacancy is: 0-(-108/56) =108/56. Therefore, the compatible oxygen vacancy can be denoted as $v_{\frac{54}{56}O}^{\frac{108}{56}\bullet}$. In this thesis, I have chosen lanthanum tungstate with La/W=5.4, corresponding to x=1, and one unit cell is $La_{27}W_5O_{55.5}$. One W sitting on La site per unit cell, as donor: $W_{La}^{\bullet\bullet\bullet}$. The symbol notations used in this thesis are shown in Table 2.1.

Table 2.1 Kröger-Vink notation for some possible point defects.

Notation	Defect
Compatible oxygen vacancy	$v_{\frac{54}{56}O}^{\frac{108}{56}\bullet}$
Compatible oxygen site	$O_{\frac{54}{56}O}^{\frac{4}{56}/}$
Barium substitute Lanthanum	$Ba_{La}^{/}$
Tungstate substitute Lanthanum	$W_{La}^{\bullet\bullet\bullet}$
Compatible proton	$OH_{\frac{54}{56}O}^{\frac{52}{56}\bullet}$
Electron	$e^{/}$
Electron hole	$h^{\bullet}$

2.2. Defects in $La_{27}W_5O_{55.5}$

2.2.1. Defect chemical reactions with $La_{27}W_5O_{55.5}$

At low oxygen partial pressure, reduction reaction may predominate. Reduction of $La_{27}W_5O_{55.5}$, in terms of oxygen ions and fully ionized vacancies could be written as follow

$$O_{O}^{\frac{4}{56}/} = v_{O}^{\frac{108}{56}\bullet} + 2e/ + \frac{1}{2}O_2\,(g) \tag{2.1}$$

The equilibrium coefficient is accordingly

$$K_R = \frac{\left[v_{O}^{\frac{108}{56}\bullet}\right] n^2\, {p_{O_2}}^{\frac{1}{2}}}{\left[O_{O}^{\frac{4}{56}/}\right]} \tag{2.2}$$

Through the reduction reaction, the total electroneutrality now reads

$$\frac{4}{56}\left[O_{O}^{\frac{4}{56}/}\right] + n = \frac{108}{56}\left[v_{O}^{\frac{108}{56}\bullet}\right] \tag{2.3}$$

Here, we simplify the electroneutrality by regarding the electrons as minority defects

$$\frac{4}{56}\left[O_{O}^{\frac{4}{56}/}\right] \cong \frac{108}{56}\left[v_{O}^{\frac{108}{56}\bullet}\right] \tag{2.4}$$

By inserting this into the equilibrium coefficient, we obtain

$$K_R = \frac{1}{27}\, n^2 {p_{O_2}}^{\frac{1}{2}} \tag{2.5}$$

$$n = (27K_R)^{\frac{1}{2}} {p_{O_2}}^{-\frac{1}{4}} \tag{2.6}$$

In a similar way, at high oxygen partial pressure, oxidation reaction may predominate

$$\frac{1}{2}O_2(g) + v_{O}^{\frac{108}{56}\bullet} = O_{O}^{\frac{4}{56}/} + 2h^{\bullet} \tag{2.7}$$

$$K_O = \frac{\left[O_{O}^{\frac{4}{56}/}\right] P^2}{\left[v_{O}^{\frac{108}{56}\bullet}\right] {p_{O_2}}^{\frac{1}{2}}} \tag{2.8}$$

Here, we take electron holes as minority defects, therefore, after simplification, the electroneutrality is the same as Eq.(2.4). The concentration of electron holes can be obtained

$$P = \left(\frac{1}{27} K_O\right)^{\frac{1}{2}} {p_{O_2}}^{\frac{1}{4}} \tag{2.9}$$

The Brouwer diagram based on the calculation above represents the concentration of the defects involved as a function of oxygen partial pressure. In this case, there is one W sitting on La site per unit cell, yielding 1per formula unit, which is higher than the concentration of oxygen vacancies (0.5 per formula unit) and lower than the concentration of oxygen on oxygen site (55.5 per formula unit) . As an inherent donor, $[W_{La}^{\bullet\bullet\bullet}]$ does not affect the native defect equilibrium and is constant as function of pO_2 as shown in the Brouwer diagram.

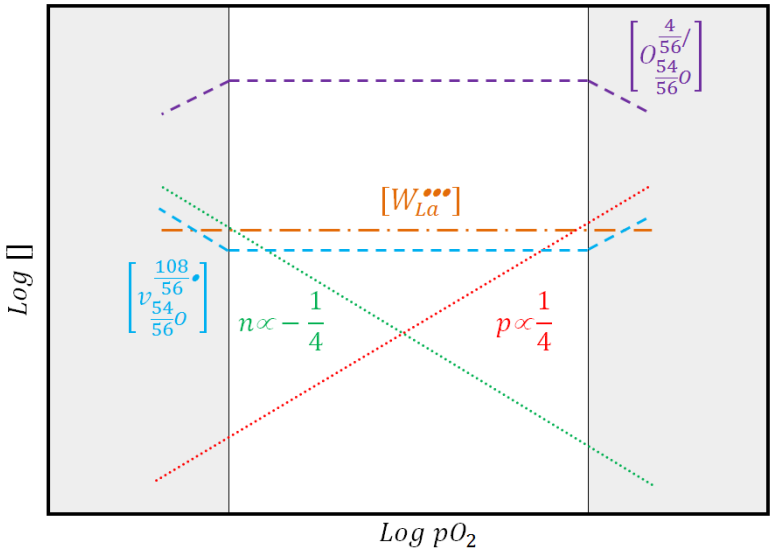

Fig.2.1 Brouwer Diagram of $La_{27}W_5O_{55.5}V_{0.5}$ shows logarithm concentration of defects as a function of log pO_2.

2.2.2. Ba doping $La_{27}W_5O_{55.5}v_{0.5}$

In this thesis, lower valence Ba was chosen to dope on La site in $La_{27}W_5O_{55.5}$, forming $Ba_{La}^{/}$ and acting as an acceptor. Disordered material $La_{27}W_5O_{55.5}$ was chosen as a host compound, which means x=1. Negatively charged acceptor must be charge compensated by forming an equal amount of positively charged defects, such as electron holes, oxygen vacancies or protons. With oxygen vacancies as charge-compensating defect, the defects equation for dissolution can be written

$$27\,\mathrm{BaO} + 5WO_3 = 4\,W_W{}^{x} + 27Ba_{La}{}^{/} + W_{La}{}^{\bullet\bullet\bullet} + 14v_{\frac{54}{56}O}^{\frac{108}{56}\bullet} + 42O_{\frac{54}{56}O}^{\frac{4}{56}/} \qquad (2.10)$$

From Eq.(2.10), two negative species, $Ba_{La}{}^{/}$ and $O_{\frac{54}{56}O}^{\frac{4}{56}/}$ are both compensated by two positive species, $v_{\frac{54}{56}O}^{\frac{108}{56}\bullet}$ and $W_{La}{}^{\bullet\bullet\bullet}$. Then the electroneutrality in acceptor doped material can be summarized as:

$$\left[Ba_{La}{}^{/}\right] + \frac{4}{56}\left[O_{\frac{54}{56}O}^{\frac{4}{56}/}\right] = \frac{108}{56}\left[v_{\frac{54}{56}O}^{\frac{108}{56}\bullet}\right] + 3\left[W_{La}{}^{\bullet\bullet\bullet}\right] \qquad (2.11)$$

Inherent defects initially charge compensate each other, therefore, positively charged oxygen vacancy is compensated by negatively charged oxygen ions. Extrinsic negatively charged defects, the acceptors, will create positively charged oxygen vacancies by transforming negatively charge oxygen ion sites. Since a certain amount of dopant is introduced, dopant could be considered "frozen in", and the concentration of it is constant. Thus, the Brouwer diagram for the Ba-doped $La_{27}W_5O_{55.5}$ is similar to undoped $La_{27}W_5O_{55.5}$.

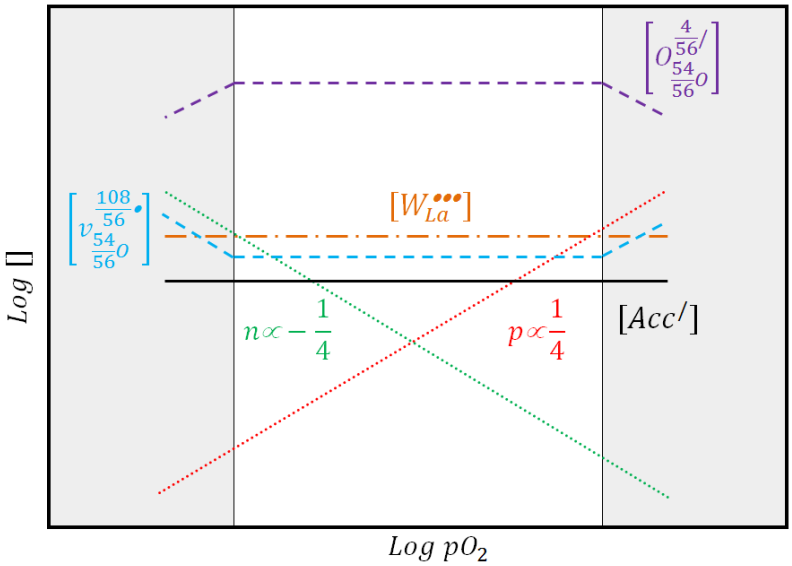

Fig.2.2 Brouwer Diagram of $La_{27}W_5O_{55.5}V_{0.5}$ with Ba dopant shows logarithm concentration of defects as a function of log pO_2.

2.2.3. Proton in $La_{27}W_5O_{55.5}v_{0.5}$

Material exposed to hydrogen atmosphere may form hydrogen containing defects. In oxides, dissolved hydrogen species are commonly associated with oxygen as proton. Proton are formed when oxygen vacancies react with water vapor

$$H_2O(g) + v_O^{\bullet\bullet} + O_O^{\,x} = 2OH_O^{\bullet} \tag{2.12}$$

Disordered fluorite related material $La_{27}W_5O_{55.5}$ may also react with water vapor because of the large amount of oxygen vacancies in intrinsic part. Vacant oxygen sites hydrated in water vapor can be written as follow:

$$H_2O(g) + v_{\frac{54}{56}O}^{\frac{108}{56}\bullet} + O_{\frac{54}{56}O}^{\frac{4}{56}/} = 2OH_{\frac{54}{56}O}^{\frac{52}{56}\bullet} \tag{2.13}$$

The equilibrium constant of hydration reaction is

$$K_{hydr} = \frac{\left[OH_{\frac{54}{56}O}^{\frac{52}{56}\bullet}\right]^2}{\left[O_{\frac{54}{56}O}^{\frac{4}{56}/}\right]\left[v_{\frac{54}{56}O}^{\frac{108}{56}\bullet}\right]p_{H_2O}} \tag{2.14}$$

The total electroneutrality is given

$$\frac{52}{56}\left[OH_{\frac{54}{56}O}^{\frac{52}{56}\bullet}\right] + \frac{108}{56}\left[v_{\frac{54}{56}O}^{\frac{108}{56}\bullet}\right] = \frac{4}{56}\left[O_{\frac{54}{56}O}^{\frac{4}{56}/}\right] \tag{2.15}$$

We assume the hydroxide defects are minority at first, which means $\left[OH_{\frac{54}{56}O}^{\frac{52}{56}\bullet}\right] << \left[v_{\frac{54}{56}O}^{\frac{108}{56}\bullet}\right]$, then we obtain native defects $v_{\frac{54}{56}O}^{\frac{108}{56}\bullet}$ and $O_{\frac{54}{56}O}^{\frac{4}{56}/}$ dominating and constant

$$\frac{108}{56}\left[v_{\frac{54}{56}O}^{\frac{108}{56}\bullet}\right] \cong \frac{4}{56}\left[O_{\frac{54}{56}O}^{\frac{4}{56}/}\right] \tag{2.16}$$

By inserting this, the concentration of protons reads

$$\left[OH_{\frac{54}{56}O}^{\frac{52}{56}\bullet}\right] = \left(108\ K_{hydr}\right)^{\frac{1}{2}} p_{H_2O}{}^{\frac{1}{2}} \tag{2.17}$$

With the material taking up more water, hydroxide defects increase and can become major defects, which means $\left[OH_{\frac{54}{56}O}^{\frac{52}{56}\bullet}\right] >> \left[v_{\frac{54}{56}O}^{\frac{108}{56}\bullet}\right]$, then we get $OH_{\frac{54}{56}O}^{\frac{52}{56}\bullet}$ and $O_{\frac{54}{56}O}^{\frac{4}{56}/}$ dominating and constant

$$\frac{52}{56}\left[OH_{\frac{54}{56}O}^{\frac{52}{56}\bullet}\right] \cong \frac{4}{56}\left[O_{\frac{54}{56}O}^{\frac{4}{56}/}\right] \tag{2.18}$$

Then the relation between oxygen vacancies and water vapor partial pressure is

$$\left[v_{\frac{54}{56}O}^{\frac{108}{56}\bullet}\right] = \frac{4}{13}\left(K_{hydr}\right)^{-1}\left(p_{H_2O}\right)^{-1} \tag{2.19}$$

The Brouwer diagram based on the calculation above is given as

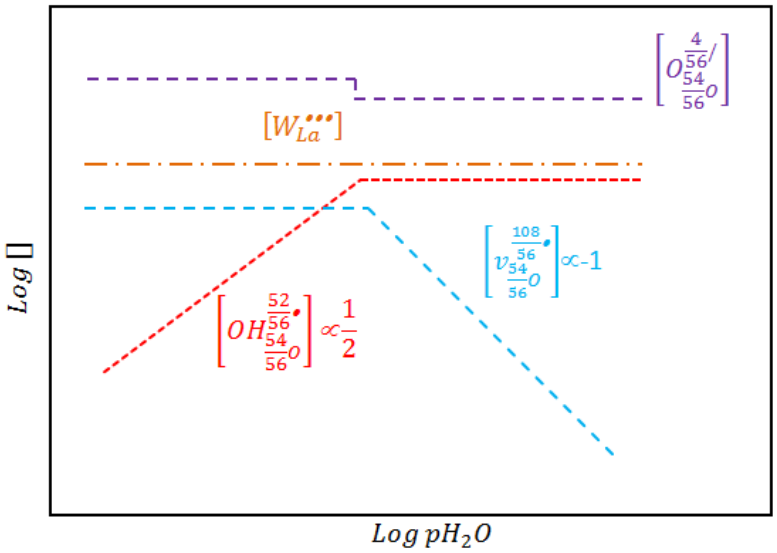

Fig.2.3 Brouwer Diagram of $La_{27}W_5O_{55.5}V_{0.5}$ shows logarithm concentration of defects as a function of log pH_2O.

2.2.4. Proton in Ba-doped $La_{27}W_5O_{55.5}v_{0.5}$

The electroneutrality of $La_{27}W_5O_{55.5}$ with Ba dopant under wet condition can be expressed as

$$\frac{52}{56}\left[OH_{\frac{54}{56}O}^{\frac{52}{56}\bullet}\right]+\frac{108}{56}\left[v_{\frac{54}{56}O}^{\frac{108}{56}\bullet}\right]=\frac{4}{56}\left[O_{\frac{54}{56}O}^{\frac{4}{56}/}\right]+\left[Ba_{La}{}'\right] \quad (2.20)$$

The only difference from Eq. (2.15) to the undoped one is that acceptor involved in as a charge compensating defect. Same reason previously described, the Brouwer diagram of pH_2O for the Ba-doped $La_{27}W_5O_{55.5}V_{0.5}$ is similar with the undoped one shown in Fig.2.3.

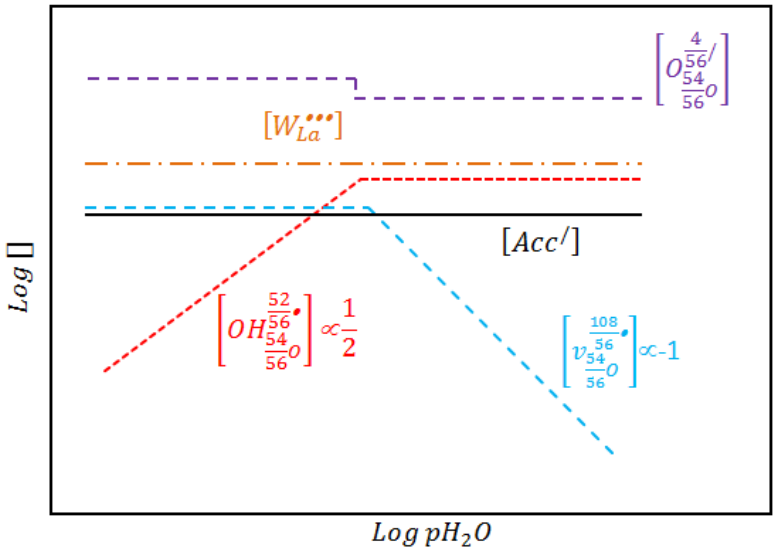

Fig.2.4 Brouwer Diagram of Ba-doped $La_{27}W_5O_{55.5}V_{0.5}$ shows logarithm concentration of defects as a function of log pH_2O.

2.2.5. Hydration thermodynamics in oxides

When water is present, oxygen vacancies may be hydrated to form protonic defects through the hydration reaction Eq.(2.13). The equilibrium constant K_{hydr} from Eq.(2.14) can also be described by thermodynamic constants, standard Gibbs energy, enthalpy and entropy changes, ΔG_{hydr}^0, ΔH_{hydr}^0 and ΔS_{hydr}^0

$$K_{hydr}=exp\left(-\frac{\Delta G_{hydr}^0}{RT}\right)=exp\left(\frac{\Delta S_{hydr}^0}{R}\right)exp\left(-\frac{\Delta H_{hydr}^0}{RT}\right) \quad (2.21)$$

Hydration reaction and the equilibrium are very important for modeling the proton conduction behavior in oxides. Assuming that all the negatively charged defects in Eq.(2.20) are combined and denoted as $[Acc']$, for simplicity, we may write

$$\frac{52}{56}\left[OH_{\frac{54}{56}O}^{\frac{52}{56}\bullet}\right]+\frac{108}{56}\left[v_{\frac{54}{56}O}^{\frac{108}{56}\bullet}\right]=\left[Acc'\right] \tag{2.22}$$

Combining Eq.(2.14), and (2.22), the concentration of protons in this work can be calculated through a quadratic equation

$$\left[OH_{\frac{54}{56}O}^{\frac{52}{56}\bullet}\right]=\frac{13}{56}K_{hydr}\left[O_{\frac{54}{56}O}^{\frac{4}{56}/}\right]P_{H_2O}\left(-1+\sqrt{1+\frac{1512[Acc']}{169K_{hydr}\left[O_{\frac{54}{56}O}^{\frac{4}{56}/}\right]P_{H_2O}}}\right) \tag{2.23}$$

2.3. Electrical conductivity

Charged particles move in solid by electric potential gradient as a driving force, which is given by both the electric field and the charge of the species. The following expression gives the driving force exerted on a charged particle of type i

$$F=-z_i e\frac{d\phi}{dx}=-z_i eE \tag{2.24}$$

where $E=-\frac{d\phi}{dx}$ is the electric field and $z_i e$ is the charge of the particle of type i.

The driving force here gives rise to the current density i_i, which is the product of flux density and charge, and can be eventually written:

$$i_i=z_i e\mu_i c_i E=\sigma_i E \tag{2.25}$$

where σ_i, c_i, and μ_i are the partial conductivity, concentration and mobility of species i, respectively. Therefore, the definition of partial conductivity is got:

$$\sigma_i=z_i e\mu_i c_i \tag{2.26}$$

In this work, the activated process of charge carriers is assumed to rely on activated jumping. By inserting the expression for mobility, a new expression for conductivity is given

$$\sigma_i = \sigma_i = \frac{\sigma_0}{T}\exp\left(-\frac{\Delta H_{m,i}}{RT}\right) = z_i e c_i \mu_{0,i}\frac{1}{T}\exp\left(-\frac{\Delta H_{m,i}}{RT}\right) \quad (2.27)$$

where σ_0 is the pre-exponential of conductivity, and $\Delta H_{m,i}$ is the enthalpy of mobility of charge carrier.

The total conductivity should be the sum of the partial conductivities of all the contributing charge carries.

$$\sigma_{tot} = \Sigma\sigma_i \quad (2.28)$$

The transport number of charge carries t_i, can be given as the ratio of partial conductivity σ_i to the total conductivity σ_{tot}

$$t_i = \frac{\sigma_i}{\sigma_{tot}} \quad (2.39)$$

2.4. Isotope effect

The use of H_2O-D_2O isotope exchange in conductivity measurements is a common means of verifying the proton effect when oxides exhibit proton conductivity. The unique ratio between the masses of protium (H) and deuterium (D) isotopes of hydrogen is 1:2, which give rise to the isotope effect of proton diffusion. According to Nernst-Einstein relationship for hopping species, ionic conductivity directly related to diffusion can be derived

$$\sigma_i = \text{zieμici} = \frac{(z_i e)^2 c_i D_i}{KT} \quad (2.30)$$

where D_i is the self-diffusion coefficient of specie i and K is Boltzmann constant. The self-diffusion is proportional to the attempt frequency ν, which is given by the inverse of the square root of the reduced mass of the harmonic oscillator. The reduced mass here is proportional to the mass of hydrogen. Therefore, the ratios of the diffusion coefficients of protons and deuterons are roughly inversely proportional to the square root of the mass of H and D and can read:

$$D_{OH_O^\bullet} = \sqrt{2} D_{OD_O^\bullet} \tag{2.31}$$

From Eq. (2.31) and (2.32), the theoretical ratio between $\sigma_{OH_O^\bullet}$ and $\sigma_{OD_O^\bullet}$ is $\frac{1}{\sqrt{2}}$. This explains why in oxides with proton conductivity, the conductivity in deuterium containing atmosphere is observed lower than the one in hydrogen containing atmosphere.

2.5. Electrochemical impedance spectroscopy (EIS)

Electrochemical impedance spectroscopy is a very powerful method for characterizing electrical properties of materials and their interfaces, by measuring complex impedance over a wide range of frequencies, typically from 5 HZ to 10 MHZ. We may specify the grain interior contribution and grain boundary contribution due to the resistive and capacitive elements arising from them.

When voltage is applied to an ionic or mixed conductor, positive charged ions move to the negative electrode and negative charged ions move to the positive electrode. This movement of ions leads to the polarization of electrode, which causes the current to drop with time.

2.5.1. Alternating current and impedance

Impedance is a more general expression for what we called resistance. The difference is that resistance mainly is used to describe for DC condition, while impedance covers both AC and DC. In AC impedance measurements, follow Ohm law, we get impedance as follow

$$Z = \frac{U}{I} = \frac{U_0 \sin \omega t}{I_0 \sin(\omega t + \theta)} \tag{2.32}$$

The current compromise two parts, one is in phase with the voltage, the other is π/2 out of the phase. Therefore, the impedance is respectively divided into two parts. The

real part of the impedance is the in phase part, which is denoted resistance R and the imaginary part of it is the π/2 out of phase component, which is called reactance X. The real part reflect the resistance of charge carriers through the impedance element, while the imaginary part reflect the one storing there temporarily, not transporting though it.

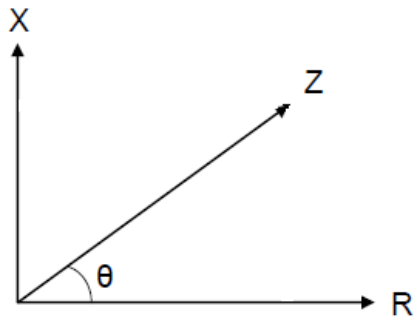

Fig.2.5 Complex impedance, x axis is the real part; y axis is the imaginary part.

In Fig.2.5, the impedance Z is taken as a vector in the two dimensional real imaginary space, with shift angle θ. The impedance can be expressed as

$$Z^* = Z^{/} + jZ^{//} = R + jX \left(j = \sqrt{-1}\right) \tag{2.33}$$

The inverse of impedance is admittance: $Y^* = 1/Z^*$, which means the ratio between the current and the voltage. The real part of admittance is denoted conductance, G, and the imaginary part is denoted susceptance, B. The total admittance is therefore given as

$$Y^* = Y^{/} + jY^{//} = G + jB \left(j = \sqrt{-1}\right) \tag{2.34}$$

2.5.2. Passive electrical circuit elements

In polycrystalline materials, grains are separated by a large number of grain boundaries. Sample and electrodes are separated by interphase. When the sample is charged, grain interiors, grain boundaries, electrodes and interphases impede the

transportation of charge carries. Therefore, the equivalent circuit can be regarded as the combination of the resistance, R, the capacitance, C, and the inductance, L.

Resistors (conductors)

A resistor or a conductor is an element to transfer charge carriers. The number of charge carries, concentration and the mobility of charge carries give a positive effect on conductor G, meanwhile resistance R = 1/G. When a sine voltage is applied, the resistance is given as

$$R = \frac{U}{I} = \frac{U_0 \sin \omega t}{I_0 \sin(\omega t + \theta)} \tag{2.35}$$

ω here is angular frequency.

Capacitors

A capacitor, which is an ideal insulator, can typically be considered as two parallel plate conductors separated by vacuum. When the capacitor is charged, in general the capacitance of it reads

$$C = \varepsilon_0 \varepsilon_\gamma \frac{A}{d} \tag{2.36}$$

where ε_0 is the permittivity of vacuum, $\varepsilon_0 \approx 8.854 * 10^{-14}$ F/cm, ε_r is the relatively static permittivity of the insulating medium between the plates, A is the area and d is the distance between the plates. If AC voltage is applied, we get

$$I = C \frac{d(U_0 \sin \omega t)}{dx} = \omega C U_0 \cos \omega t = \omega C U_0 \sin\left(\omega t + \frac{\pi}{2}\right) \tag{2.37}$$

The current through the capacitor is π/2 head of the AC voltage. The resistance of capacitor is given as the ratio between the peak voltage and the peak current when AC voltage is applied,

$$R_C = \frac{1}{\omega C} \tag{2.38}$$

Inductors

Inductor is an ideal conductor with no resistance. When AC voltage is applied on the inductor, the voltage shows:

$$U = -U_L = L\frac{dI}{dt} = L\frac{d(I_0 \sin \omega t)}{dt} = \omega L I_0 \cos \omega t = \omega L I_0 \sin\left(\omega t + \frac{\pi}{2}\right) \qquad (2.39)$$

where L is the inductance of the inductor.

Thus, the voltage applied is π/2 ahead of the current. The inductor resistance is:

$$R_L = \omega L \qquad (2.40)$$

2.5.3. Impedance sweep

In impedance measurement, we plot sweep with resistance, R versus negative reactance, -X, which is so called Nyquist plots. For polycrystalline materials, the Nyquist plot shows several semicircles which can be interpreted by the combination of passive electrical circuit elements previously mentioned. Fig.2.6 shows the typical impedance sweep of a polycrystalline material, with three semicircles denoted the contribution of grain interior, grain boundary, electrode from high frequency to low frequency. One may note, in some situation a semicircle denoted the interface between grain boundary and electrode or denoted another grain boundary could be observed as well. Assume a sample could be ideally described as a model equivalent circuit with two electrical circuit elements, a resistor and a capacitor in parallel, (RC). Then, using three (RC) in series could describe the impedance spectra in Fig.2.6. From Eq. (2.36) and Eq. (2.39), the peak frequency of one (RC) circuit element corresponds to a perfect semicircle can read:

$$\omega = \frac{1}{RC} = \frac{A}{L\rho}\frac{L}{\varepsilon_0 \varepsilon_r A} = \frac{\sigma}{\varepsilon_0 \varepsilon_r} \qquad (2.41)$$

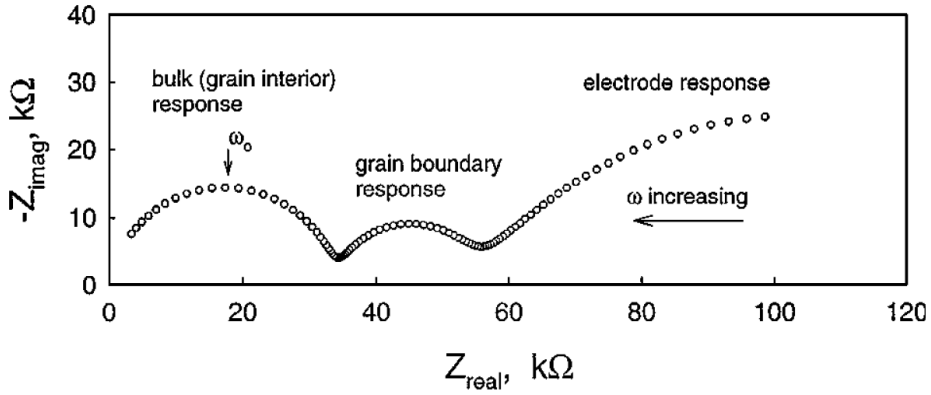

Fig.2.6 Typical impedance spectra from a polycrystalline sample[14].

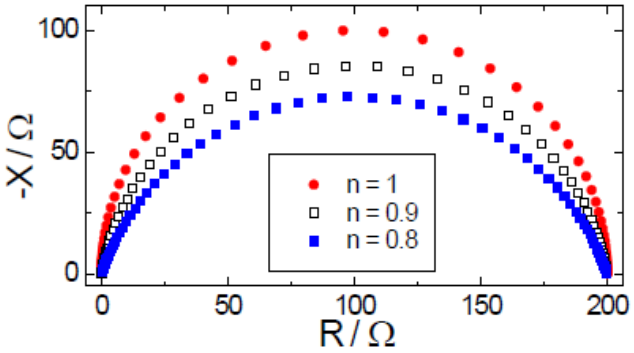

Fig.2.7 The calculated complex impedance of a parallel circuit of a resistor and a constant phase element (CPE), when n=1, the CPE represents an ideal capacitor[15]

However, the equivalent circuit of a real crystalline material is much more complicated, for instance grain and grain boundary are in different size and orientation to the current. The practical passive elements in the impedance are different from the ideal passive elements. Actually, the impedance for real materiasl shows a depressed semicircle. This phenomenon is attributed to a distribution of the time constants of the individual grains. Fig.2.7 above shows the depressed semicircle. In order to model these depressed semicircles, a constant phase element, CPE or Q is introduced to describe non-ideal capacitors. The admittance and impedance of a CPE is given as

$$Y_{CPE} = Y^0(j\omega)^n = Y_0\omega^n \cos\left(\frac{n\pi}{2}\right) + jY_0\omega^n \sin\left(\frac{n\pi}{2}\right) \qquad (2.42)$$

where n is a constant, which can vary between +1 and -1. In special case, when n = +1, 0, and -1, CPE represents ideal capacitance, conductance, and inductance.

Further, the capacitance of each (RQ) equivalent circuit is given as

$$C = Y^{\frac{1}{n}} R^{\frac{1-n}{n}} \tag{2.43}$$

Nyquist plot of a polycrystalline material typically consists of three semicircles, from high frequency to low frequency, corresponding to bulk, grain boundary and electrode, respectively. The n value of the CPE corresponding to gain boundary is lower than the one to bulk. Actually, this three semicircles condition is an ideal condition. The grain resistance and the grain boundary resistance of most polycrystalline material change with temperature. Therefore, at some temperatures, for some materials, the Nyquist plot shows just part of the three semicircles. The value of different capacitances corresponds to different individual contribution is shown in Table 2.2

Table 2.2 Capacitance values and their conventional interpretation.

Phenomenon responsible	**Capacitance (F)**
Bulk	10^{-12}
Secondary phase	10^{-11}
Grain boundary	$10^{-11} - 10^{-8}$
Bulk, ferroelectric	$10^{-10} - 10^{-9}$
Surface layer	$10^{-9} - 10^{-7}$
Sample electrode interphase	$10^{-7} - 10^{-5}$
Electrochemical reactions	10^{-4}

2.5.4. Brick layer model

Brick layer model was proposed to describe the microstructure in polycrystalline materials. From Fig.2.8, Brick layer model assumes that uniform cube-shaped grains are separated by grain boundaries both in parallel and perpendicular to the direction along the field, which means in series as well. The relevant geometric parameters in Fig.2.8 (a) are defined as L = sample length, A = sample cross section area, g = grain boundary thickness, and G = edge length of grain. Assuming each component of the

material behaves as a (RQ) subcircuit, from Fig.2.8 (b), there are three subcircuits in series. The first one consists of grains and parallel grain boundaries, the second one consist of only grain boundaries and the last one denoted electrode effect

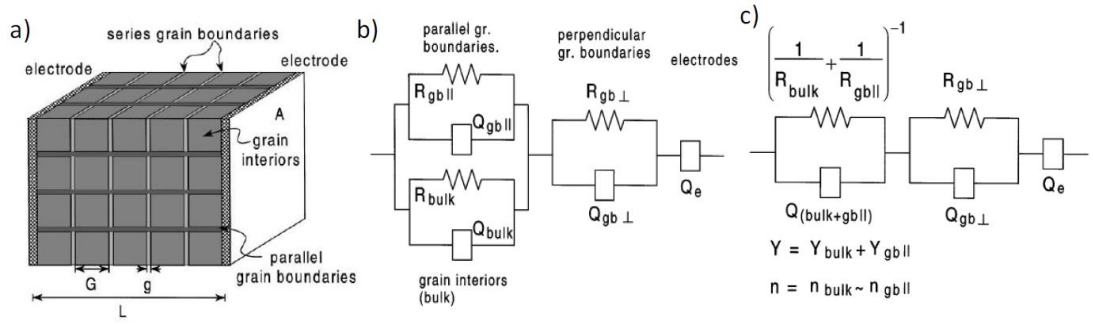

Fig.2.8 (a) Brick layer model, (b) equivalent circuit, (c) simplified equivalent circuit[16].

Since the width grain boundary is considered much smaller than the one of grain, the total length of the grain boundaries in parallel with bulks is assumed to equal to L and the total cross section area is assumed to equal to $\frac{2g}{G}A$. Similarly, the total length and area of the grain boundaries in series is with $\frac{g}{G}L$ and A, respectively. By defining $\sigma_i = L/AR_i$, the conductivity from the sum of the bulk and grain boundary in parallel,σ_1, and the one from the grain boundary in series,σ_2, can be found as:

$$\sigma_1 = \left(\frac{2g}{G}\sigma_{gb} + \sigma_{buk}\right) \tag{2.44}$$

$$\sigma_2 = \left(\frac{G}{g}\sigma_{gb}\right) \tag{2.45}$$

Combining Eq.(2.44) and (2.45), the ratio R_2 to R_1 can be obtained from the ratio of σ_1 and σ_2

$$\frac{\sigma_1}{\sigma_2} = \frac{R_2}{R_1} = 2\left(\frac{g}{G}\right)^2 + \left(\frac{g}{G}\right)\frac{\sigma_{bulk}}{\sigma_{gb}} \tag{2.46}$$

However, for the polycrystalline material, the width of grain is estimated 100 times bigger than the width of grain boundary, hence, Eq. (2.44) can be simplified to

$$\sigma_1 = (\sigma_{buk}) \tag{2.47}$$

And Eq.(2.46) reduces to

$$\sigma_{gb} = \left(\frac{g}{G}\sigma_2\right) \tag{2.48}$$

From Eq. (2.47) and Eq. (2.48), some microstructural parameters still need to be studied to find the specific conductivity of grain boundary. Since the parallel grain boundary has an unfavorable geometry, the contribution of it to the capacitance could be negligible. C_1 could be considered as the capacitance only attributed by bulk while C_2 is attributed by perpendicular grain boundaries. Consider the dielectric constants of the bulk and ground boundary is similar, the ratio g/G could be obtained by capacitance of the subcircuits.

$$\frac{g}{G} = \frac{C_1}{C_2} \tag{2.49}$$

$$\sigma_{gb} = \left(\frac{C_1}{C_2}\sigma_2\right) \tag{2.50}$$

2.6. Space charge layer theory

Grain boundary is a crystallographic mismatch zone, which can be observed by transmission electron microscopy (TEM). High electrical resistance in grain boundaries is observed for several types of conductors such as oxide ion conductor, mixed electron-oxide ion conductor and proton conductor. It is commonly attributed to segregation of impurities or secondary phases. Studies show that even in high purity materials, highly resistive intrinsic grain boundaries exist. Intrinsic grain boundary resistances properties for oxide ion conductor such as acceptor-doped ZrO_2 and CeO_2 have successfully been interpreted by a grain boundary core-space charge layer model [17, 18]. Later, the intrinsic grain boundary properties for proton conducting materials such as Y-doped $BaZrO_3$ was also studied[19].

Fig.2.9 depicts that in electrical term, a grain boundary consists of a core with two adjacent space-charge layer. In principle, the core can be positively charged or negatively charged. Here, we assume that the core is positively charged, for instance, $v_O^{\bullet\bullet}$ resident in the core. In order to maintain electroneutrality, the positively charged core should be balanced. Due to the depletion of positively charged defects, negatively charged defects accumulate in the space-charge larger, which can compensate the positively charged core. This gives rise to the electrical potential in the space-charge layer, the Schottky barrier height, Δφ(0), which increases with the number of positively charged defects being transferred to the core. Thus, a higher Δφ(0) means a more depletion of positively charged defects such as $OH_O^{\bullet}$, etc, while the negatively charged defects such as $e^{/}$ will increase.

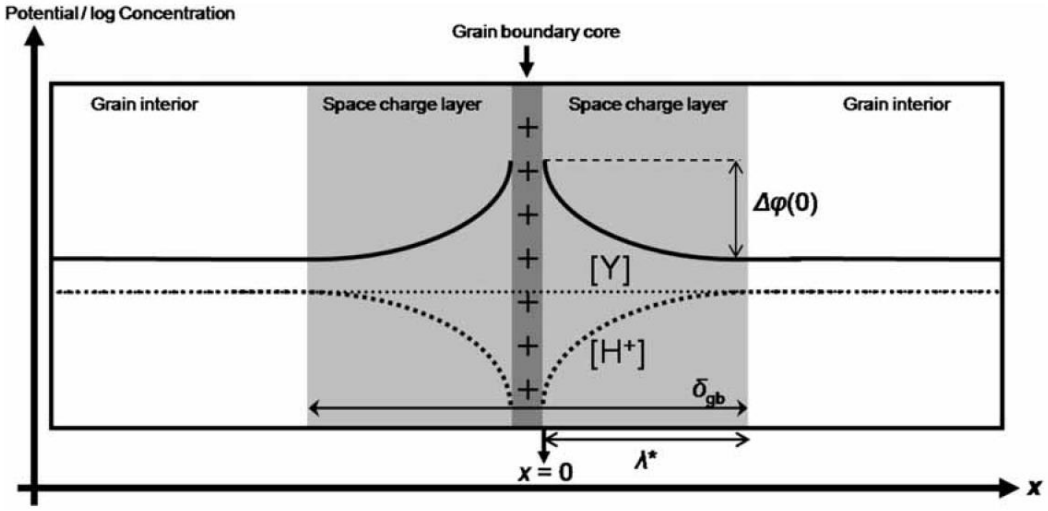

Fig.2.9 Schematic grain boundary consisting of a positive core charge compensated by two space-charge layers. The dotted lines represent concentration profiles in the space-charge layer for protons and the acceptor dopant under the Mott-Schotty approximation, [19].

3. Literature

Proton conductors have received many attentions as candidates for electrolytes of sensors, batteries, fuel cells, electrolysers, etc. Several perovskite-structured oxides exhibit proton and mixed proton-electron conductivity at high temperatures, however, these oxides are vulnerable to CO_2. In order to find new high temperature proton and mixed proton-electron conductors with CO_2 stability, the electrical properties of rare earth tungstates were studied. Yoshimura and Baumard [20]. first reported the electronic and ionic conduction of La_6WO_{12} with CeO_2 doping. However, they did not go further to the proton effects. Later, Shimura et al.[9]. first reported the existence of proton conductivity in La_6WO_{12}. Afterwards, Magraso et al.[13, 21] pointed out that lanthanum tungstates with La/W=5.7-5.3 show promise for use in industrial processes. Furthermore, crystal structure and defect model of $La_{28-x}W_{4+x}O_{54+\frac{3}{2}x}v_{2-\frac{3}{2}x}$ were studied.

3.1. Proton conductors

Pure and high proton conductivity in solid oxide materials was first reported by Iwahara et al. for $SrCeO_3$[22, 23] and $BaCeO_3$[24], which are of perovskite type structure. In addition to perovskites, rare-earth fluorite related structures and pyrochlore structure have also been studied. Fig.3.1 shows proton conductivity of various oxides calculated from the data on proton concentrations and mobility by Norby et al.[25]. $BaCeO_3$ based material demonstrates the highest proton conductivity. Kreuer[26] pointed that $BaCeO_3$ is the perovskite with higher lattice constants and smaller distortion from ideal cubic perovskite structure than $SrCeO_3$ leads to a higher proton conductivity.

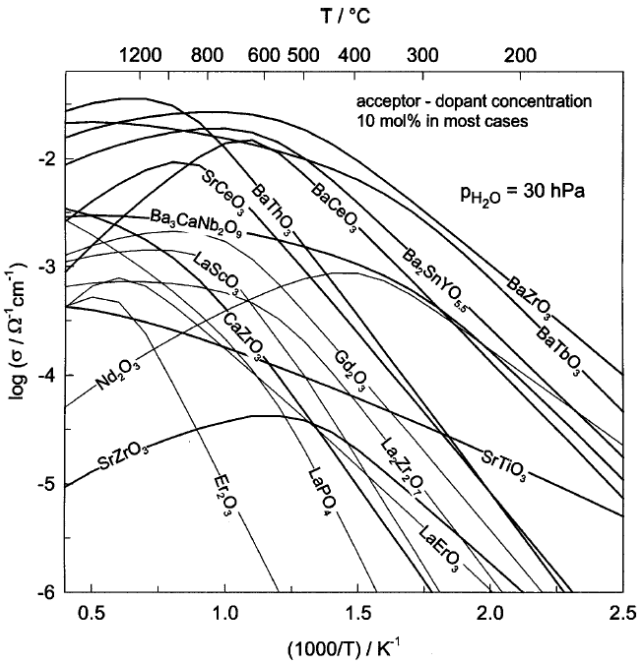

Fig.3.1 Proton conductivities of various oxides[26] as calculated from data on proton concentrations and mobilities[25].

In the light of recent findings, highly Y-doped $BaZrO_3$ with high bulk proton conductivity with high stability is particularly promising. Fig.3.2 displays that proton conductivity of 20% Y-doped BaZrO3 is higher than 10% Y-doped. According to Kreuer, BaZrO3 is the cubic perovskite with the highest lattice constant and the high symmetry of leads to the high solubility limit of protonic defects. He also analyzed from the side of acceptor dopant choice. For the other acceptor dopants reported that the proton conductivity decrease with increasing acceptor doping level.

However, the conductivity of Y-doped $BaZrO_3$ is significantly lower than the corresponding bulk conductivity, due to blocking effects caused by grain boundaries shown in Fig.3.3. Since the mobility and concentration of proton is very sensitive to the symmetry[26], structural distortion in grain boundary is likely to slow down the mobility of proton and possibly to deplete the proton.

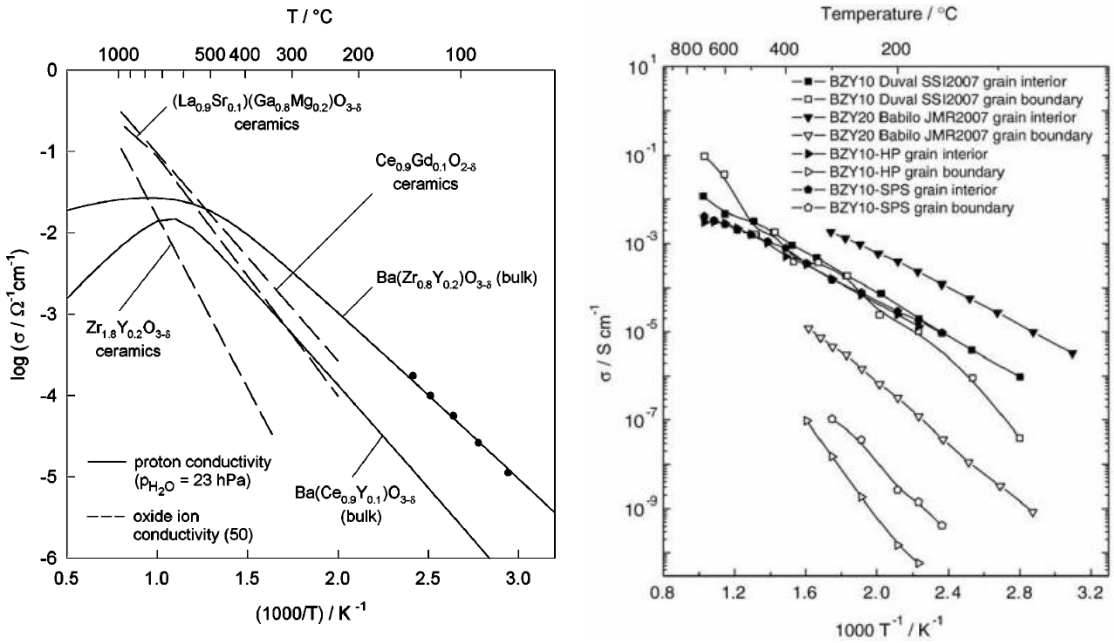

Fig.3.2(left) Bulk conductivity of 20% Y doped $BaZrO_3$ compared with 10% Y doped $BaCeO_3$[26] and oxide oxide ion conductivity of the best oxide ion conductors.

Fig.3.3(right) The specific grain interior and and grain boundaries for $BaZrO_3$ as a function of inverse absolute temperature[19, 27, 28].

3.2. Defects in Ln_6WO_{12} (Ln= La, Nd, Gd, Er)

3.2.1. Crystal structure of Ln_6WO_{12} (Ln= La, Nd, Gd, Er)

The structure of the rare-earth tungstates can be described either as an ordered defective fluorite or a disordered pyrochlore[29-31]. The ordered structure for example Re_6WO_{12} is described in Fig.3.4. Seven cubes share edges, including one WO_8 cube and six LnO_8 cubes. One W^{6+} cation locates in the middle of the central cube, with two oxygen vacancies being located on one of the main diagonal. The other six cubes surround the central one, containing rare-earth cations, Ln^{3+}, in the middle and only one oxygen vacancy. Furthermore, the symmetry of this oxide changes with rare-earth element: cubic or pseudo-cubic from La to Pr, pseudo-tetragonal from Nd to Gd, and rhombohedral from Tb to Lu and for Y[32].

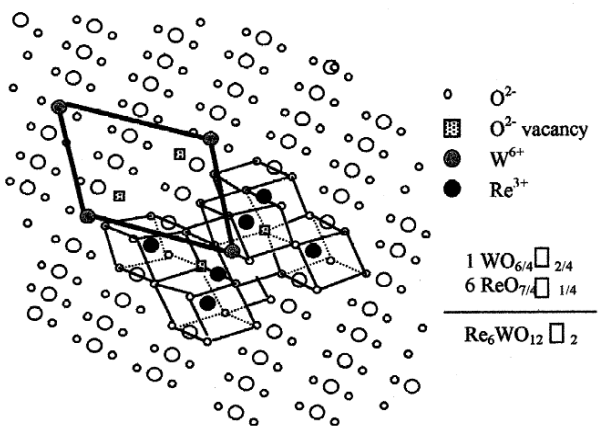

Fig. 3.4 Structural model for the tungstates $Re_6WO_{12}$with a rhombohedral symmetry[31].

3.2.2. Electrical properties of Ln6WO12 (Ln= La, Nd, Gd, Er)

The point defects and transport properties of undoped and Ca-doped Ln_6WO_{12} (Ln= La, Nd, Gd, Er) were studied by Haugsrud[6].The maximum proton conductivity was observed with the value in order of 3-5 mS/cm for undoped La_6WO_{12}. Fig.3.5 shows an isotope effect below approximately 800 °C, which indicates that protons predominate the conductivity under wet condition at relatively low temperature. And it clearly shows that there is effect of doping varying with different rare-earth cation.

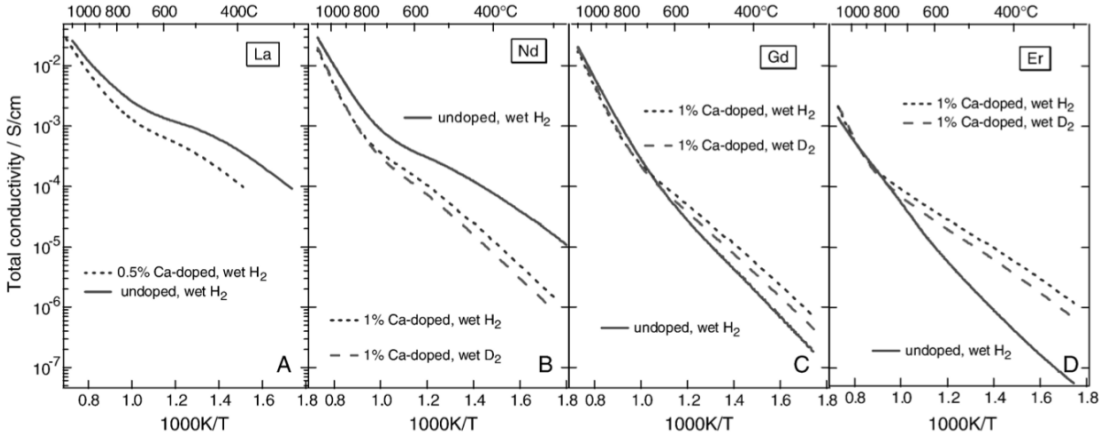

Fig.3.5 The total ac conductivity (10 kHz) as a function of the 1/T for undoped and Ca-doped, $LnW_{1/6}O_2$, [Ln= La(A), Nd(B), Gd(C), Er(D)] under H2+2.5% H2O and D2+2.5% D2O atmospheres in the temperature range 300 °C to 1100 °C[6].

One can conclude from Fig.3.5, that the conductivity decreases for Ca-doped $LaW_{1/6}O_2$ and $NdW_{1/6}O_2$. However, the conductivity increases for Ca doping for $GdW_{1/6}O_2$ and $ErW_{1/6}O_2$ up to 800 °C. the steeper slope of the conductivity of $GdW_{1/6}O_2$ and $ErW_{1/6}O_2$ above ~900 °C means a stronger dependence on temperature than for $LaW_{1/6}O_2$ and $NdW_{1/6}O_2$. As shown by the partial conductivity in wet H_2 from electromotive forces technique (EMF) in Fig.3.6, that electrons directly take up protons as predominating charge carriers explains this strong dependence on temperature. However, for Ca-doped $LaW_{1/6}O_2$ and $NdW_{1/6}O_2$, both oxygen ion and electron conductivity contribute.

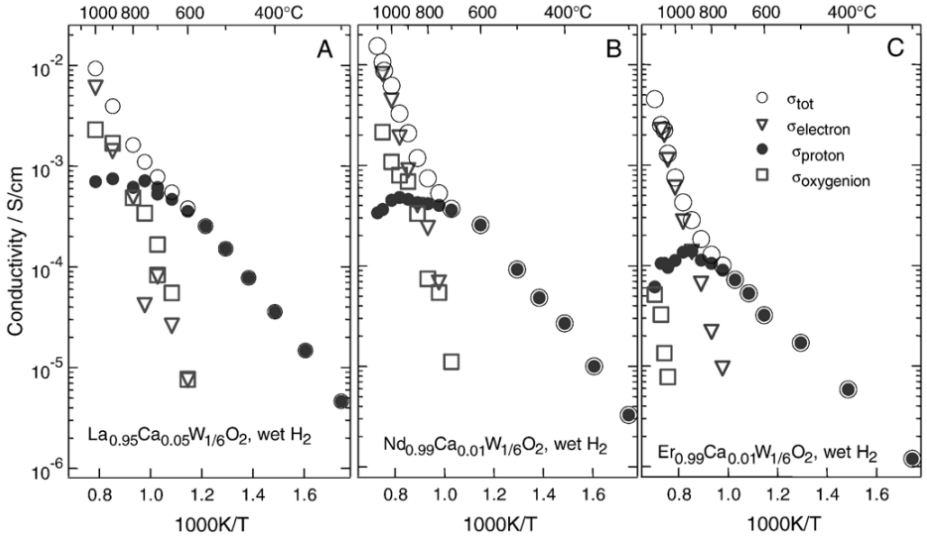

Fig.3.6 Partial conductivities, as determined from the EMP-technique, as function of the 1/T for Ca-doped $LaW_{1/6}O_2$, $NdW_{1/6}O_2$ and $ErW_{1/6}O_2$ under H_2+2.5% H_2O atmospheres in the temperature range 300 °C to 1050 °C[6].

In addition, Haugsrud measured the pO_2 dependence of the total AC conductivity for the four different rare-earth tungstates with Ca doping at 800 °C in wet gas presented in Fig.3.7. It shows that the conductivity of Ca-doped Gd $W_{1/6}O_2$ and $ErW_{1/6}O_2$ is predominated by electrons under reducing conditions while it is predominated by electron holes under oxidizing conditions. From the partial pressure dependence, doped $LaW_{1/6}O_2$ has relatively low electronic contribution compared to the other three materials. One can also note that there is a sudden increase of one order of magnitude of the total conductivity for $Nd_{0.99}Ca_{0.01}W_{1/6}O_2$, which might indicate phase transition

happening between two different conditions.

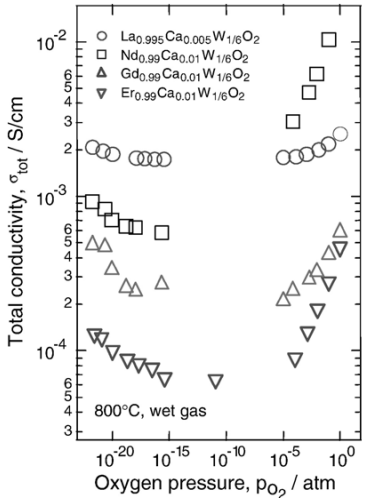

Fig.3.7 Total ac conductivity (10 kHz) as a function of the oxygen partial pressure for Ca-doped $LnW_{1/6}O_2$ (Ln= La, Nd, Gd, Er) at 800 °C under wet condition[6].

3.2.3. Hydration properties of Ln_6WO_{12} (Ln= La, Nd, Gd, Er)

By modeling the conductivity and thermogravimetric data, thermodynamic and transport parameters for the compounds across the rare-earth series were aslo extracted and reported by Haugsrud. The standard hydration enthalpy changes in Ca-doped $LaW_{1/6}O_2$, $NdW_{1/6}O_2$, $GdW_{1/6}O_2$ and $ErW_{1/6}O_2$ is ~-90 kJ/mol, ~110 kJ/mol, ~-120 kJ/mol and ~-135 kJ/mol, respectively.

3.3. Defects in La_6WO_{12}

3.3.1. Electrical properties of La_6WO_{12}

Electrical properties of La_6WO_{12} was studied in detail by Haugsrud et al.[7]. Fig.3.8 (A) presents the AC conductivity of undoped La_6WO_{12} as a function of inverse absolute temperature in different conditions. A difference between the conductivities in wet condition (with 2.5% H_2O or D_2O) and dry condition (with 30 ppm H_2O) is observed in Fig.3.8 (B).

Fig.3.9 (A) demonstrates the temperature dependence of the total conductivity for $La_{0.95}Ca_{0.05}W_{1/6}O_{\sim 2}$, $La_{0.995}Ca_{0.005}W_{1/6}O_{\sim 2}$ and $LaW_{1/6}O_2$ comparing with each other. In Fig.3.9 (B) the temperature dependence of the total conductivity for $La_{0.9}W_{1/6}O_{\sim 2}$, $La_{0.95}W_{1/6}O_{\sim 2}$ and $LaW_{1/6}O_2$ are compared. One may notice that the conductivity of acceptor doped materials is lower than the one of non-stoichiometric and undoped materials. Furthermore, the difference increases with the amount of doping and decreasing temperature.

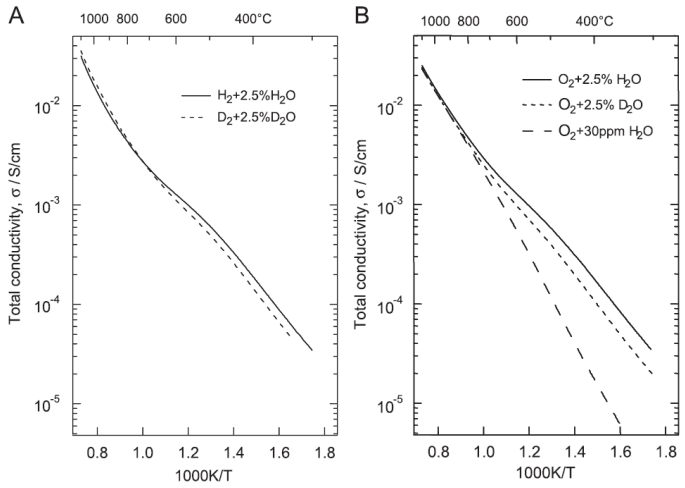

Fig.3.8 Total ac conductivity (10 kHz) as a function of the 1/T for $LaW_{1/6}O_2$ in H_2+2.5% H_2O, D_2+2.5% D_2O atm (A) and O_2+2.5% H_2O , O_2+2.5% D_2O, O_2+30ppm H_2O atm (B) in the temperature range 300 °C to 1100 °C[7].

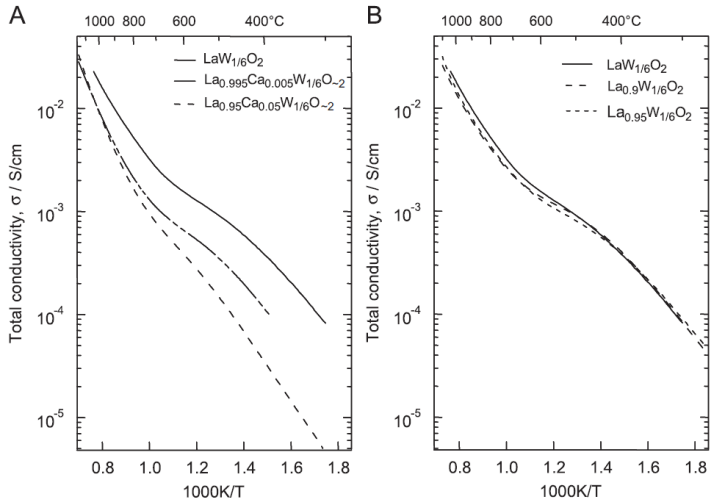

Fig.3.9 Total ac conductivity (10 kHz) as a function of the 1/T for $La_{0.95}Ca_{0.05}W_{1/6}O_{\sim 2}$, $La_{0.995}Ca_{0.005}W_{1/6}O_{\sim 2}$ and $LaW_{1/6}O_2$ (A) and $La_{0.9}W_{1/6}O_2$, $La_{0.95}W_{1/6}O_2$ and $LaW_{1/6}O_2$ (B) as measured in wet hydrogen in the temperature range 300 °C to 1100 °C [7].

The different dependences of oxygen partial pressure for the three materials shown in Fig.3.10, represent a typical mixed ionic-electronic conductor: total conductivity decreases with pO_2 under reducing condition, while it increases with pO_2 under oxidization condition, and the total conductivity is pO_2 independent at intermediate region.

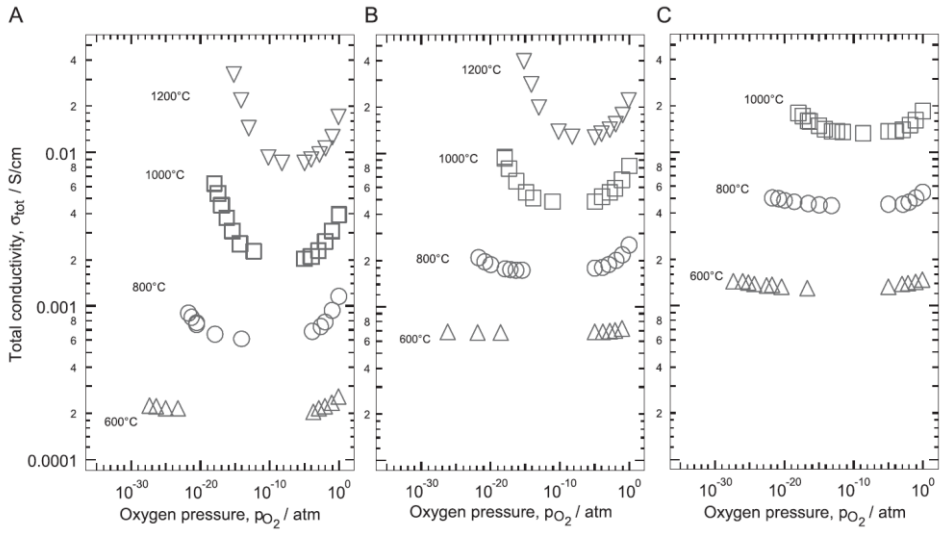

Fig.3.10 Total ac conductivity (10 kHz) as a function of the oxygen partial pressure at different temperatures from 600°C to 1200°C for $La_{0.95}Ca_{0.05}W_{1/6}O_{\sim 2}$ (A), $La_{0.995}Ca_{0.005}W_{1/6}O_{\sim 2}$ (B) and $LaW_{1/6}O_2$ (C). Measurements are performed under wet conditions [7].

Fig.3.11 shows the total conductivity as a function of water vapor partial pressure for $La_{0.9}W_{1/6}O_{\sim 2}$, $La_{0.95}W_{1/6}O_{\sim 2}$ and $LaW_{1/6}O_2$ under reducing condition. The conductivity of acceptor-doped materials is lower than the one of undoped material, moreover, the higher the doping level is, the lower the conductivity is. The conductivity increases with increasing amount of water vapor partial pressure. However, the dependency decreases with increasing temperature, and pH_2O dependency is almost invisible up to 900°C.

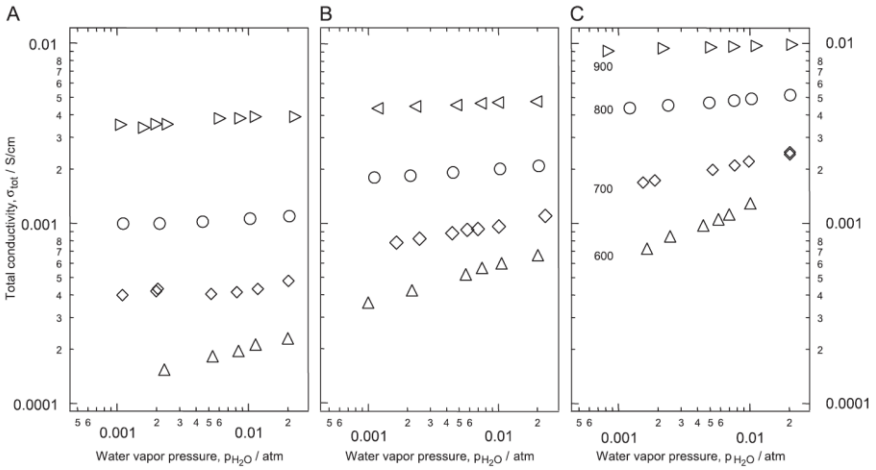

Fig.3.11 Total ac conductivity (10 kHz) as a function of the water vapor partial pressure in hydrogen at different temperatures from 600°C to 900°C for $La_{0.95}Ca_{0.05}W_{1/6}O_{\sim 2}$ (A), $La_{0.995}Ca_{0.005}W_{1/6}O_{\sim 2}$ (B) and $LaW_{1/6}O_2$ (C)[7].

The equation of Ca-doped La_6WO_{12} with oxygen vacancies as charge compensating defects, this can be written:

$$2CaO + \frac{1}{3}WO_3 = 2Ca'_{La} + \frac{1}{3}W_W^x + v_O^{\bullet\bullet} + 3O_O^x \qquad (3.1)$$

One may expect an increasing ionic conductivity upon acceptor doping, however, it goes to the opposite way from Fig.3.9 and 3.10. Explanation could be given from two sides: either a decreasing number of protons dissolved or decreasing proton mobility. According to Haugsrud et al., smaller aliovalent cations doped La may change the environment of oxygen vacancies and, thereby, lower the water dissolution. From the mobility side, protons could be trapped by acceptors, forming $(acc' \cdot OH_O^{\bullet})$, and yielding lower proton mobility.

3.4. Defects in $La_{28-x}W_{4+x}O_{54+1.5x}v_{2-1.5x}$

3.4.1. Crystal structure of $La_{28-x}W_{4+x}O_{54+1.5x}v_{2-1.5x}$

Investigations by Magraso et al. have shown that La_6WO_{12} is not stable and the single phase material is obtained when the ratio between La and W is from 5.3 to 5.7, after

sintering at 1500 °C[33]. Combining powder X-Ray and powder neutron diffraction techniques, the structure of lanthanum tungstates with La/W=5.6 has been solved, which is different from the one of Ln_6WO_{12} (Ln=Y, Ho). According to Magraso et al., the materials can be described as a face centered cubic structure with space group $F\bar{4}3m$. Lattice parameter is between 11.173 and 11.188 Å.

When x=0, the ratio between La and W is 7, the perfect parent structure of this material is obtained. The hypothetical structure was modeled by DFT, from Fig. 3.12 (A), we know that there are two oxygen vacancies in this stoichiometric structure [13]. Later, Magraso et al.[21] reported when some W is substituting La, a more stable configuration is obtained. Moreover, La2 site has a distorted environment, which is stable and flexible for W to substitute. Fig.3.12 (B) shows of the structure of $La_{28-x}W_{4+x}O_{54+1.5x}v_{2-1.5x}$ (x=1), which displays that there is one W on La2 site in one unit cell, forming triply effectively charged donor: $W_{La}^{\bullet\bullet\bullet}$.

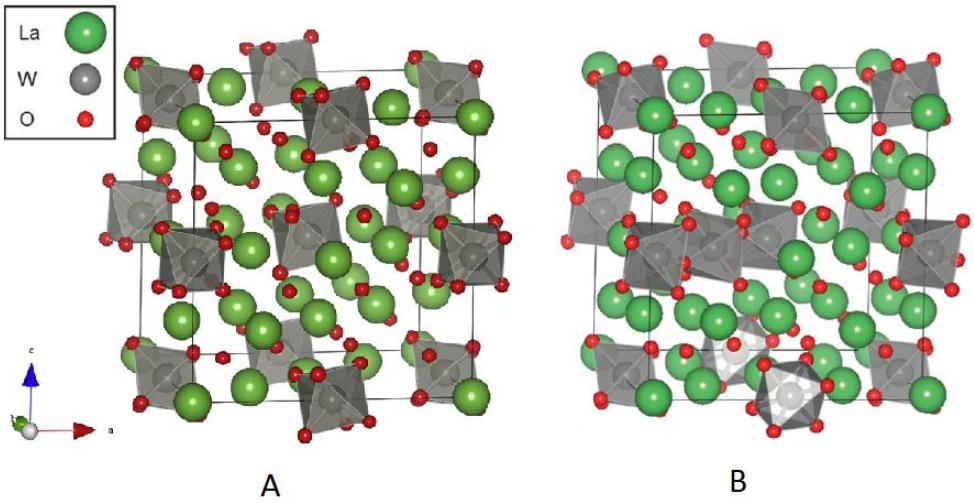

Fig.3.12 (A) $La_{28-x}W_{4+x}O_{54+1.5x}v_{2-1.5x}$ with x=0 from DFT modeling. Two vacant oxygen sites are found[13]. (B) $La_{28-x}W_{4+x}O_{54+1.5x}v_{2-1.5x}$ with x=1 from DFT modeling. One W replaces one La2 site[21].

Table3.1 Structural details of LWO56 obtained though the joint refinement of NPD and PXRD data using the $F\bar{4}3m$ space group with the lattice parameter a=11.187Å.

Label	x	y	z	Wyckoff
La1	0	0	0	4a
La2	x	$\frac{1}{4}$	$\frac{1}{4}$	24g
W1	$\frac{1}{2}$	$\frac{1}{2}$	$\frac{1}{2}$	4b
W2	$\frac{3}{4}$	$\frac{3}{4}$	$\frac{3}{4}$	4d
W3	x	0	0	24f
O1a	x	x	x	16e
O1b	x	x	x	16e
O2a	x	x	x	16e
O2b	x	x	x	16e

3.4.2. Electrical properties of $La_{28-x}W_{4+x}O_{54+1.5x}v_{2-1.5x}$

The electroneutrality for lanthanum tungstate can be read as follow by assuming the concentration of electrons and electron holes are negligible compared with ionic defects:

$$3[W_{La}^{\bullet\bullet\bullet}] + \frac{108}{56}\left[v_{\frac{54}{56}O}^{\frac{108}{56}\bullet}\right] = \frac{4}{56}\left[O_{\frac{54}{56}O}^{\frac{4}{56}\prime}\right] \quad (3.2)$$

The stoichiometry with La/W=5.3, corresponds to x=1.08, and there is 1.08 W ion resident on La site in one unit cell. Similarly, 0.78 W ion substitutes La in one unit cell with ratio La/W=5.7. With the decreasing ratio between La and W, more W replaces La on La2 site, which increases the concentration of $W_{La}^{\bullet\bullet\bullet}$and decreases the concentration of oxygen vacancies.

Oxygen partial pressure dependency on the conductivity of this material was studied, with the ratio of La and W being 5.3, 5.4, and 5.7 respectively (henceforth denoted LWO53, LWO54 and LWO57). Fig.3.13 proves that the more W substitution, the lower is the ionic conductivity at intermediate pO_2 region. More W substitution also increases pO_2 dependency under reducing condition, especially at up to 1000 °C, which indicates n-type conductivity.

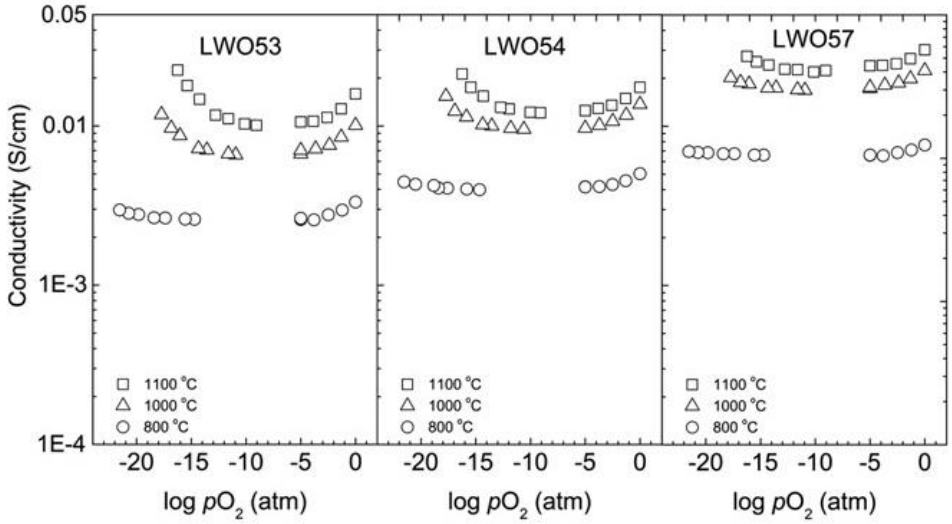

Fig.3.13 pO_2 dependency of the total conductivity of LWO with varying donor concentration[13].

Fig.3.14 shows the total conductivity of LWO53 and LWO57 as a function of 1/T in wet hydrogen condition. Magraso et al. reported that the conductivity at relatively low temperature mainly reflects protons. One may notice that the proton conductivity for LWO57 is higher than for LWO53, due to the higher concentration of oxygen vacancies. At the highest temperatures, the behavior of conductivity shows that electrons dominate, moreover, the total conductivity of LWO53 will surpass the one of LWO57 up to 1200°C. Because the more W substation is introduced into the unit cell, the more donor effect it is.

When water is present, oxygen vacancies may hydrate as:

$$H_2O\ (g) + v_{\frac{54}{56}O}^{\frac{108}{56}\bullet} + O_{\frac{54}{56}O}^{\frac{4}{56}/} = 2OH_{\frac{54}{56}O}^{\frac{52}{56}\bullet} \tag{3.3}$$

Then the electroneutrality will contain protons contribution and read as:

$$3[W_{La}^{\bullet\bullet\bullet}] + \frac{108}{56}\left[v_{\frac{54}{56}O}^{\frac{108}{56}\bullet}\right] + \frac{52}{56}\left[OH_{\frac{54}{56}O}^{\frac{52}{56}\bullet}\right] = \frac{4}{56}\left[O_{\frac{54}{56}O}^{\frac{4}{56}/}\right] \tag{3.4}$$

The total conductivity in of LWO in wet reducing condition, containing contribution

of protons, oxygen vacancies and electrons can be written as follow:

$$\sigma_{tot} = \sigma_{OH_O^{\bullet}} + \sigma_{v_O^{\bullet\bullet}} + \sigma_n \tag{3.5}$$

$$= F\delta_M \left(z_{OH_O^{\bullet}} \mu_{OH_O^{\bullet}} \left[OH_{\frac{54}{56}O}^{\frac{52}{56}\bullet} \right] + z_{v_O^{\bullet\bullet}} \mu_{v_O^{\bullet\bullet}} \left[v_{\frac{54}{56}O}^{\frac{108}{56}\bullet} \right] + z_n \mu_n n \right)$$

By using Eq.(3.4) and (3.5), Magraso et al. extracted thermodynamic and transport parameters form fitting conductivity. For LWO53 and LWO57, the standard hydration enthalpy and entropy are -83 kJ/mol and -125 J/molK, respectively. The enthalpy of mobility of protons and oxygen vacancies are reported as ~60 kJ/mol and ~85 kJ/mol, respectively. The activation energy of electrons including enthalpy of formation and mobility is yielded as ~275 kJ/mol.

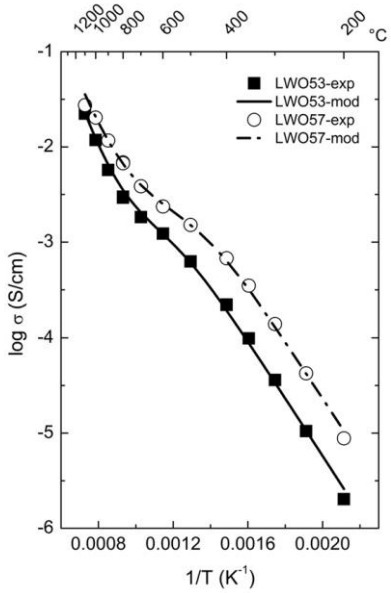

Fig.3.14 Experimental and modeled temperature dependency of the gran interior conductivity of LWO53 and LWO57 in wet hydrogen[13].

3.4.3. Hydration properties of $La_{28-x}W_{4+x}O_{54+1.5x}v_{2-1.5x}$

Hydration of lanthanum tungstate with ratio La/W=5.3 and 5.6 (henceforth denoted LWO53 and LWO56) was studied in detail by Hancke et al.[34]. The number of oxygen vacancies remaining in LWO53(x=1.08) and LWO56(x=0.85) is 0.38 per

formula unit and 0.73 per formula unit, respectively. Fig.3.15 displaces that water uptake of both LWO53 and LWO56 reaches saturation. LWO53 hydrates significantly less than LWO56 does, which agrees well with the decreasing oxygen vacancy concentration. As Hancke et al. reported, for LWO53, 100% of theoretical are hydrated and for LWO56, 66% of theoretical are hydrated (0.48 out of 0.73 oxygen vacancies per formula unit). LWO56 is believed to be metastable at medium temperature, and thus that the ordering of oxygen vacancies and/or precipitation of La_2O_3 decreases the number of oxygen vacancies available for hydration and explains the deviation from full hydration for this composition[34]. Thermodynamic hydration parameters for LWO were determined by different techniques, including thermogravimetric analysis, conductivity measurement and TG-DSC. The standard hydration enthalpy and entropy is reported to be ΔH^0_{hydr} = -90±10 kJ/mol and ΔS^0_{hydr} = -110±10 J/molK.

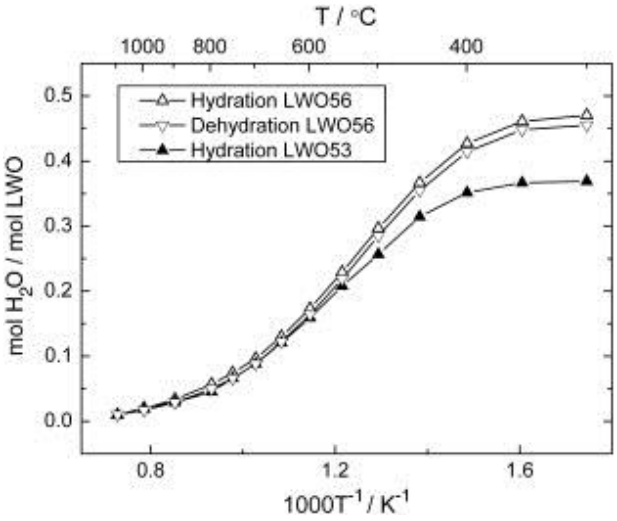

Fig.3.15 The water concentration of LWO53 and LWO56 as a function of reciprocal temperature recorded during hydration. The concentration from a dehydration measurement is also included for LWO56.All the measurements are carried out under oxidizing conditions[34].

4. Experimental

In the thesis, the experimental methods for 2% and 0.5% acceptor-doped $La_{27}W_5O_{55.5}$ are described. After synthesis, two samples were characterized by powder X-ray diffraction (XRD), scanning electron microscopy (SEM) and electron probe micro-analyzer (EPMA). XRD is for checking the crystal structure and single phase of the samples, SEM is for checking the morphology and the element composition of the samples, EPMA providing better results of chemical analysis. The electrical measurements were carried out by an electrical measurement cell and impedance analyzer. The electrical properties were studied by investigating the total conductivity as a function of inverse temperature, oxygen partial pressure, water vapor partial pressure and by deconvoluting impedance spectra. Furthermore, hydration properties of the samples were studied by weighing mass change under wet and dry condition by using thermogravimetry (TG).

4.1. Preparation of samples

4.1.1. Synthesis of samples

Polycrystalline powders of 2% and 0.5% Ba-doped LWO54 were prepared by wet chemical freeze-drying method, which is widely used for preparing ceramics. Wet chemical freeze-drying is a versatile rote which has proven effective to obtain stoichiometrically complex polymetallic systems with milder thermal treatments compared to the conventional solid state route.

Starting materials for synthesizing Ba-doped LWO56 were La_2O_3 (99.99%, Sigma-Aldrich), WO_3 (99.9%, Fluka), $BaCO_3$ (99.98%, Sigma-Aldrich), ammonia (28%, VWR international S.A.S), nitric acid (68%, VWR international S.A.S) and ethylenediaminetetraacetic acid (EDTA, 99.7%, Sigma-Aldrich). Since WO3 and La_2O_3 easily absorb water in room temperature, especially for La_2O_3, raw material needs drying before synthesis. Fig.4.1 shows the temperature profile for drying La_2O_3. La_2O_3 need to be taken out of furnace at 500 °C and be weighed as soon as possible. For WO_3, it needs drying at 200 °C for more than 2 hours.

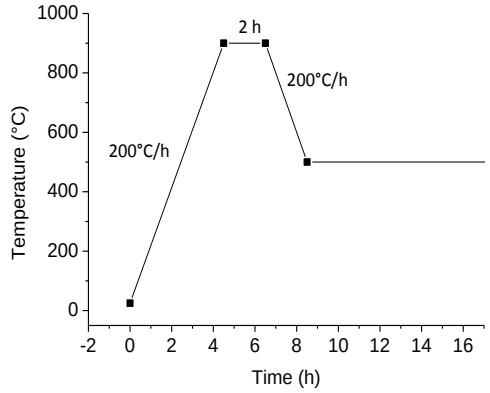

Fig.4.1 Temperature profile of drying La_2O_3.

Synthesis in this work is based on the previous work by Magraso et al.[33]. Stoichiometric quantities of La_2O_3 and $BaCO_3$ were dissolved in diluted nitric acid, all the cations would not dissolved until the solution is clear and transparent, and meanwhile the solution should be acidic. Afterwards, EDTA as a complex agent in 1:1 molar ratio with La was added to it. Solution should be transparent and pH should be adjusted around 6 to 8. Stoichiometric quantities of WO_3 powder were dissolved in diluted ammonia solution. EDTA to metal with ratio 1:1 was introduced to the solution. The two solutions were then slowly mixed together. Adjusted pH until the mixture is neutralized and without visible precipitation. Mixed "perfect" solution were kept stirring under 100 °C to evaporate the solvent to form a gel. Combustion was carried out at 250 °C. Reaction happened during combustion and a black fluffy ash was formed. After roughly grinding, the ash was calcined at 800°C for 5 hours. In order to ensure completely decomposition of organics, these powders are further calcined at 1000 °C for 5 hours. The two temperature profiles are shown in Fig.4.2 and fine white powder was gained after the second calcination.

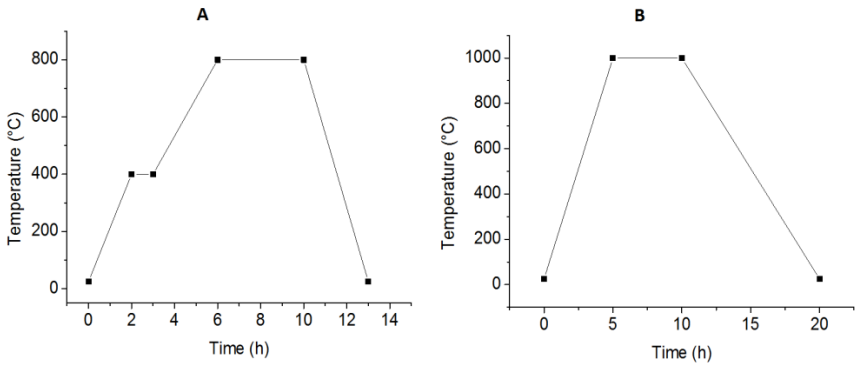

Fig.4.2 Temperature profile of (A) first calcination and (B) second calcination.

4.1.2. Sintering

A 25 mm diameter green body was cold pressed for sintering. Before cold pressing, powders were well grinded by mortar together with drops of binder (Paraloid B-60/B-72, with the quantity of 15 to 20 drops per gram). Mechanical treatments of powders, such as ball milling were not used to avoid contamination. Each Pellet was pressed by using hydraulic press (Specac GS15011) with ~3 tons for ~2 min. The ideal sintering temperature was found to be 1500 °C. The heating rate was set to 300 °C/h, up to 1000 °C, continued heating at 120 °C/h, up to 1500 °C, held for 4 hours, then cooled to room temperature at 300 °C/h as shown in Fig.4.3. After sintering, shrinkage of green bodies was observed.

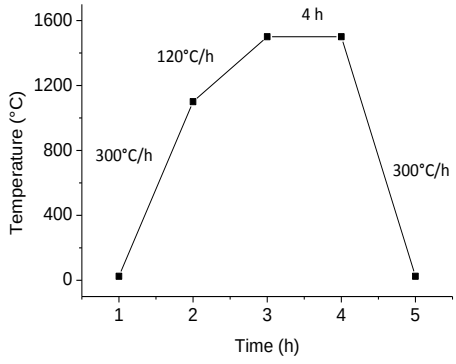

Fig.4.3 Temperature profile of sintering.

4.1.3. Density measurement

Density ρ was calculated by measuring mass and diameter of the pellets. The relative density for all the samples synthesized by the method previously described is around 80%.

Table 4.1 List of the relative density of the samples in this work.

Sample Name	Measured density g/cm^3	Theoretic density g/cm^3	Relative density %
LWO	5.17	6.339[33]	81.56
LBaWO-2%	5.26	6.339[33]	82.58
LBaWO-0.5%	5.55	6.339[33]	87.55

4.1.4. Electrode

Each side of samples needs to be painted by platinum ink (METALOR 6695) in the middle. It could be painted either a square with a side length around 1 cm or a circle with diameter around 1 cm. It was dried at 150 °C for 30 minutes, until the color changed from dark black to light grey. Each side should be painted and dried for twice. Then cut the platinum net to respective shape and size and cover it by Pt ink and dry again. Pellets with electrodes on both sides were left in the furnace at 1000 °C for a couple of hours. Fig.4.4 shows a sample with circular Pt electrode and a sample with square electrode. The left one shows the sample after electrical measurements under reducing condition, which causes the color change.

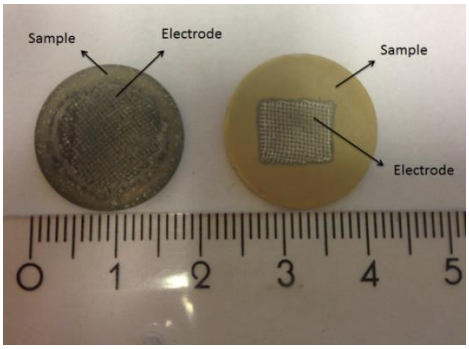

Fig.4.4 Sample with round Pt electrode after electrical measurements (left) and sample with square Pt electrode before electrical measurements (right).

4.2. Characterization of samples

4.2.1. X-ray powder diffraction

X-ray powder diffraction analysis (XRD) was used to study the composition of all the samples and identifies the phase of crystalline after calcination and sintering. Powder of samples after calcination and pellets after sintering were characterized by XRD. For powder preparation, powder were collected and suspended into isopropanol. Then, one or two droplets of the suspension were dripped on the center of quartz substrate. After isopropanol volatilization repeated dripping, until powders well disperse on the substrate. For pellets preparation, sample holder with deep cavity was chosen to hold the pellet stuck in the middle. The pellet should keep in line with the edge of the sample holder.

In this work, Bruker D8 3-circle diffractometer with area detector and nitrogen cryostat was utilized. The scans were performed with angle 2θ, ranging from 10° to 90°.

4.2.2. Scanning electron microscope (SEM)

Scanning electron microscope (SEM) was used to study the microstructure and morphology of the sample after sintering. It images a sample by scanning it with a high-energy beam of electrons in a raster scan pattern. The electrons interact with the atoms that make up the sample, producing a variety of signals such as secondary electrons (SE), backscattered electrons (BSE), Auger electrons, X-rays, which contain information about the sample's surface topography, composition and other properties.

In this work, scanning electron microscopy (FEI Quanta 200 FEG-ESEM) was utilized. Both high vacuum mode and low vacuum mode could be used during SEM characterization. High vacuum is commonly used for conductive material, whereas, for low vacuum, water is introduced to reduce the charge effect in non-conductive material. The material studied in the thesis was known to be non-conductive material. Therefore, low vacuum mode was used during all the characterization. One may note that the images exhibit bright areas where the atomic number is high, and vice versa.

4.2.3. Energy Dispersive X-ray spectroscopy (EDS)

Energy Dispersive X-ray spectroscopy (EDS) was employed to identify the elemental composition of the specimen. The equipment is attached to the SEM. The sample is bombarded by SEM's electron beam and the electron beam excites the atoms in the sample. X-rays are subsequently produced to discharge the excess energy. Atoms can be characterized from different energy of X-rays which form peaks in spectrum. One may notice that each element may have several peaks and peaks from different elements may overlap.

4.2.4. Electron probe micro-analyzer (EPMA)

Electron probe micro-analyzer (EPMA) is a micro beam instrument, a commonly used method for investigating the chemical composition of solid materials. This analytical technique can function as SEM, but having a higher spatial resolution and sensitivity. Better results can be thus provided than with SEM/EDS.

Before using EPMA, the sample needs to be prepared properly. A whole piece or a fragment of sample was placed into a cylindrical mold and fully covered with resin (mixture of Epofix Resin and Epofix Harden with the proportion of 30:4). The sample was left with resin over night until the resin hardened before it was taken out. The sample was grinded with waterproof silicon carbide paper, with steps of finer paper from 220 (U.S. Grain number 220, Diameter/μm 68) to 4000 (U.S. Grain number 1000, Diameter/μm 5). After grinding, the sample was polished on Struer polish cloth with diamond polishing-spray from 6μm to 0.25 μm. Afterwards, a 30nm-60nm carbon film was coated on the surface of sample.

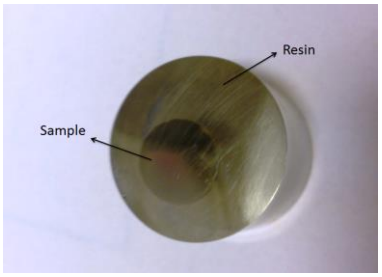

Fig.4.5 Sample in the resin after grinding and polishing.

4.3. Apparatus

4.3.1. Measurement cell

Samples were placed in a measurement cell (ProboStat, NorECs) as illustrated in Fig.4.6, and the electrical properties were characterized under different gas conditions and elevated temperatures. The upper part of the cell tube was put into the furnace. Temperature was monitored and controlled by a PID regulator (Eurotherm 2216e) and the cell is connected to PID regulator using an S-type thermocouple as a sensor. The sample was put on the top of the alumina tube with four Pt wires well touching the two-side Pt electrodes. The sample was finally fixed and well contacted with Pt wires by using a spring loaded alumina disk. Gas flowed through inner gas tube and outer gas tube. At last, the setup was sealed by a quartz tube.

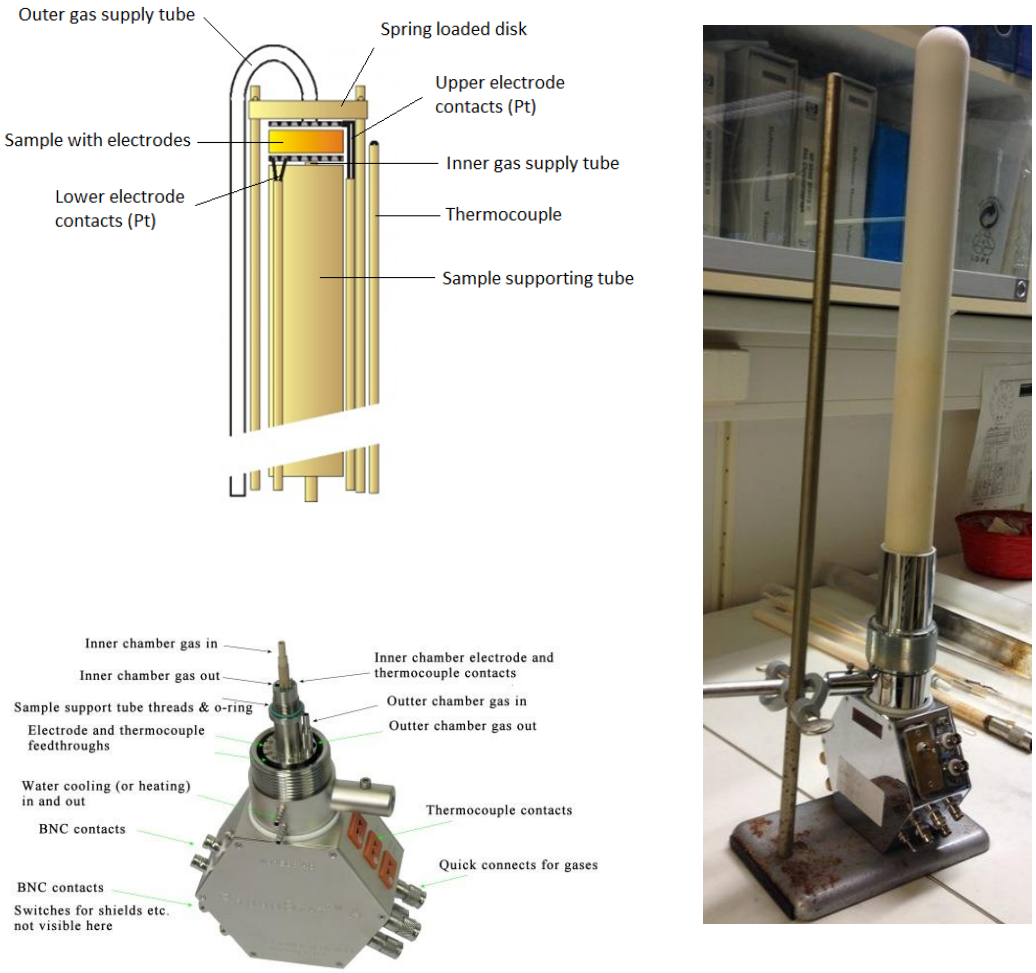

Fig.4.6 Schematic illustration of the Probostat cell (left)[35] and picture of the measuring cell sealed with alumina tube (right).

4.3.2. Gas mixer

For obtaining different gas atmosphere in the measurement cell, an in-house built gas mixer was used, as illustrated in Fig.4.7. The main principle for getting different atmospheres is by diluting the initial gases. In this work, nine flow meters (A-I) separated into four pairs and one single was built for diluting and controlling the gas. pO_2 was set by diluting Gas1 such as O_2, Harmix (5% H_2 in Ar) or H_2 with an inert gases such as N_2, Ar, or He. Here Ar was used for diluting. First diluted gas flowed into MIX1 and further repeatedly diluted into the following MIX2 and MIX3. After MIX3, gas can be chosen to go through the wet stage or dry stage. The wet stage consists of H_2O (saturated KBr) and D_2O (saturated KBr heavy water). A saturated solution of KBr was introduced instead of pure water in order to get a similar water vapor partial pressure, meanwhile avoid water condensation in the cooper tubes. Dry stage was set by gas through the column filled with P_2O_5. The columns with bubbling were equipped with mix gas to check the over pressure. By adjusting flow meters, one can control the quality of the gas and by using software Gasmixer 0.5000, pO_2 and pH_2O could be calculated. One may notice, two different materials were used as floating balls inside the flow meters, one is made by light glass, the other is made by heavy tantalum, the latter one is five times heavier than the former one.

In this work, pO_2 in the measuring cell can be controlled in the range of ~1 to ~10^{-30} atm by using O_2/Ar, Harmix/Ar and H_2/Ar. pH_2O can be adjusted in the range of ~$2 \cdot 10^{-2}$ to ~$2 \cdot 10^{-5}$ by using O2 dried and/or humidified through the stage previously mentioned.

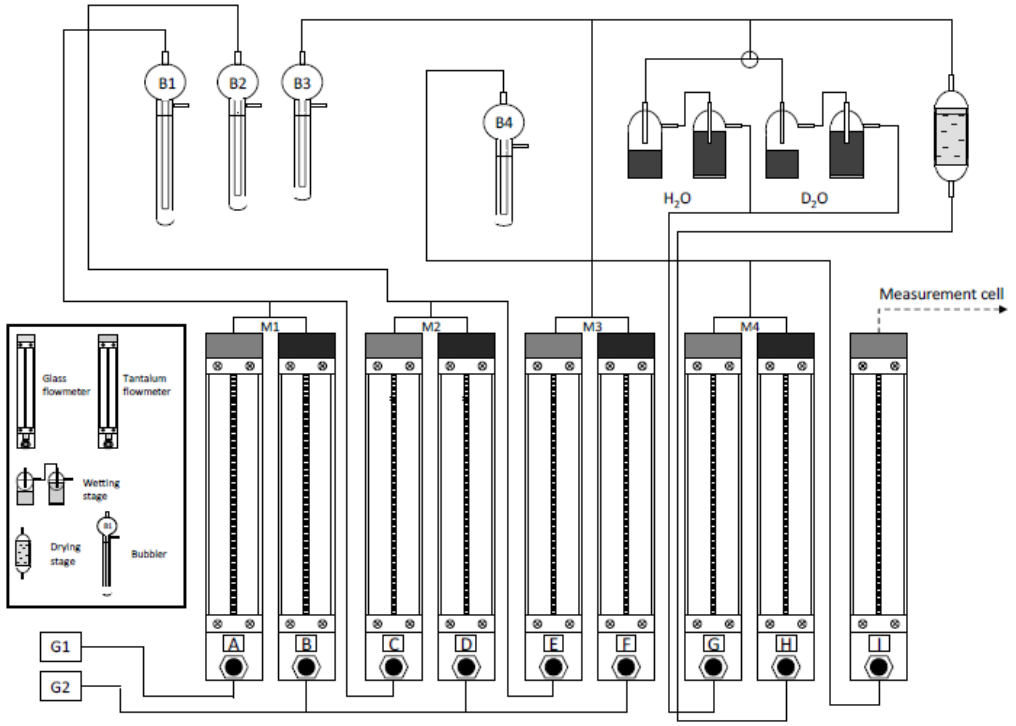

Fig.4.7 Schematic illustration of gas mixer with four mixing stages[36].

4.3.3. Thermogravimetry (TG)

The hydration properties of the sample were studied by thermogravimetry (TG) in the temperature range from 1100 °C to 300 °C both in dry O_2 and wet O_2 (pH_2O=0.02 atm). In this work, Netzsch STA 449 F1 Jupiter was employed. TG is a method of thermal analysis to determine the mass loss or gain as a function of temperature due to the decomposition and/or oxidation. Here, we used powder samples with a minimum sample load of 600 mg and maximum sample load of 2800 mg. Sample holder as illustrated in Fig.4.8 (left) was directly connected with the balance. Powder samples were put From Fig4.8 (right), one may notice that there are three gas tubes connected to TG, purge1, purge2, and protective gas. In my work, only purge1 (controlling wet stage) and protective gas (controlling dry stage) were used because measurement was carried out under one gas constant condition.

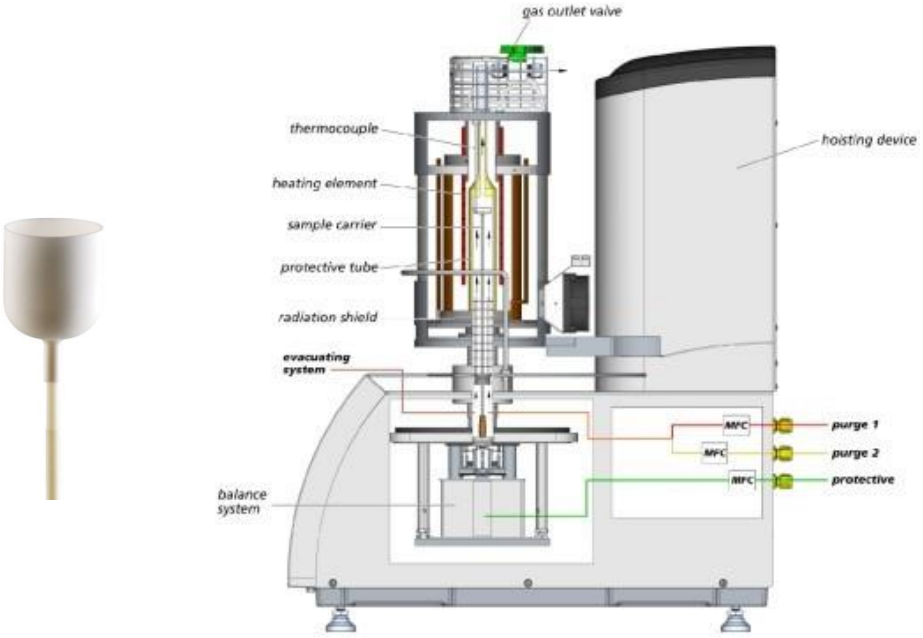

Fig4.8 Sample holder used in thermogravimetry (left) and schematic illustration of thermogravimetry analyzer, Netzsch STA 449 F1[37]

Fig.4.9 shows the temperature profile of TG progress. In a real measurement, all the parameters could be adjusted according to the requirement. For instance, in this case, in order to make sure that particles with different sizes have enough time to reach the equilibrium, equilibrium time was enlarged from 2h or 3 to 4h or 5h, especially down to 500°C.

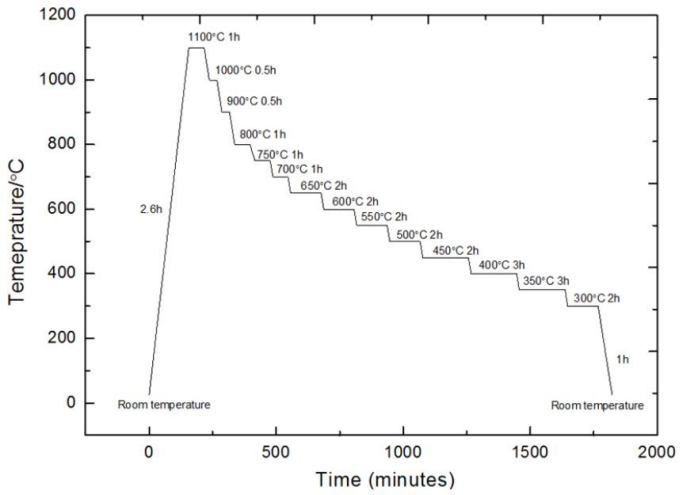

Fig.4.9 Temperature profile of thermogravimetric measurement of.

4.4. Electrical measurements

4.4.1. 4-wire 2-electrode measurements

In this work, 4-wire 2-electrode measurements were carried out. In this method, the resistance of current wires is removed and only electrodes and sample are included in the measurement, as shown in Fig.4.10.

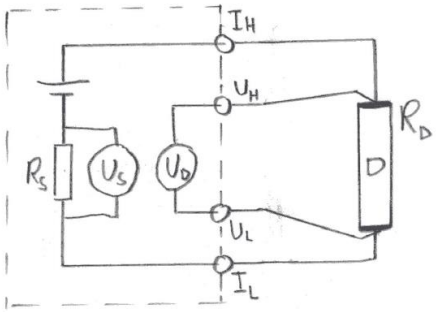

Fig.4.10 Illustration of a 4-wires 2-electrode measurement, taken from[11]

The conductivity of the sample in different atmospheres was measured by an impedance analyze (Solartron 1260) with a 10 kHz constant frequency of and 0.5 V oscillation voltage. In order to identify the contribution of bulk, grain boundary and electrode, impedance sweeps were measured with a frequency ranging from 1 Hz to 1 MHz.

The conductivity of the sample was measured directly with the geometric correction by the system, which can read as:

$$\sigma_g = G\frac{d}{\pi r^2} \tag{4.1}$$

where G is the conductance, d is the thickness of the sample, and r is the average radius of the electrodes.

The specific conductivity need to be corrected by the relative porosity, which can be written as:

$$\sigma_{specific} = \frac{\sigma_g}{\rho^2} \tag{4.2}$$

where ρ is the relative density, obtained from:

$$\rho = \frac{\rho_{sample}}{\rho_{reference}} \tag{4.3}$$

5. Results

In this part, results from 2% and 0.5% Ba-doped $La_{27}W_5O_{55.5}$ (henceforth denoted LBaWO-2% and LBaWO-0.5%, respectively) are given. After characterization, the results and data from temperature ramp, pO_2 dependency, pH_2O dependency and impedance spectra are presented. Some results from TG are presented at the end.

5.1. Characterization

5.1.1. XRD

After sintering at 1500°C, each sample was characterized by XRD and compared with the reference pattern[38] to check if the material was single phase. Fig.5.1 and Fig.5.2 show that the main peaks of both LBaWO-2% and LBaWO-0.5% appear at the positions as for the reference. However, secondary phases were detected in both of them, where the amount of secondary phase increases with the level of doping.

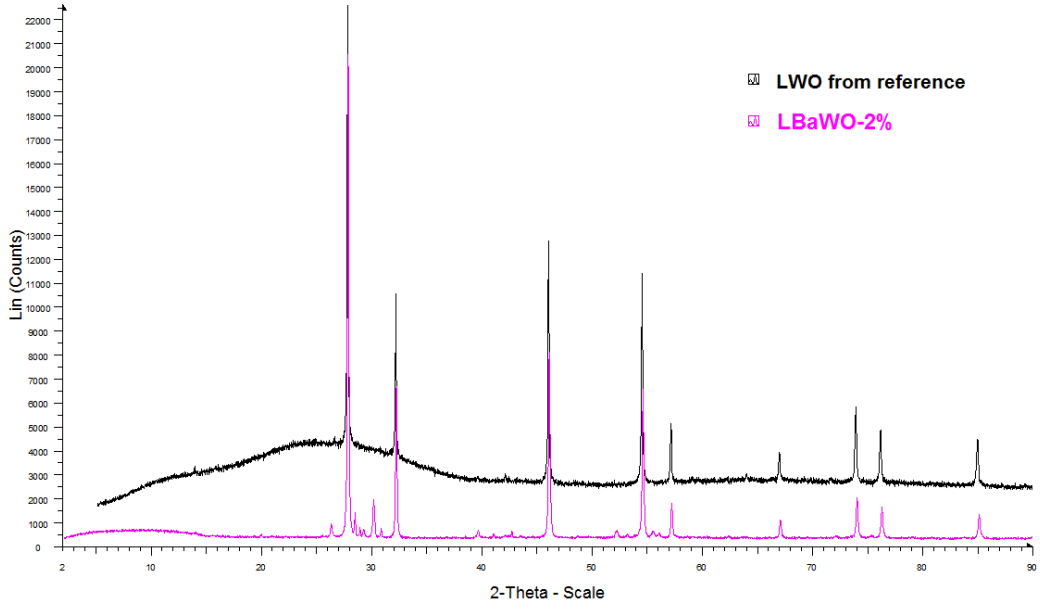

Fig5.1 XRD pattern measured at room temperature of LBaWO-2% after 1500 °C sintering compared with LWO from reference pattern[38].

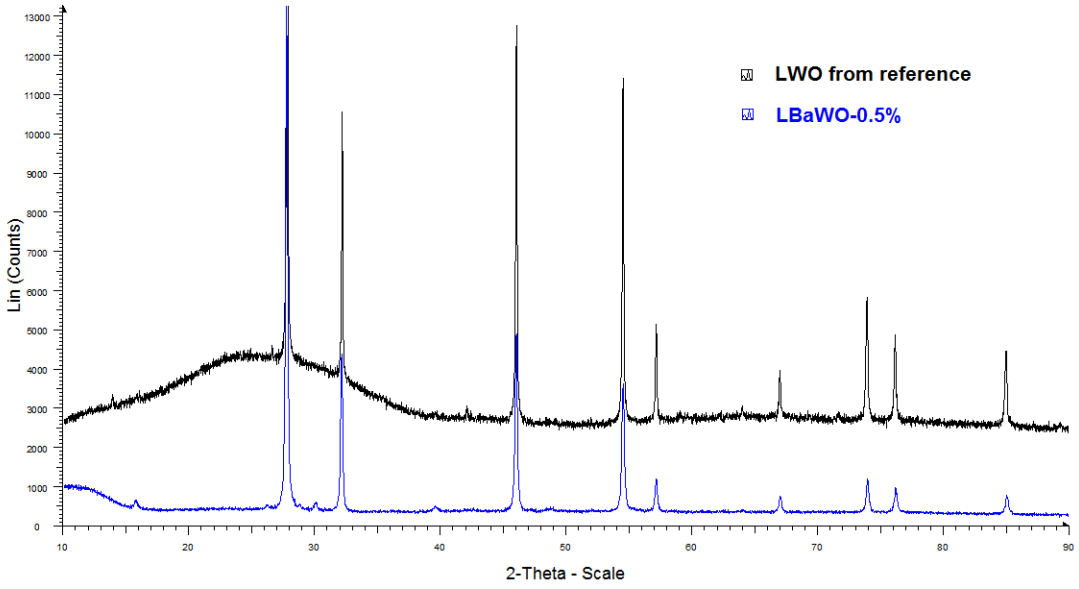

Fig5.2 XRD pattern measured at room temperature of LBaWO-0.5% after 1500 °C sintering compared with LWO from reference pattern[38].

5.1.2. SEM

In order to achieve a good contrast for these low electronic conductivity samples, low vacuum was used during SEM characterization. Fig.5.3 (a)-(d) display BSE images of LBaWO-2% and LBaWO-0.5%. Images show that two dense samples are both with black points well distributed on the surface. Grain size of each material is approximately 5μm to 10μm, there is no obvious size change with doping level.

Fig.5.4 and Table 5.1 show the data from EDS-analysis for LBaWO-2%. In Table5.1, 2% Ba-doped LWO shows that the concentration of Ba inside the grains is ~1.7% indicating that this is the doping level of the material. However, the ratio of La/Ba is ~7.5% in the black points, showing that these are the black points are Ba-rich phase. Compare to the matrix around LBaWO-0.5% with smaller doping level shows less amount of the Ba-rich phase than the LBaWO-2%. From Fig.5.4, one may notice that the peaks of La and Ba are almost overlapping, which may lead to relatively high uncertainties with to determining the actual composition from EDS.

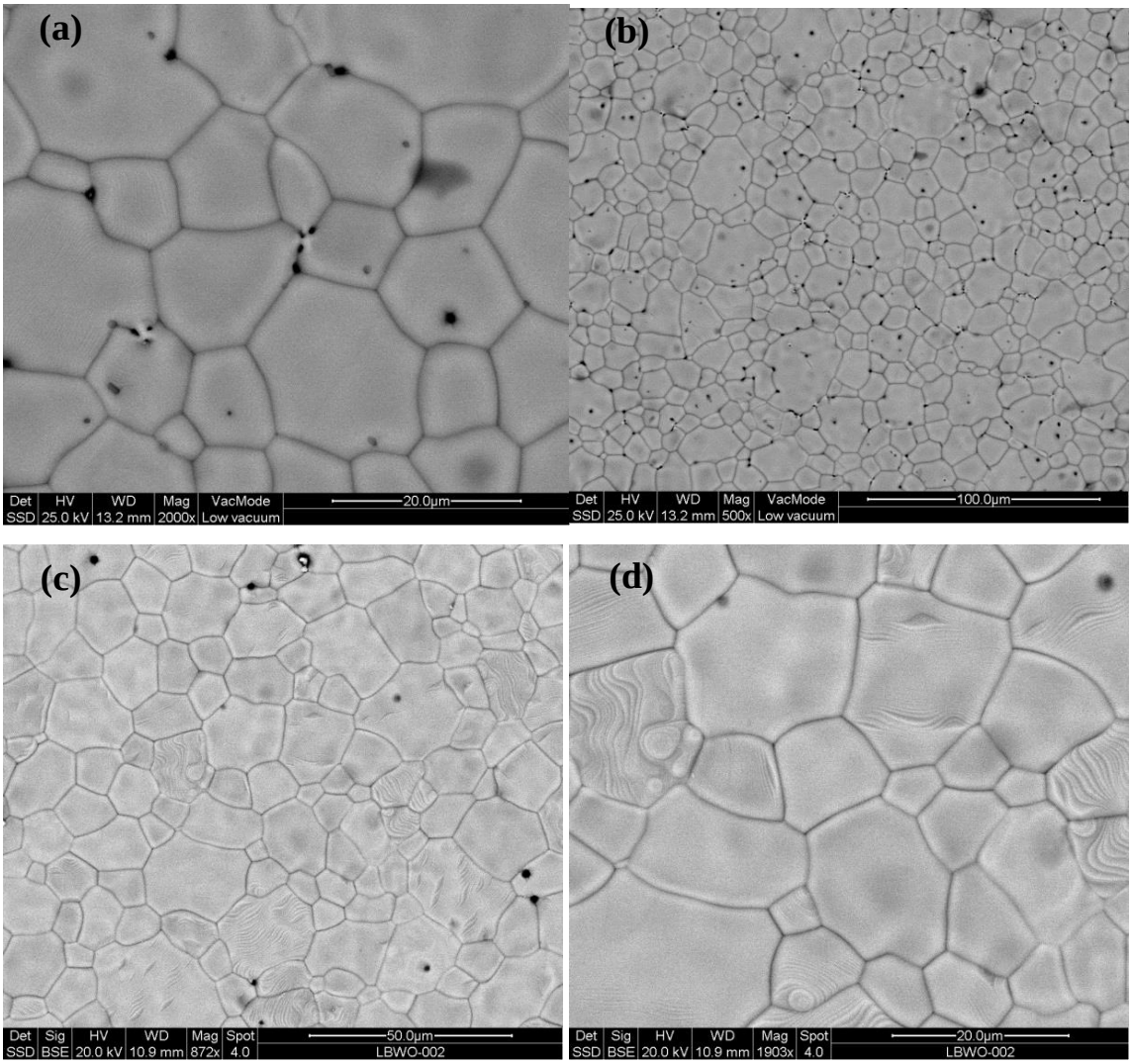

Fig.5.3 Image from SEM was taken under low vacuum with signal from SSD. (a)-(b) are SEM images of LBaWO-2% with different magnifications.(c)-(d) are SEM images of LBaWO-0.5% with different magnification.

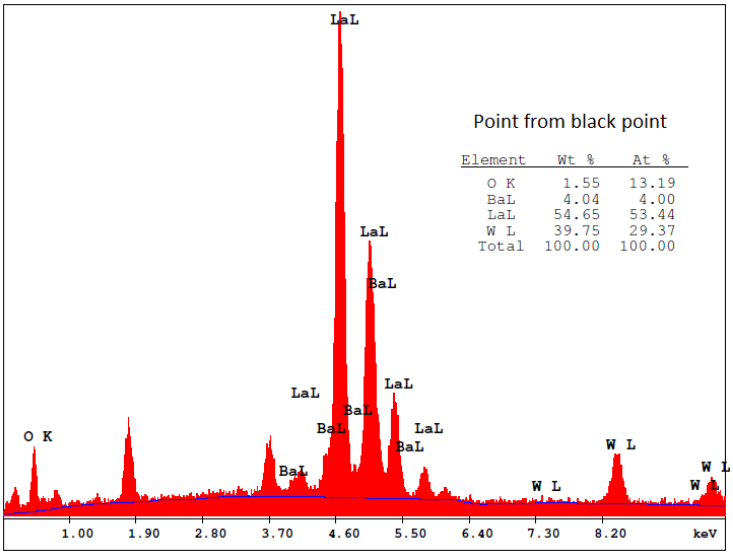

Fig.5.4 EDS results of black point taken from LBaWO-2%.

Table 5.1 Atomic percentage of different elements from the black point and the grain of LBaWO-2% using EDS.

Part	La L Atom %	Ba L Atom %	W L Atom %	O K Atom %
Black point	53.44	4	29.37	13.19
Grain	49.02	0.85	7.69	42.44

5.1.3. EPMA

In order to get more accurate results, EPMA was employed to characterize the elemental composition. Fig.5.5 shows the BSE image of LBaWO-2% obtained in the EPMA. Here we find, in addition to the black points also uniformly distributed white points, and the main matrix can be clearly separated into two with different colors, light grey and dark grey. The black points were proven to be porosity, the amount of which corresponds well to the calculated density. The composition in atomic percentage of different elements of the dark grey part, the light grey part and the white points is presented in Table 5.2. For the dark grey part, there is ~0.3% Ba-doped on La site, and the ratio of La/W is ~5.6 instead of the nominal 5.4 (henceforth, ratio of La/W means La sites and W sites). For the light grey part, the ratio of Ba/(Ba+La) is ~6.8% and the ratio of La/W changes to ~5.0. The exact amount (in area%) of these two parts, the light and the dark grey, could not be told from the image. Comparing

the composition of these two parts, more Ba accumulates in the light parts than the dark ones and the ratio of La/W increase when the color is getting darker. The white points are confirmed to be a secondary phase which from the ratio between the cations could be that La_2BaWO_7 formed during synthesis. Turning back to the Ba-rich phase observed in SEM image, it wasn't detected from EPMA. The reason for this is that the sample prepared for SEM is without grinding and polishing, thereby representing surface after sintering. It also needs to be stated that although the results from EPMA is more reliable than SEM-EDS, there are uncertainties, especially in this case due to the small doping level and the peak overlapping.

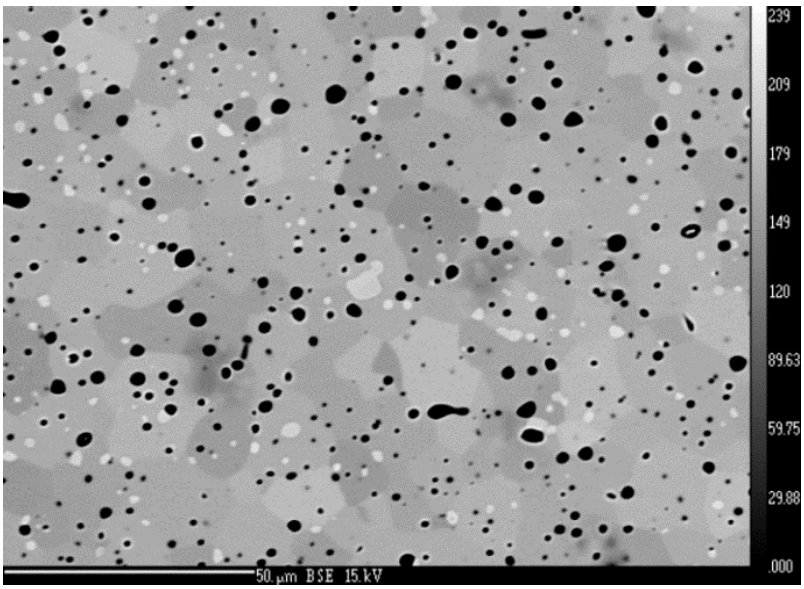

(a)

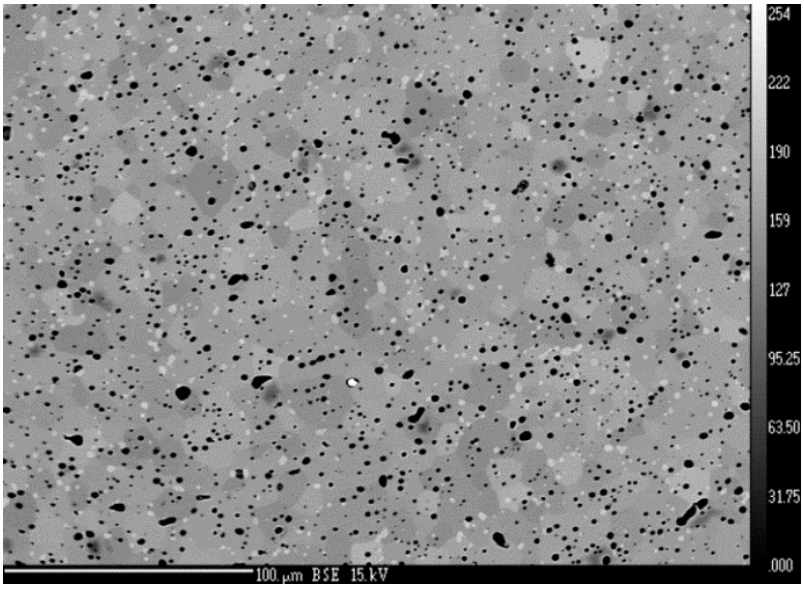

(b)

Fig.5.5 Image from EPMA of LBaWO-2% with different magnifications.

Table 5.2 Atomic percentage of the different elements from the three parts with different color in LBaWO-2% using EPMA.

	Dark Grey Part		Light Grey Part		White Point	
	Weight%	Atomic%	Weight%	Atomic%	Weight%	Atomic%
La	67.1224	31.0892	60.9123	28.2804	40.6039	19.1539
W	15.794	5.527	18.124	6.3576	24.5331	8.7438
Ba	0.1805	0.0845	4.1193	1.9344	17.9614	8.5701
O	15.7419	63.2993	15.7361	63.4277	15.5133	63.5322
Total	98.8387	100	98.8916	100	98.6117	100

Three parts with different color are seen from the EPMA mapping image of LBaWO-0.5% shown in Fig.5.6. The black regions again correspond to porosity, and in addition, two grey parts with lightness difference could be seen. From Table 5.3, we see that the composition of these two parts is similar. This is different compared to LBaWO-2% where the composition of the two grey parts clearly was different. On this basis it is believed that this difference in contrast rather represents a difference in orientation rather than an actual compositional difference. Around 0.4% Ba was successfully doped on La site and the ratio between La and W is ~5.6-5.7. Moreover, no secondary phase was detected (even the lightest part in the image was detected to be the same phase).

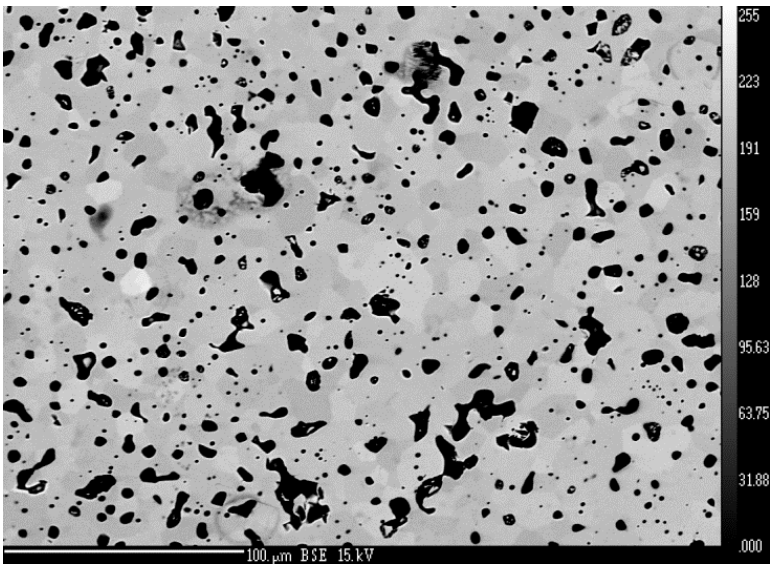

Fig.5.6 Image from EPMA of LBaWO-0.5%.

Table 5.3 Atomic percentage of the different elements from the two parts with different color in LBaWO-0.5% using EPMA.

	Dark Grey Part		Light Gery Part	
	Weight%	Atomic%	Weight%	Atomic%
La	66.6555	31.1248	66.8394	31.1195
W	15.8487	5.48371	15.6545	5.4839
Ba	0.2682	0.1267	0.2821	0.1328
O	15.606	63.2649	15.6515	63.2638
Total	98.0731	100	98.3626	100

5.2. Electrical characterization

5.2.1. Impedance spectroscopy analysis

The impedance spectra of LBaWO-2% and LBaWO-0.5% were recorded at different temperatures and different atmospheres during the electrical measurements in order to distinguish the contribution from bulk, grain boundary and electrode on the conductivity. The frequency was set to 10 kHz for the constant frequency measurements and the frequency range of sweep was chosen from 5Hz to 1MHz. The oscillation voltage was set to 0.5V.

Fig.5.7 (a) and (b) show the impedance spectra of LBaWO-2% from 800 °C to 400 °C in wet O_2. No well-defined semicircle starting from origin can be seen within this range of temperature. Therefore, the spectra was deconvoluted with equivalent circuit $R_1(R_2Q_2)(R_3Q_3)$. Upon deconvolution, R_1 is the resistance of bulk interior, and the corresponding capacitances of the constant phase elements for (R_2Q_2) and (R_3Q_3) were determined to be ~10^{-11} Fcm^{-1} and ~10^{-6} Fcm^{-1}, respectively. Capacitances in the pF range are generally attributed to bulk response, while those in the nF and μF range are attributed to grain boundary and electrode, respectively. In Fig.5.7 (b), the green one shows the sweep at 400°C, and a flat region between grain boundary and electrode can be clearly seen. Therefore one more subcircle (RQ) element was added

to get the better fit. Capacitor of the first semicircle was determined to be ~10^{-10} Fcm^{-1}, whereas that of the second semicircle was ~10^{-9} Fcm^{-1}. Consequently, it was concluded to treat this essentially flat region as transition between the part representing the grain boundary and electrode processes.

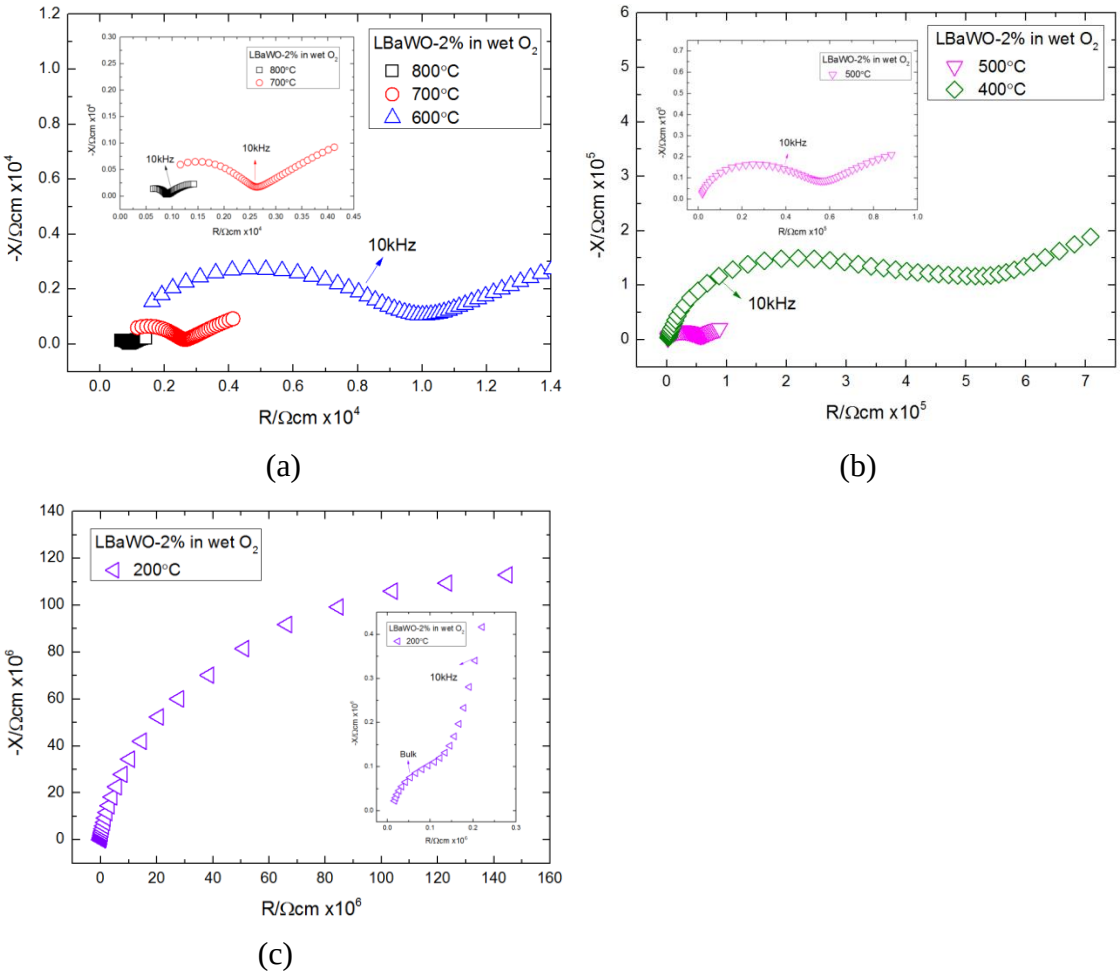

Fig.5.7 Selected impedance spectra of LBaWO-2% at various temperature in wet O_2, measured from 1MHz to 5Hz. The spectra have been corrected for sample geometry and porosity. (a) spectra from 600 °C to 800 °C. (b) spectra from 400 °C to 500 °C.(c) spectrum at 200 °C.

Fig.5.7 (c) shows the sweep of LBaWO-2% in wet O_2 at 200 °C including an inset where the high frequency part of the spectrum is magnified revealing also the semicircle representing the grain interior. Consequently this strengthens the argument that the intercept of the first semicircle for the sweep at high temperature correspond to the bulk resistance of the specimen. An equivalent circuit of two parallel subcircuit

in series $(R_1Q_1)(R_2Q_2)$, (R_1Q_1) was chosen to be appropriate for the spectrum. After deconvolution, the capacitance of the first small semicircle was in the pF range, showing that this actually was bulk. If one compares the two semicircles in Fig5.7(c), the LBaWO-2% has a huge grain boundary resistance compared to the bulk resistance

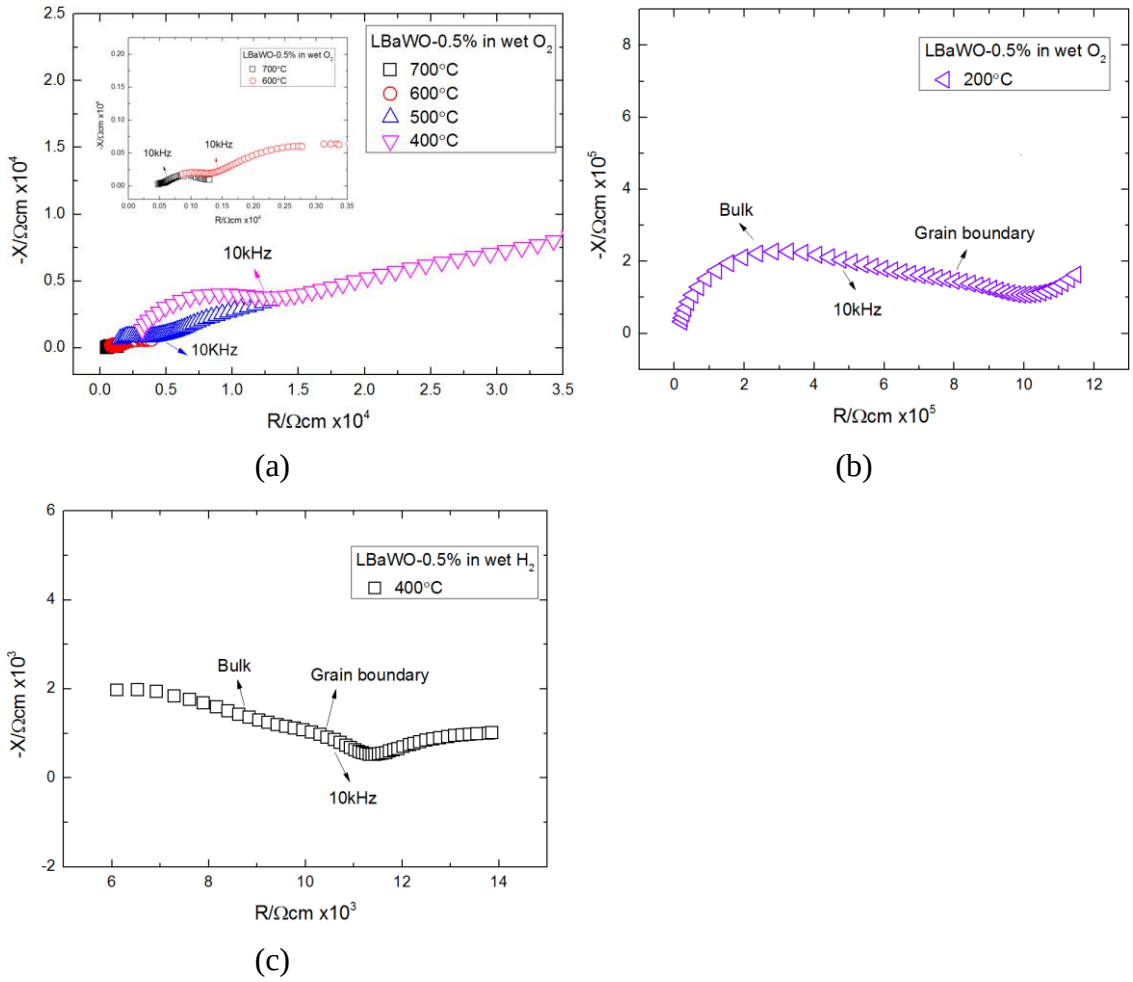

Fig.5.8 Selected impedance spectra of LBaWO-2% at various conditions measured from 1MHz to 5Hz. The spectra have been corrected for sample geometry and porosity. (a) is the spectra from 400 °C to 700 °C in wet O_2. (b) is the spectra at 200°C in wet O_2.(c) is the spectra at 200 °C in wet H_2.

Fig.5.8 (a) displays the impedance spectra of LBaWO-0.5% from 700 °C to 400 °C in wet O_2. Similar as for LBaWO-2%, none of the spectra start from the origin. Comparing the spectra at the same temperature from Fig.5.7 (a)-(b) and Fig.5.8 (a),

the grain boundary resistance of the LBaWO-0.5% can be observed to be around one order of magnitude smaller than for LBaWO-2%. The resistance of grain boundary increases with increasing Ba doping level. The equivalent circuit $R_1(R_2Q_2)(R_3Q_3)$, as for LBaWO-0.5% was found to be appropriate for temperature up to 300 °C.

Fig.5.8 (b) presents the sweep of LBaWO-0.5% down to 200 °C, and an equivalent circuit of corresponding to $(R_1Q_1)(R_2Q_2)$ was applied for deconvolution. Again Comparing with corresponding spectra for LBaWO-2% (Fig.5.7 (b)), the spectra from Fig.5.8 (b) shows more visible bulk semicircles and considerably smaller grain boundary semicircles.

Fig.5.8 (c) shows the spectra of LBaWO-0.5% in reducing atmosphere at 400 °C. After deconvolution, the first incomplete semicircle was confirmed to represent the bulk.

5.2.2. Temperature dependence of the conductivity

Temperature dependence of the conductivies of LBaWO-2% and LBaWO-0.5% were recorded in oxidizing atmophere at ~1 atm oxygen. The two samles with different doping level show a different total conductivity behavoir. This is illustrated in Fig.5.9 (a) and (b), showing the logarithm 10 kHz constant frequency conductivity of respectively LBaWO-2% and LBaWO-0.5% as a function of inverse temperature from 300°C to 1000°C in both dry O_2 and wet O_2. First focusing on LBaWO-2% (Fig.5.9 (a)), the conductivity in wet O_2 is a bit higher than in dry O_2 from 1000 °C down to ~400 °C, whereas below ~400 °C, this changes and the conductivity in dry starts to go above in wet O_2. Spectra of selected temperatures were deconvoluted as described in chapter 5.2.1. The bulk conductivity in wet O_2 estimated from these spectra is included in the figure and shows a different behavior upon temperature than the total conductivity, and difference increase with decreasing temperature.

Fig.5.9 (b) shows similarly the logarithm conductivity at 10 kHz constant frequency of LBaWO-0.5% as a function of inverse temperature from 300 °C to 1000 °C. Conductivities under wet and dry condition are almost overlapping for temperatures

up to ~700 °C. Below ~700 °C, the conductivity in wet condition starts to go higher than the one in dry condition and the effect increases with decreasing temperature. Comparing the total conductivity measured in wet O_2-0.025H_2O atm and O_2-0.025D_2O atm, it is clear that there is a significant isotope effect in the same temperature regime that there is a difference between wet and dry conditions revealing that proton are important charge carriers below ~700 °C. The total conductivity at 700 °C is ~2.3·10^{-3} Scm^{-1}. The bulk conductivity deconvoluted from impedance data is included in Fig.5.9 (b) and it is clear that the total conductivity of LBaWO-0.5% in wet O_2 at 10 kHz frequency can mainly be attributed to bulk interior. This behavior is very different from the data from LBaWO-2% where the resistance of the grain boundaries is dominating the 10 kHz total conductivity values.

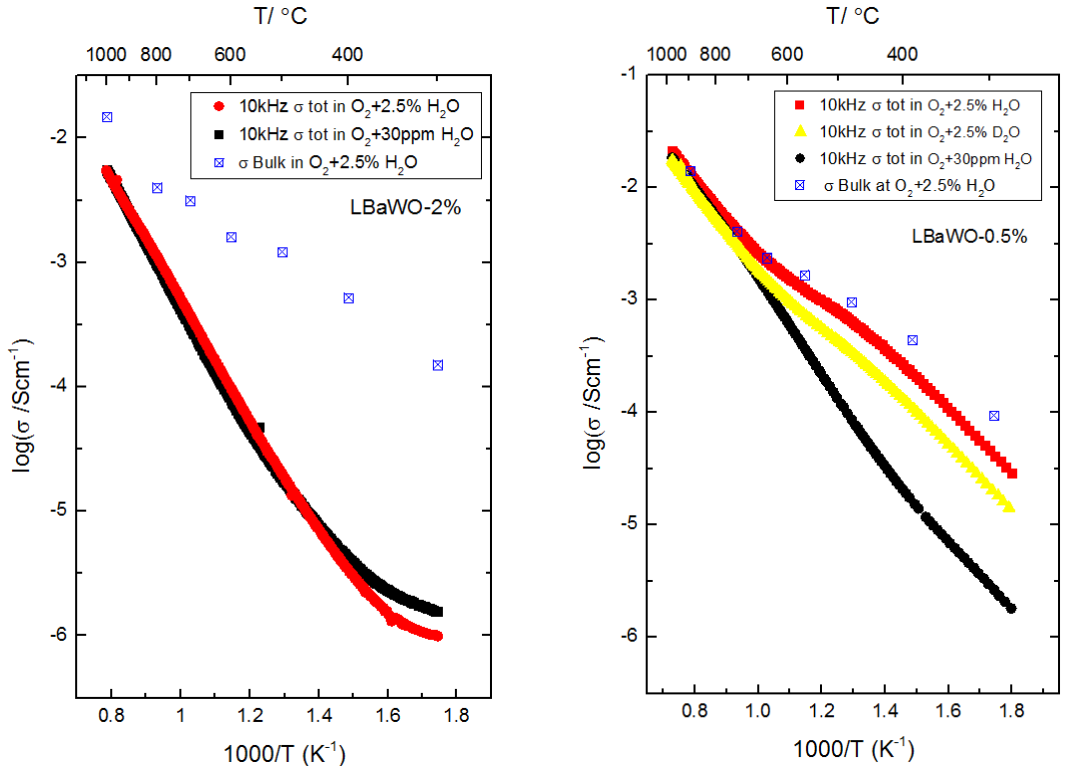

Fig.5.9 Logarithm of total conductivity as a function of the inverse absolute temperature at 10 kHz constant frequency from 300 °C to 1000 °C. (a) LBaWO-2% in O_2-0.02H_2O atm, O_2-~3·$10^{-5}$$H_2O$ atm and bulk of LBaWO-2% in O_2-0.02H_2O atm. (b) LBaWO-0.5% in O_2-0.02H_2O atm, O_2-~3·$10^{-5}$$H_2O$ atm, O_2-0.02D_2O atm and bulk of LBaWO-2% in O_2-0.02H_2O atm.

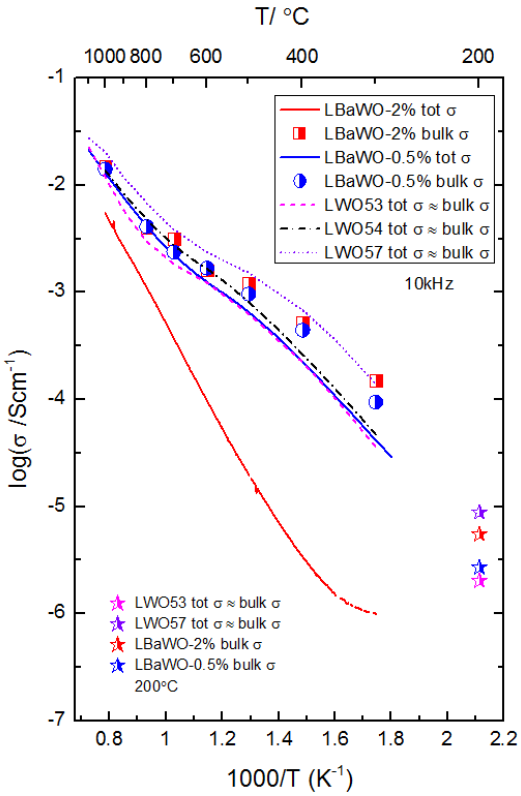

Fig.5.10 Logarithm of conductivity as a function of the inverse absolute temperature at 10 kHz constant frequency for different materials in various atmospheres. Solid curves are LBaWO-2% and LBaWO-0.5% measured under O_2-0.025H_2O atm, scatters are the bulk of these two samples after deconvolution, and others are the undoped LWO taken from reference[39] measured under H_2-0.025H_2O atm.

Fig.5.10 presents a comparison of 10 kHz total and bulk conductivity of LBaWO-2% and LBaWO-0.5% in wet O_2 with 10 kHz total conductivity of LWO53, LWO54 and LWO57[39] in wet H_2. According to the Magraso, the total conductivity of LWO corresponds to the bulk conductivity and there is, moreover, essentially no difference between the conductivity in wet O_2 and wet H_2. Therefore a comparison between the seven data sets can be justified. Both the doped versions of LWO show slightly lower conductivities than the undoped LWO54. The conductivity of LBaWO-0.5% behaves similar with the LWO, whereas the total conductivity of LBaWO-2% is at the maximum ~1.5 orders of magnitude lower than these two. The bulk conductivity of all three behaves similarly. Since the characterization results from EPMA shows that the ratio of La/W for both samples has changed, it is necessary to compare the conductivity of two samples with undoped materials with different ratio of La/W. In this respect, one may note that LBaWO-0.5% has a similar behavior as LWO53 at

temperature below to ~600 °C. Up to ~700 °C, the behavior gets closer to that of LWO54. Moreover, LWO57 shows higher conductivity than the others through all the temperature.

Since down to 200 °C, more reliable bulk conductivity of these to sample could be obtained as previously mentioned. The bulk conductivity of LBaWO-2%, LBaWO-0.5%, LWO53 and LWO57 was also plotted in Fig.5.9. They correspond with the curves in the same color. From the magnitudes of these four bulk conductivities, one may believe that the bulk conductivities of these two samples are decent.

5.2.3. pO_2 dependence of conductivity

Fig.5.11 (a) displays the logarithm of the total conductivity (10 kHz) of LBaWO-2% as a function of logarithm pO_2 in wet O_2 every 200 °C, from 1000 °C to 600 °C. pO_2 dependence in reducing atmosphere was not done. The conductivity of this sample increases with oxygen partial pressure and the dependency gets more significant with increaing temperature and for higher pO_2. At 1000 °C, the slople of logrighm conductivity was determined to be $\sim\frac{1}{20}$. Fig.5.11 (b) displays the pO_2 dependence of the bulk conducitivity of LBaWO-2% at 1000 °C and 800 °C, which was obtained by deconvolution with equivalent circuit $R_1(R_2Q_2)(R_3Q_3)$. The bulk conductivity is higher than the total conductivity, and the difference between them at these two temperatures matches with the plot shown in Fig5.9 (a). Bulk conductivity also shows visible pO_2 dependence at the temperature up to 800 °C. Since EPMA shows that the main part of the sample consists of a phase with La/W≈5.0, the pO_2 dependence of LWO50 from reference was plotted in Fig.5.11 (c) for comparison. The total conductivity of LWO50 in oxidizing region has a different behavior with the bulk conductivity of LBaWO-2%.

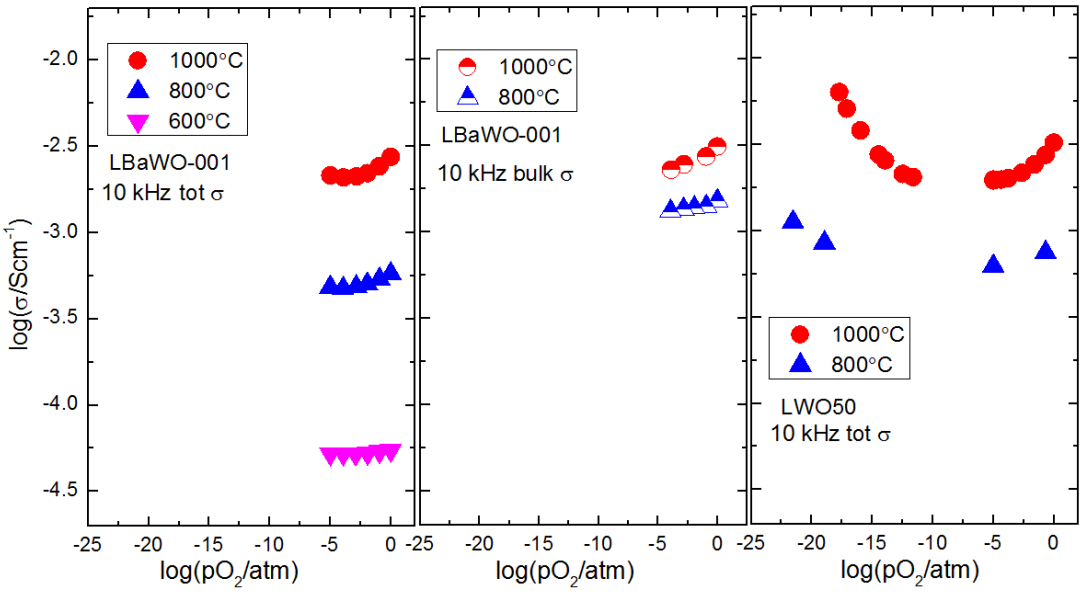

(a) (b) (c)

Fig.5.11 Logarithm of conductivity as a function of logarithm pO_2 at 1000 °C and 800 °C. (a) the total conductivity of LBaWO-2%, (b) the bulk conductivity of LBaWO-2%, (c) total conductivity of LWO50 from reference[39].

Logarithm conductivity (10 kHz) of LBaWO-0.5% as a function of logarithm pO_2 under both reducing atmosphere (H_2 and Hamix) and oxidizing atmosphere (O_2) from 600 °C to 1100°C is shown in Fig.5.12. The slope of the conductivity at 1100 °C in reducing part is about~- $\frac{1}{17}$, and the one at oxidizing part is around ~$\frac{1}{18}$. pO_2 dependence increases with increasing temperature under both reducing and oxidizing regions. Here, at 1100 °C it shows much lower conductivity in oxidizing section than in reducing section due to that sample was left at 1100°C in H_2 for days.

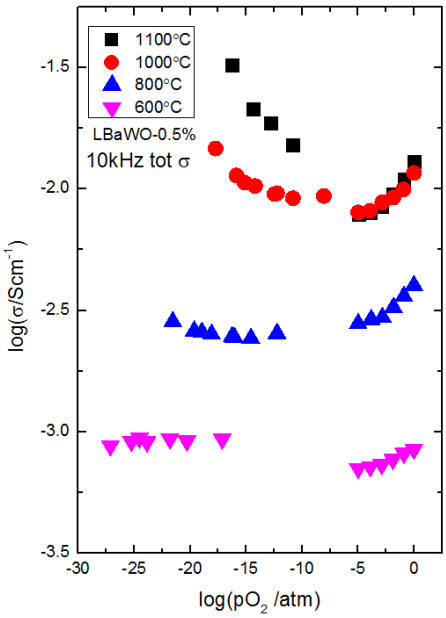

Fig.5.12 Logarithm of total conductivity as a function of logarithm pO_2 from 600 °C to 1100°C.

5.2.4. pH_2O dependence of conductivity

Logarithm of the total conductivity (10 kHz) of LBaWO-2% shows no visible pH_2O dependence in wet O_2 from 1000 °C to 400 °C as shown in Fig.5.13 (a). Magnified plots of logarithm total conductivity at 600 °C and 400 °C show that the at low temperature, conductivity of the material decrease with the increasing pH_2O, and a turning point appears at 600 °C. This unexpected phenomenon might be atrributed to the measurements error or not reaching equillibium, etc.(more explaination will be discussed in the latter chapter).

Spectra under different water vapor partial pressure at 600 °C were deconvoluted to get the bulk contribution and grain boundary contribution. It needs to be clarified that grain boundary conductivities reported here are not specific values. From Eq. (2.51), specific grain boundary data is the product of the C_1 and C_2. Since $R_1(R_2Q_2)(R_3Q_3)$ was chosen to be the equivalent circuit here, C_1 could not be obtained, therefore, it has been assumed that σ_2 corresponds σ_{gb}in this situation to get an estimate of the grain boundary conductivity and more importantly how it behaviors upon changes in the measuring condition. From Fig.5.13 (b), bulk conductivity goes almost one order magnitude higher than the total conductivity, which matches with the results in

Fig.5.9 (a). Bulk conductivity also shows pO_2 dependence at this temperature, while grain boundary does not.

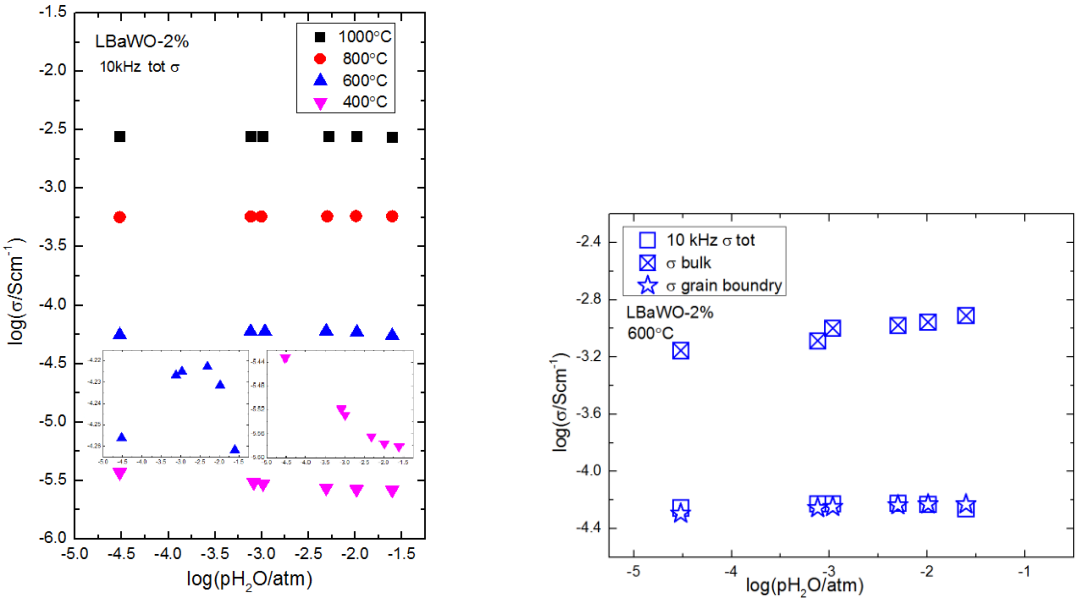

(a) (b)

Fig.5.13 (a) Logarithm of total conductivity of LBaWO-2% as a function of logarithm pH_2O from 400 °C to 1000 °C, with the plots of 400 °C and 600 °C being magnified in it. (b) Bulk and grain boundary conductivity of LBaWO-2% as a function of logarithm pH_2O at 600 °C after deconvolution.

Fig,5.14 (a) shows that upon dehydration at 800 °C, the conductivity has a sudden increase then slowly decreases with time towards a saturation. Upon hydration, the conductivity relaxes in an opposite way, shown in Fig.5.14 (c) The conductivity first decreases fast and then increases slowly until saturation.

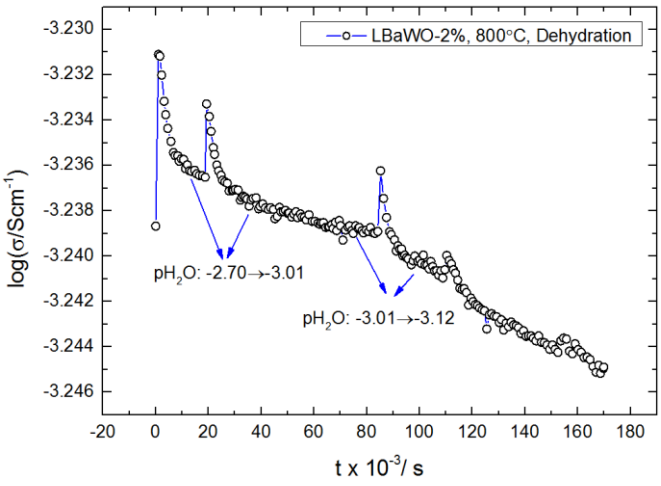

(a)

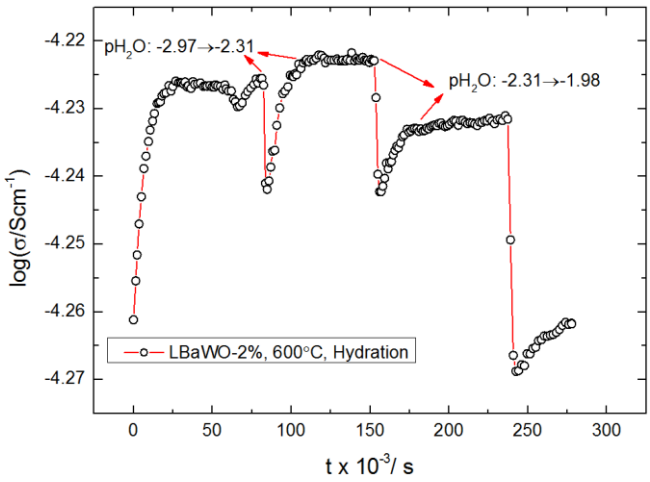

(b)

Fig.5.14 (a) Conductivity relaxation of LBaWO-2% upon dehydration at 800 °C. (b) Conductivity relaxation of LBaWO-2% upon hydration at 600 °C.

From Fig.5.15 (a), one realizes that pH_2O dependence of LBaWO-0.5% behaves differently from LBaWO-2%. Below 600 °C, dependence can clearly be seen, and it becomes more significant with decreasing temperature. pH_2O dependence at 400 °C approaches $\frac{1}{4.5}$. Fig.5.15 (b) is the pH_2O dependence for bulk of LBaWO-0.5%. The pH_2O dependence of bulk is similar as total conducitivty, except for the conductivity of bulk that goes higher than total conductivity at the temperature down to 600 °C.

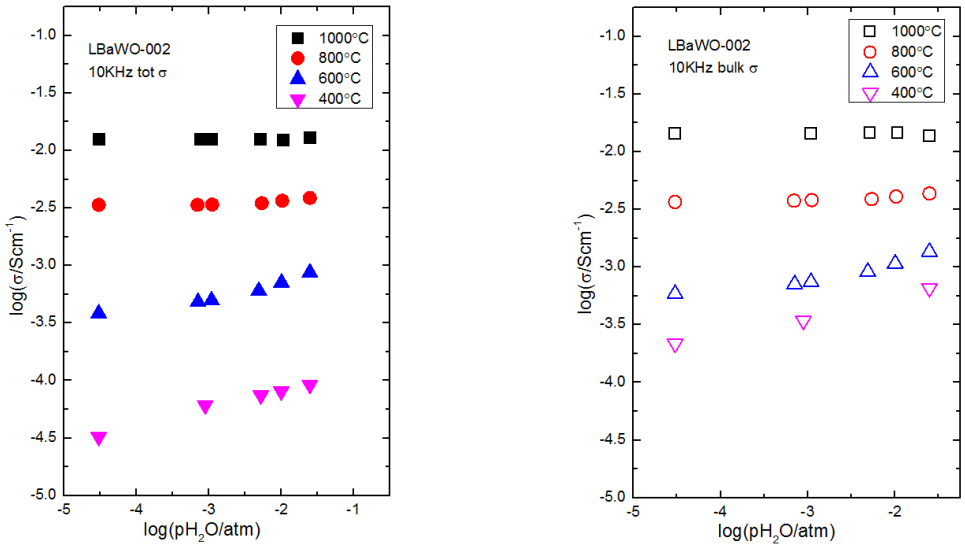

(a) (b)

Fig.5.15 Logarithm of conductivity of LBaWO-0.5% as a function of logarithm pH_2O from 400°C to 1000°C. (a) Total conductivity. (b) Bulk conductivity after deconvolution.

pH_2O dependence of LWO53[39] and LWO57[39] was plotted in Fig.5.16 to compare with the samples. It is clear that pH_2O for the total conductivity of LBaWO-0.5%, LWO53 and LWO57 at these two temperatures are similar. Although the bulk conductivity exists uncertianty, pH_2O dependence of the bulk conductivity of LBaWO-2% at 600 °C is also similar with the undoped ones.

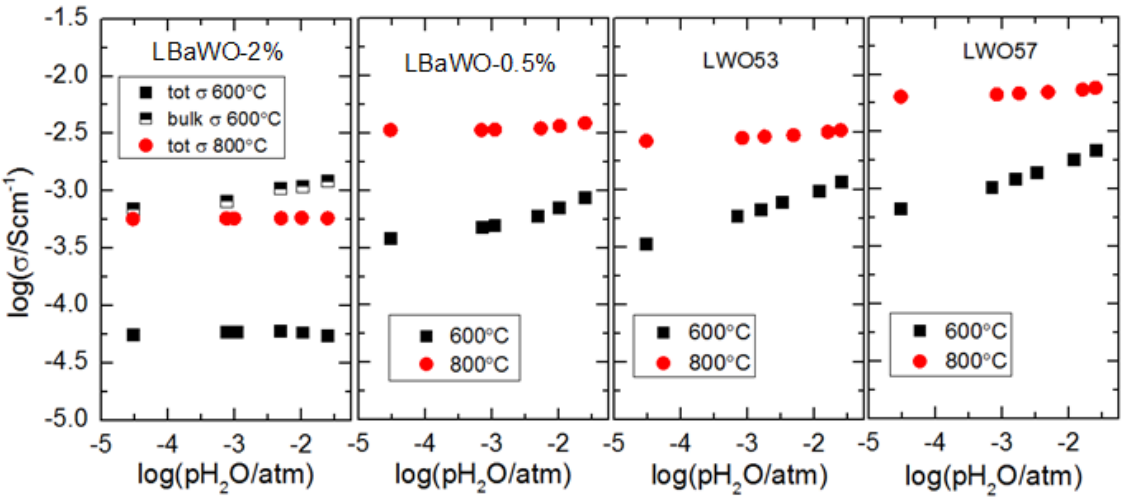

Fig.5.16 Logarithm of conductivity of different materials as a function of logarithm pH_2O at 600 °C and 800 °C. All the solid symbols represent the total conductivity and half open symbol is for bulk of LBaWO-2%

5.3. TG Results

Fig.5.17 displays the relative mass change of LBaWO-2% associated with a step wise decrease in temperature from 1100 °C to 300 °C in dry O_2 and wet O_2. From the raw data of Fig.5.17 (a), the mass change is only 0.024 mg, which means that there is essentially no water uptake under the dry condition. Under the wet O_2, there is 0.737 mg mass change. From Fig.5.17 (b), the water uptake happens quickly at 1100 °C and down to 600 °C, whereas below 600 °C the equilibrium increases. One may also notice that from 1100 °C and 600 °C, mass change seems not reach to equilibrium.

Fig.5.18 shows the thermogravimetric measurements of LBaWO-0.5% at the same atmosphere and temperature range as Fig.5.17. Fig.5.18 (a) indicates that there is no water uptake in dry O_2, whereas (b) indicates LBaWO-0.5% could be hydrated when

water is present. Mass change of LBaWO-0.5% under wet O_2 (1.446 mg) is almost doubled the one of LBaWO-2%. The sample powder used for thermogravimetric measurements of LBaWO-2% was nearly one half of LBaWO-0.5%, therefore, mass change for these two samples is reasonable.

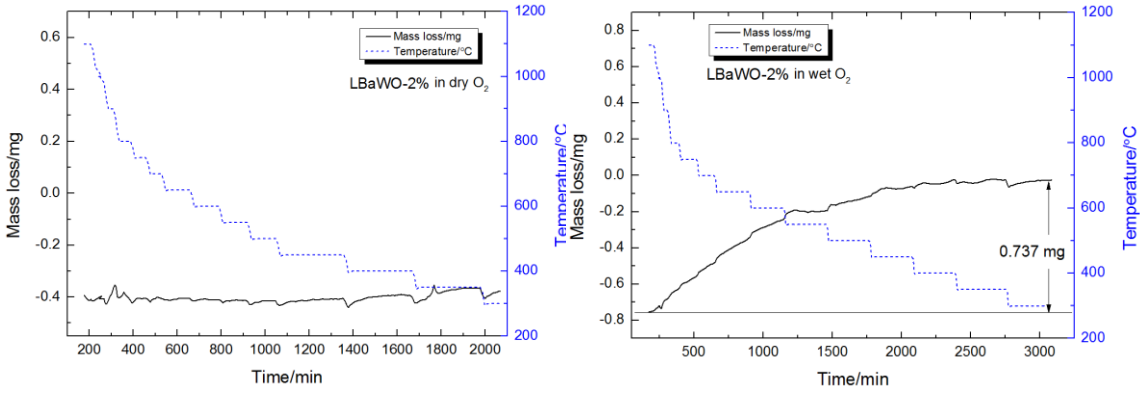

(a) (b)

Fig.5.17 The time-dependent mass change of LBaWO-2% taking place in response to the step wise temperature decrease. (a) in dry O_2. (b) in wet O_2.

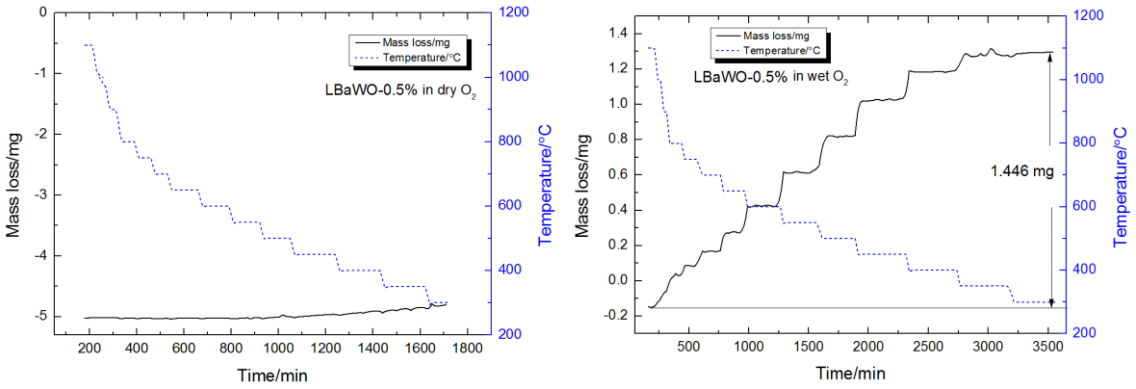

(a) (b)

Fig.5.18 The time-dependent mass change of LBaWO-0.5% taking place in response to the step wise temperature decrease. (a) in dry O_2. (b) in wet O_2

Hydration of LWO54 has not been studied yet by anyone. LWO54 has 0.5 mol inherent oxygen vacancies, which is less than LWO56 (0.73 mol oxygen vacancies) and higher than LWO53 (0.46 mol oxygen vacancies). I assume mol dissolved water per mol LWO54 be in the between of LWO56 and LWO53. With acceptor doping, higher hydration than undoped LWO54 would be expected. From Fig.5.19, both

samples are hydrated. Water uptake of LBaWO-0.5% goes between LWO57 and LWO53, closer to LWO53. As to LBaWO-2%, it shows bit lower water uptake than LBaWO-0.5%.

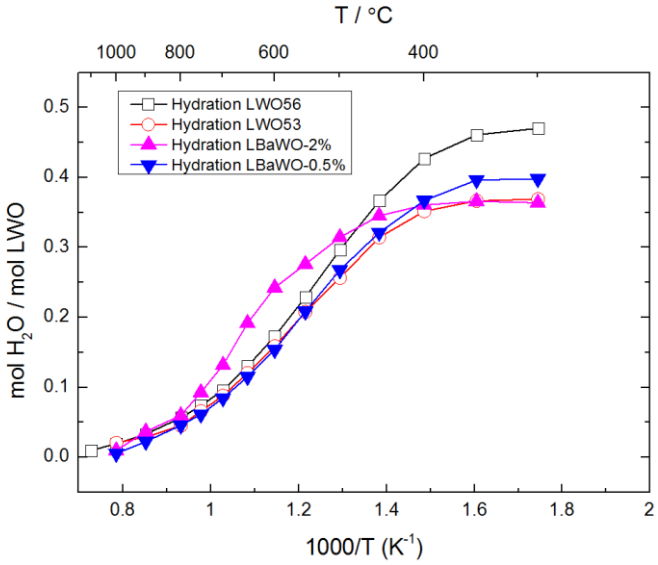

Fig.5.19 The water concentration of LBaWO-2%, LBaWO-0.5%, LWO53 and LWO57 as a function of inverse absolute temperature. All the data are recorded under oxidizing condition. Data of LWO56 and LWO is taken from[34].

6. Discussion

The main purpose of this chapter is to interpret the results presented in chapter 5, including structural properties, conductivities as a function of temperature, pO_2, pH_2O, and the materials hydration properties. Comparing with the undoped material, Ba acceptor doping does not change the properties as being expected. The measurements of 0.5% Ba-doped sample, LBaWO-0.5%, reveal a different behavior than LBaWO-2%. Possible explanations will be proposed by comparing the behavior of these two samples with the undoped materials and considering the effects of intrinsic defects, dopant and secondary phases.

6.1. LBaWO-0.5%

6.1.1. Phase composition

From the SEM micrograph in Fig.5.3, one may note that even when the Ba doping level is reduced from 2% to 0.5%, a Ba-rich phase still could be seen on the sample surface after sintering. Based on the results of EPMA analysis LBaWO-0.5% (cf.Fig.5.5 and Table 5.3), the solubility of Ba-doped in $La_{27}W_5O_{55.5}$ is ~0.4%. One may note that the atomic composition results from EPMA (cf. Table 5.3) showing that the ratio of La/W has changed to ~5.6 after Ba doping. (La here denotes La site and means La+Ba in this case. Henceforth all the La/W means site ratio.) W kicked out of the matrix could be one of the reasons for ratio change. Or the ratio actually still maintains ~5.4 or less, but together with La segregation (La/W≤5.4, together La segregation makes EPMA results show 5.6).

6.1.2. Thermogravimetry (TG)

0.4 mol oxygen vacancies per formula unit were hydrated for LBaWO-0.5% and the amount of water uptake is higher than LWO53 (fully hydrated)[34] and lower than LWO56 (66% hydrated)[34]. LBaWO-0.5% (La/W=5.4 x=1) contains 0.5 mol inherent oxygen vacancies per formula unit. Assuming that 0.4% Ba acceptors are

successfully substituted on the La site according to the solubility discussed before, then, 0.108 mol oxygen vacancies per formula unit would be introduced. Therefore, material contains 0.608 mol oxygen vacancies per formula unit, including both intrinsic and extrinsic part. Thus, for LBaWO-0.5%, 66% of theoretical oxygen vacancies are hydrated (0.4 out of 0.608 vacancies per formula unit). Based on the discussion in Chapter 6.1.1, the deviation from full hydration can have the following two explanations.

1. Hancke et al.[34] repored that the undoped LWO56 not being fully hydrated is attributed to LWO56 being metastable at moderate temperature; oxygen vacancies order and/or La_2O_3 precipitates. If the ratio of La/W does change to ~5.6, the explanations for LWO56 are also suitable for this case.

2. If the ratio of La/W is actually ~5.4 or less, but together with La segregation makes EPMA results show 5.6. With decreasing ratio of La/W, fewer oxygen vacancies are available being hydrated. Based on this speculation, the total oxygen vacancies in LBaWO-0.5% is not 0.608 mol, but fewer. Therefore, the amount of water uptake of LBaWO-0.5% is probably within expectation.

All in all, whether LBaWO-0.5% can have full hydration could not be known because what initiates the ratio change from 5.4 to 5.6 is not known.

6.1.3. Defects structure

The pO_2 and pH_2O dependence of the sample (Fig. 5.11-Fig.5.16) can be explained by the full electroneutrality condition

$$n + \left[Ba_{La}^{/}\right] + \frac{4}{56}\left[O_{\frac{54}{56}O}^{\frac{4}{56}/}\right] = \frac{108}{56}\left[v_{\frac{54}{56}O}^{\frac{108}{56}\bullet}\right] + \frac{52}{56}\left[OH_{\frac{54}{56}O}^{\frac{52}{56}\bullet}\right] + 3[W_{La}^{\bullet\bullet\bullet}] + p \qquad (6.1)$$

At 1100 °C, the conductivity of LBaWO-0.5% exhibits a weak dependence under oxidizing condition (cf. Fig.5.12), corresponding to the right part of the Brouwer diagram (cf.Fig.2.2). In this region, $\frac{4}{56}\left[O_{\frac{54}{56}O}^{\frac{4}{56}/}\right] = \frac{108}{56}\left[v_{\frac{54}{56}O}^{\frac{108}{56}\bullet}\right] + p$, electron holes are

regarded as a minority defect. The pO_2 dependence at this temperature indicates that p-type conductivity has a contribution due to the high mobility of electronic species at high temperature and it exhibits a mixed p-type and oxygen ion conductivity. At the same temperature, under reducing condition, the conductivity of this material exhibits slightly stronger pO_2 dependence (cf. Fig.5.12), corresponding to the left region of Brouwer diagram (cf. Fig.2.3). Here, $\frac{4}{56}\left[O_{\frac{54}{56}O}^{\frac{4}{56}/}\right] + n = \frac{108}{56}\left[v_{\frac{54}{56}O}^{\frac{108}{56}\bullet}\right]$. Similar to the oxidizing condition, electrons as a minority defect have a contribution to the conductivity and it exhibits a mixed n-type and oxygen ion conductivity. Inherent donor $W_{La}^{\bullet\bullet\bullet}$ increases the concentration of electrons and gives rise to the n-type conductivity.

The conductivity of LBaWO-0.5% exhibits pH_2O dependence below ~600 °C and the dependence gets stronger with decreasing temperature as shown in Fig.5.15. Above 600 °C, the conductivity becomes independent of pH_2O, which shows that the material is essentially dehydrated at higher temperature. The conductivities approach $pH_2O^{\frac{1}{4}}$ at the highest level of pH_2O at 400 °C, a weaker dependence than $pH_2O^{\frac{1}{2}}$ corresponding to the Brouwer diagram (cf. Fig.2.4).

6.1.4. Effect of Ba acceptor doping

From Eq.(2.10) and (2.11), one may expect that the oxide ion and proton conductivity increase upon acceptor doping. From Fig.5.10, the bulk conductivity of LBaWO-0.5% shows a slightly higher conductivity than undoped LWO54[39] below ~600 °C. Before discussing the conductivity, several statements need to be made. First the bulk conductivity of LBaWO-0.5% has uncertainties due to the deconvolution. Second, the total conductivity of the undoped materials measured under reducing condition are compared with bulk conductivity of the sample measured under oxidizing conduction. Although as previously mentioned, it is reliable to compare them, difference exists. The conductivity of the LBaWO-0.5% is similar as for the undoped ones.

One may note that the ratio La/W has changed from 5.4 to 5.6 after doping, which could lead an effect on the conductivity. With Ba doping, tungsten might be kicked

out from the structure. The concentration of oxygen vacancies will increase with the increasing ratio of La/W, it can thus give a relatively higher ionic conductivity. By comparing the data with undoped LWO57[39] (cf.Fig.5.10), one may notice that the bulk conductivity has a trend close to LWO57 at low temperature.

To account for the proton conductivity not increasing as predicted, explanations from two parts will be given. First, based on the intrinsic and extrinsic oxygen vacancies calculated in Chapter 6.1.2, the relative number of oxygen vacancies as a consequence of the acceptor doping is few compared to the intrinsic ones. Therefore, it could be essentially unaffected.

Second, the acceptor might either decrease the concentration of proton or decrease their mobility. The sample not being fully hydrated (cf.Chapter 6.1.2) could be the explanation from the concentration side. Another feasible reason could be that acceptor traps protons, forming $Ba_{La}^{/} \cdot OH_O^{\bullet}$, decreasing the mobility of protons. In proton conductors, acceptor trapping oxygen vacancies, forming $Ba_{La}^{/} \cdot v_O^{\bullet\bullet}$ might also have an indirect effect. Trapping will slow down the mobility of oxygen vacancies to migrate to the surface of the sample and take part in the hydration reaction.

Fig.6.1 shows the pO_2 dependence of undoped LWO53, LWO54 and LWO56[39]. By comparing them with LBaWO-0.5%, one may find that the behavior of the sample is closer to LWO53, which has the highest concentration of $W_{La}^{\bullet\bullet\bullet}$ of these three undoped material. Comparing with undoped LWO54 and LWO56, LBaWO-0.5% shows lower ionic conductivity and more n-type conductivity in the reducing region. From the electroneutrality of LWO, $3[W_{La}^{\bullet\bullet\bullet}] + \frac{108}{56}\left[v_{\frac{54}{56}O}^{\frac{108}{56}\bullet}\right] \cong \frac{4}{56}\left[O_{\frac{54}{56}O}^{\frac{4}{56}/}\right]$ (assuming that electron and electron hole concentration is negligible), one can tell that the lower ratio of La/W means more tungsten, which leads to a lower concentration of oxygen vacancies. The conductivity at intermediate pO_2 – where it is essentially pO_2 independent, decreases with increasing tungsten concentration due to this effect. Furthermore, the pO_2 dependence at the highest temperature of LWO53 shows n-type conductivity due to more tungsten[13]. Therefore, it is speculated that more inherent donor $W_{La}^{\bullet\bullet\bullet}$ formed with Ba doping. In the discussion of TG results, we talked that, in one case, it is possible to form more $W_{La}^{\bullet\bullet\bullet}$.

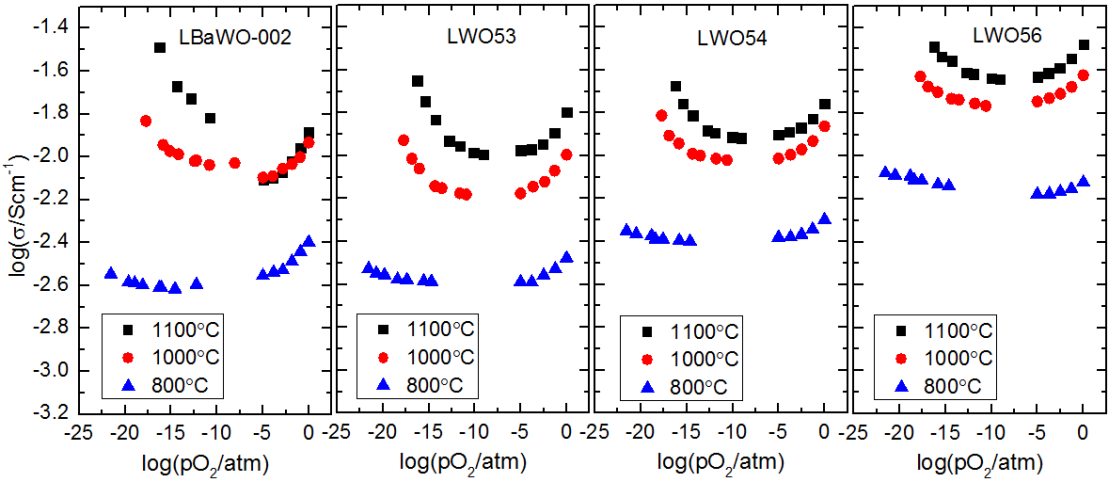

Fig.6.1 Logarithm of total conductivity as a function of logarithm pO_2 at 1100 °C, 1000 °C and 800 °C. The results of LWO53, LWO54 and LWO56 are taken from reference[13].

6.1.5. Curve fitting

The dominating electroneutrality could be given as

$$\left[Acc'\right] = \frac{108}{56}\left[v_{\frac{54}{56}O}^{\frac{108}{56}\bullet}\right] + \frac{52}{56}\left[OH_{\frac{54}{56}O}^{\frac{52}{56}\bullet}\right] \tag{6.2}$$

Here, Acc' is the effective acceptor level, and, it includes the effect from $Ba_{La}^{/}$, $W_{La}^{\bullet\bullet\bullet}$ and $O_{\frac{54}{56}O}^{\frac{4}{56}/}$ in this case.

$$\left[Acc'\right] = \frac{4}{56}\left[O_{\frac{54}{56}O}^{\frac{4}{56}/}\right] + \left[Ba_{La}^{/}\right] - 3[W_{La}^{\bullet\bullet\bullet}] \tag{6.3}$$

Eq.(6.2) together with expression for hydration enthalpy (cf.Eq.(2.21)) and partial conductivity (cf.Eq.(2.27)) can be used as basis of curve fitting. Transport and thermodynamic parameter of the material can be extracted by fitting the conductivity and hydration with TableCurve 2D for Windows[40].

Fig.6.2 displays the total conductivity and partial conductivity of LBaWO-0.5%, at 10 kHz in wet O_2 from 300 °C to 1000 °C. It can be observed that proton conductivity

dominates below ~700 °C. Above ~800 °C, both ionic and electronic conductivity replace proton conductivity. Eventually, electronic conductivity will surpass ionic conductivity at the temperature up to ~1000 °C. The fitted data are in agreement with pO_2 and pH_2O of the conductivity.

The hydration thermodynamics and transport parameters of the different charge carriers in Table 6.1 are interpreted based on the most recent defect model for dissolution of protons, oxygen vacancies and electron holes in the structure of LWO. Standard enthalpy and entropy changes of hydration of LBaWO-0.5% are all in general agreement with the values from literature[34] ΔH^0_{hydr} ≈-90 kJ/mol and ΔS^0_{hydr}≈-115 J/mol K. Also, the enthalpy of mobility of protons is ~60 kJ/mol, which is in agreement with the value from reference[13]. Back to the acceptor trapping discussed in Chapter 6.1.4, since the concentration of acceptor is very low, the trapping could therefore be less.

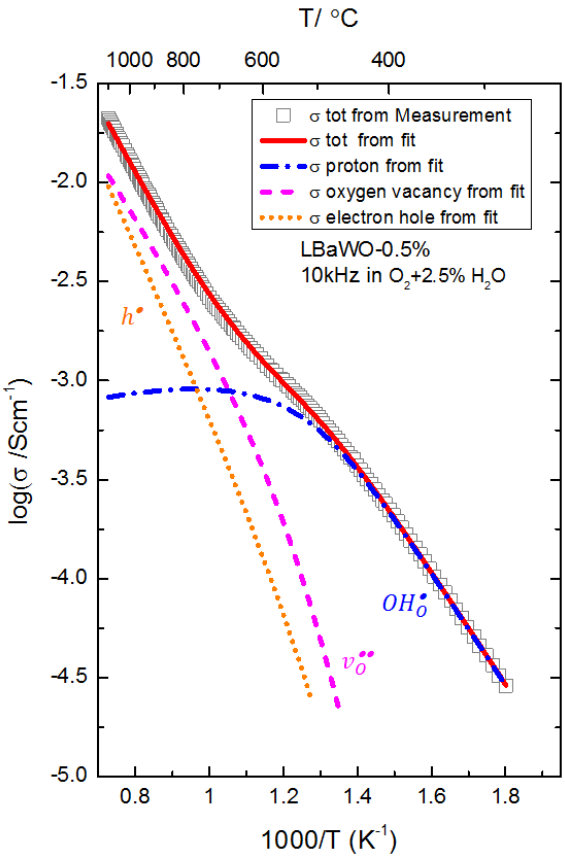

Fig.6.2 Logarithm of total conductivity and partial conductivity of LBaWO-0.5% as a function of the inverse absolute temperature from 300 °C to 1000 °C in O_2-0.025 H_2O atm.

Table 6.1 Summary of thermodynamic and transport parameters extracted from the modeled results LBaWO-0.5%.

			LBaWO-0.5%
	[Acc/]		~0.70
$OH_O^\bullet$	H_{hydr}^0	kJ/mol	~-105
	ΔS_{hydr}^0	J/molK	~-125
	$u_{OH_O^\bullet}^0$	cm^2K/Vs	~80
	$\Delta H_{OH_O^\bullet}$	kJ/mol	~60
$v_O^{\bullet\bullet}$	$u_{v_O^{\bullet\bullet}}^0$	cm^2K/Vs	~175
	$\Delta H_{v_O^{\bullet\bullet}}$	kJ/mol	~65
$h^\bullet$	$K_o^{1/2}u_{h^\bullet}^0$		~530
	$E_{a,h^\bullet}$	kJ/mol	~90

The concentration of dissolved $OH_O^\bullet$ can be derived from the concentration of dissolved water which is calculated from TG results in Fig.5.17 (b) above. According to Hancke et al.[34].

$$C_{H_2O} = \frac{\Delta m}{M_{H_2O}} \cdot \frac{M_{LBaWO-00x}}{m_{LBaWO-00x}} \tag{6.4}$$

Here, Δm is the mass change which indicated the mass of water uptake and $[OH_O^\bullet]$ =2 C_{H_2O}. By combining the expression for the concentration of proton (cf.Eq.(2.23)) and expression for hydration enthalpy (cf.Eq.(2.21)), the proton concentration of the sample could be modeled. $[OH_O^\bullet]$ of two samples is plotted as a function of inverse absolute temperature in Fig.5.19, $[OH_O^\bullet]$ increase upon decreasing temperature, eventually reaching saturation. The standard enthalpy and entropy of hydration can be calculated by curve fitting based on the defect model of proton dissolution, yielding for LBaWO-0.5%, ΔS_{hydr}^0≈-125 J/molK, ΔH_{hydr}^0≈-100 kJ/mol. Both are in general agreement with values from fitting condcutivity data and more negative than the undoped one.

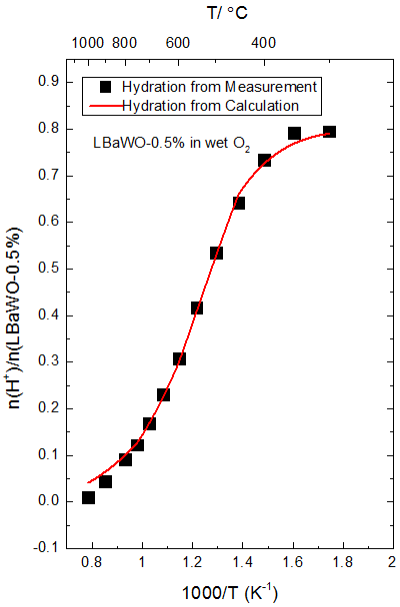

Fig.6.3 measured proton concentration and best fit to the model as a function of inverse absolute temperature for LBaWO-0.5%.

Table 6.2 Summary of thermodynamic parameters extracted from the modeled results of LBaWO-0.5%.

		LBaWO-0.5%
[Acc$^{/}$]		~0.75
ΔS^0_{hydr}	J/molK	~-125
ΔH^0_{hydr}	kJ/mol	~-100

6.2. LBaWO-2%

6.2.1. Phase composition

From EPMA results (cf.Fig.5.5 and Table 5.2), the LBaWO-2% matrix is complex due to the presence of secondary phases. One question immediately arises from this light grey phase (Ba/(La+Ba)≈6.8%, La/W≈5.0): does it have a different structure than the LWO, or is it the same structure, but with a different ratio of La/W, and/or affected by impurities? In order to make it simple, the dark grey part (~0.3% Ba-doped on La site, La/W≈5.6-5.7) is called phases1 and the light grey part is called phase2.

In order to distinguish the contribution of these two phases, let's first disregard the contribution from phase2 and regard phase1 as the only one involved. Thus, 0.37 mol water uptake per formula unit of LBaWO-2% (cf.Fig.5.19) was only led by the oxygen vacancies in phase1. From Fig.5.5, each phase takes up half of the whole sample. Therefore, I assume that half of the sample results in this 0.37 mol water uptake. By calculation the hydration according to Chapter 6.1.4 discussed, I got [$Acc^{/}$] =~1.3 mol. It means that in order to gain 0.37 mol water only initiated by phase1, 0.66 mol oxygen vacancies should be hydrated, and it further indicates that phase1 will be 108% hydrated (0.66 out of 0.608 vacancies per formula unit), which is impossible. Still can we not tell what phase2 exactly is, but phase2 must be a phase which has oxygen vacancies and could be hydrated, even if it could just be a secondary phase with different structure than LWO.

From Fig.5.10, the bulk conductivity of this sample behaves similar to undoped LWO. Combining this fact and the conclusion previously got, phase2 is believed to be the one with the same structure as LWO. These two phases are too complex to be distinguished due to the lack of data. However, one thing is accurate that impurities exist in the sample and have significantly influence.

Moreover, there is ~0.3% Ba resident in La site in phase1, which is almost in agreement with the solubility (~0.4%) we discussed in chapter 6.1.1.

6.2.2. Thermogravimetry (TG)

0.37 mol oxygen vacancies per formula unit were hydrated for LBaWO-2% (cf. Fig.5.19) which is lower than the hydration of LBaWO-0.5%, LWO56 and close to LWO53. As discussed in Chapter 6.1.2, the concentration of oxygen vacancies is 0.608 mol per formula unit with 0.4% Ba-doped. 61% of theoretical oxygen vacancies are hydrated (0.37 out of 0.608 vacancies per formula unit). Since in phase1, the ratio of La/W changed to ~5.6, the same as LBaWO-0.5%, the discussion for the hydration properties of LBaWO-0.5% could also be applicable here. The hydration of Ba-doped LWO with different doping level is observed to be similar.

6.2.3. Defects structure

Since the electrical behavior of LBaWO-2% is complicated due to high resistive grain boundary, it is necessary to emphasis and conclude the phenomenon here. First, the grain boundary has very low conductivity and shows no sign of proton effect at low temperature. However the values for the bulk conductivity deconvoluted from impedance data are similar to the undoped material (cf.Fig.5.10). Second, both grain boundary and bulk conductivity have pO_2 dependence, and the dependence is comparable with undoped materials. Last, grain boundary is independent of pH2O, whereas, grain may have dependence (cf.Fig.5.13).

For bulk, the conductivity has a similar behavior as LBaWO-0.5%.

For grain boundary, several speculations will be brought forward.

1. Blocking impurity phases at the grain boundaries (cf.Fig.5.5) could contribute to the high grain boundary resistance.

2. A large amount of Ba accumulating in phase2 may explain the relative enrichment of grain boundaries with acceptor dopant, which could serve as traps for protons and oxygen vacancies, and thus decreasing grain boundary conductivity.

3. Electronic conductivity may dominate grain boundaries. The full electroneutrality in oxidizing condition could be written as

$$\left[Acc'\right] = \frac{108}{56}\left[v_{\frac{54}{56}O}^{\frac{108}{56}\bullet}\right] + \frac{52}{56}\left[OH_{\frac{54}{56}O}^{\frac{52}{56}\bullet}\right] + p \qquad (6.5)$$

With electron holes dominating, the electroneutrality in grain boundary could be simplified as $\left[Acc'\right]$ = p=constant. Grain boundary in wet oxygen having almost the same conductivity as in dry oxygen (cf.Fig.5.9(a)) is in agreement with this possibility.

This speculation could also be proved from the pH_2O dependence (cf. Fig.5.13(a)). Below 600 °C, with oxygen vacancies being hydrated, the concentration of electron holes decreases with increasing proton concentration. Therefore, the grain boundary

conductivity will decrease with increasing pH_2O at relatively low temperature if electron holes are predominating charge carriers in grain boundary.

Moreover, conductivity relaxation of LBaWO-2% grain boundary (cf.Fig.5.14) may indicate electron holes as predominating charge carriers from the other side. According to Yoo et al[41, 42], hydration or dehydration proceeds through decoupled ambipolar diffusion of $H_i^{\bullet}$ and $h^{\bullet}$ and of $v_O^{\bullet\bullet}$ and $h^{\bullet}$.

Take hydration as an example, in-diffusion of H first consumes the concentration of electron holes, via

$$H + h^{\bullet} = H_i^{\bullet} \tag{6.6}$$

Then in-diffusion of O creates the concentration of electron holes, via

$$O + v_O^{\bullet\bullet} = O_O^{\bullet} + 2h^{\bullet} \tag{6.7}$$

Yoo et al[41, 42] interpreted that this non-monotonic, twofold relaxation of conductivity happened due to the fast chemical diffusion of H and sluggish chemical diffusion of O. Therefore, in the case of electron holes dominating, the phenomenon of Fig.5.15 could be observed.

4. Combining the impedance spectra shown in Fig.5.6, one may also think that the appearance of positively charged grain boundary and leading to Schottky barriers and the depletion of proton in grain boundary could also be a feasible possibility.

6.2.4. Effect of Ba acceptor doping

From Fig.5.10, the bulk conductivity of LBaWO-2% shows the similar behavior as the undoped ones and LBaWO-0.5%, which indicates that Ba doping does not change the properties much.

6.2.5. Curve fitting

Curving fitting for the total conductivity and bulk conductivity of LBaWO-2% as a function of inverse temperature bases on the same model talked in Chapter 6.1.5, which was used to fit the conductivity of LBaWO-0.5%.

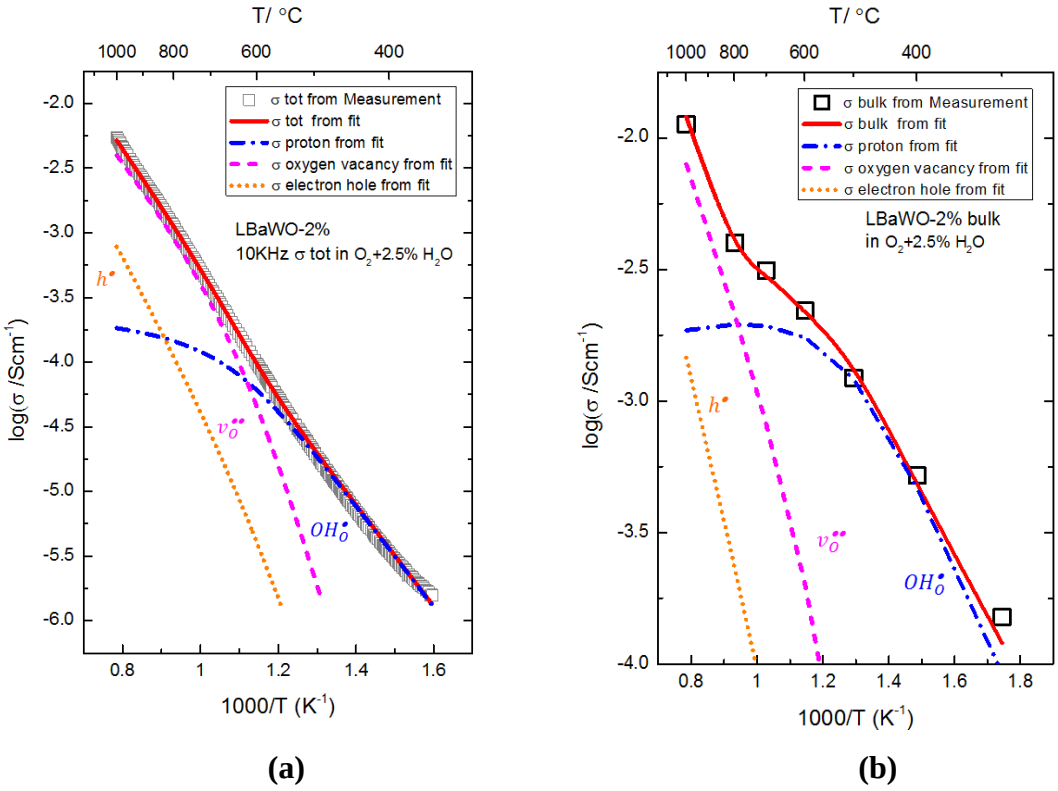

Fig.6.4 Logarithm of conductivity and partial conductivity as a function of the inverse absolute temperature from 300 °C to 1000 °C in O_2-0.025H_2O atm. (a) tot conductivity of LBaWO-2%, (b) bulk conductivity of LBaWO-2%.

Fig.6.4 (a) displays the total conductivity and partial conductivity at 10 kHz in wet O_2. The total conductivity here is dominated by grain boundary conductivity. Protons dominate below ~550 °C, then, oxygen vacancies continue to be the dominating charge carrier at the temperature above ~600 °C. Oxygen vacancies all the time show higher conductivity than electron holes. Fig.6.4 (b) is based on the bulk conductivity obtained from deconvolution with uncertainty. Therefore, it will not be discussed in detail here. However, from fitting transport and thermodynamic parameters were

extracted and shown in Table 6.3. One may note that the enthalpy of proton mobility in grain boundary is much higher than the one in bulk interior.

Table 6.3 Summary of thermodynamic and transport parameters extracted from the modeled results LBaWO-2%.

			LBaWO-2% total	LBaWO-2% bulk
	[Acc/]		~0.65	~0.70
$OH_O^{\bullet}$	H_{hydr}^0	kJ/mol	~-130	~-105
	ΔS_{hydr}^0	J/molK	~-135	~-130
	$u_{OH_O^{\bullet}}^0$	cm^2K/Vs	~60	~150
	$\Delta H_{OH_O^{\bullet}}$	kJ/mol	~80	~60
$v_O^{\bullet\bullet}$	$u_{v_O^{\bullet\bullet}}^0$	cm^2K/Vs	~350	~500
	$\Delta H_{v_O^{\bullet\bullet}}$	kJ/mol	~80	~75
$h^{\bullet}$	$K_o^{1/2}u_{h^{\bullet}}^0$		~2600	~1200
	$E_{a,h^{\bullet}}$	kJ/mol	~120	~110

The standard enthalpy and entropy of hydration of LBaWO-0.5% was yielded, ΔS_{hydr}^0 ≈ -125 J/molK, ΔH_{hydr}^0 ≈ -140 kJ/mol. Both are in general agreement with values from fitting condcutivity data and more negative than the undoped one. Compare with 0.5% Ba-doped material, the hydration enthalpy gets more negatvie with increasing doping level.

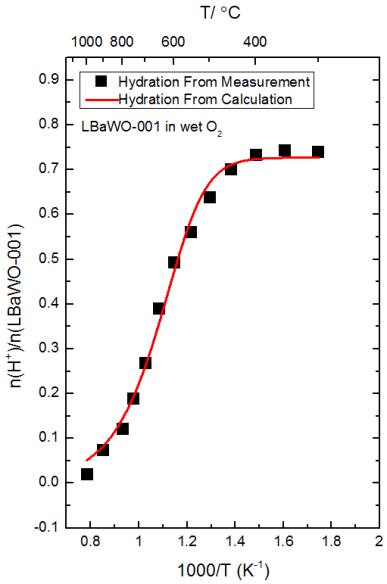

Fig.6.5 measured proton concentration and best fit to the model as a function of inverse absolute temperature for LBaWO-2%

Table 6.4 Summary of thermodynamic parameters extracted from the modeled results of LBaWO-2%.

		LBaWO-2%
[$Acc^{/}$]		~0.68
ΔS^0_{hydr}	J/mol K	~-140
ΔH^0_{hydr}	KJ/mol	~-125

6.3. Further Work

First of all, since the phases in LBaWO-2% are not completely determined, the extension of this study would include the structure investigation. For LBaWO-0.5%, it is necessary to study what initiates the ratio change of La/W, whether it has La_2O_3 precipitation. Transmission electron microscopy (TEM) or XRD Rietveld refinement could be carried out.

Secondly, through the work being done in this thesis, lanthanum tungstates with Ba doping is suspected to have an inherent space charge layer due to the high resistive

grain boundary. Transmission electron microscopy (TEM) should be carried out to investigate the purity of the sample, especially to the grain boundary.

Thirdly, the pO_2 dependence of LBaWO-2% under reducing condition could be studied to check how inherent donor $W_{La}^{\bullet\bullet\bullet}$ affects the pO_2 dependence.

7. Conclutions

Based on the characterization results from SEM and EPMA and together with the analysis from the experiments, the solubility of Ba dissolving in the LWO structure is around 0.4%. With Ba doping, the ratio change of La/W will be observed, from 5.4 to 5.6. Either tungsten is kicked out of the matrix with Ba doping, either the ratio still maintains 5.4 or less, but together with La segregation.

The grain boundary of both samples shows huge resistance and the resistance increases with increasing doping level. It could be attributed to highly resistive and blocking impurities in the grain boundaries or the inherent space charge layer depleting the positively charged species.

For LBaWO-0.5%, proton conductivity dominates blow ~700 °C, with the maximum proton conductivity being $2.3 \cdot 10^{-3}$ Scm^{-1} at 700 °C. At high temperature, the material exhibits n-type and p-type electronic conductivity under reducing and oxidizing condition respectively. The effect of acceptor doping from electrical measurements could nearly be observed.

Thermogravimetry was employed to study the hydration properties of the material. With Ba doping, no significant change of water uptake was observed. The thermodynamic parameters are in agreement with the literature. Standard hydration enthalpy and entropy get more negative with increasing doping level.

8. References

1. Shafiee, S. and E. Topal, *When will fossil fuel reserves be diminished?* Energy Policy, 2009. **37**(1): p. 181-189.
2. Agent, I.E., *CO2 EMISSIONS FROM FUEL COMBUSTION Highlights.* 2012.
3. Agent, I.E., *Key World Energy Statistics* 2012.
4. Lefebvre-Joud, F.G., Gilles; Mougin, Julie, *Current status of proton-conducting solid oxide fuel cells development.* Journal of Applied Electrochemistry, Apr 2009. **39**(4): p. 535.
5. NYMAN, J., *Proton conductivity of lanthanum and barium zirconate.* Department of Applied Physics, CHALMERS UNIVERSITY OF TECHNOLOGY, 2012.
6. Haugsrud, R., *Defects and transport properties in Ln6WO12 (Ln = La, Nd, Gd, Er).* Solid State Ionics, 2007. **178**(7–10): p. 555-560.
7. Haugsrud, R. and C. Kjølseth, *Effects of protons and acceptor substitution on the electrical conductivity of La6WO12.* Journal of Physics and Chemistry of Solids, 2008. **69**(7): p. 1758-1765.
8. Haugsrud, R. and T. Norby, *Proton conduction in rare-earth ortho-niobates and ortho-tantalates.* Nat Mater, 2006. **5**(3): p. 193-196.
9. Shimura, T., S. Fujimoto, and H. Iwahara, *Proton conduction in non-perovskite-type oxides at elevated temperatures.* Solid State Ionics, 2001. **143**(1): p. 117-123.
10. Kofstad, P.a.T.N., *Defects and transport in crystalline solids - Compendium for the advanced level course: Defect Chemistry and Reactions KJM5120.* 2012: University of Oslo.
11. Norby, T., *Electrical Measurements. Compendium for the advanced level course: Experimental methods KJM-MENA4010 Module 2.* 2011: University of Oslo.
12. Norby, T., *A Kröger-Vink Compatible Notation for Defects in Inherently Defective Sublattices.* The Korean Ceramic Society, 2010. **47**(1): p. 19-25.
13. Erdal, S., et al., *Defect structure and its nomenclature for mixed conducting lanthanum tungstates La28–xW4+xO54+3x/2.* International Journal of Hydrogen Energy, 2012. **37**(9): p. 8051-8055.
14. Haile, S.M., G. Staneff, and K.H. Ryu, *Non-stoichiometry, grain boundary transport and chemical stability of proton conducting perovskites.* Journal of Materials Science, 2001. **36**(5): p. 1149-1160.
15. Fjeld, H., *Ionic Transport in Atomic and Nanodimensional Structures in Oxides*. 2010: Department of Chemistry, Faculty of Mathematics and Natural Sciences, University of Oslo.
16. Sossina M. Haile, D.L.W.a.J.C., *The role of microstructure and processing on the proton conducting properties of gadolinium-doped barium cerate.* Journal of Materials Research, 1998. **13**(pp): p. 1576-1595.
17. Guo, X., et al., *Role of space charge in the grain boundary blocking effect in doped zirconia.* Solid State Ionics, 2002. **154–155**(0): p. 555-561.
18. Guo, X., W. Sigle, and J. Maier, *Blocking Grain Boundaries in Yttria-Doped and Undoped Ceria Ceramics of High Purity.* Journal of the American Ceramic Society, 2003. **86**(1): p. 77-87.

19. Kjølseth, C., et al., *Space–charge theory applied to the grain boundary impedance of proton conducting BaZr0.9Y0.1O3 − δ.* Solid State Ionics, 2010. **181**(5–7): p. 268-275.
20. Yoshimura, M. and J.F. Baumard, *Electrical conductivity of solid solutions in the system CeO2□La6WO12.* Materials Research Bulletin, 1975. **10**(9): p. 983-988.
21. Magraso, A., et al., *Complete structural model for lanthanum tungstate: a chemically stable high temperature proton conductor by means of intrinsic defects.* Journal of Materials Chemistry, 2012. **22**(5): p. 1762-1764.
22. Iwahara, H., et al., *Proton conduction in sintered oxides and its application to steam electrolysis for hydrogen production.* Solid State Ionics, 1981. **3–4**(0): p. 359-363.
23. Iwahara, H., H. Uchida, and S. Tanaka, *High temperature type proton conductor based on SrCeO3 and its application to solid electrolyte fuel cells.* Solid State Ionics, 1983. **9–10, Part 2**(0): p. 1021-1025.
24. Iwahara, H., *Proton Conduction in Sintered Oxides Based on BaCeO3.* J. Electrochem. Soc. , 1988. **135**(2): p. 529-533.
25. Norby, T. and Y. Larring, *Concentration and transport of protons in oxides.* Current Opinion in Solid State and Materials Science, 1997. **2**(5): p. 593-599.
26. Kreuer, K.D., *PROTON-CONDUCTING OXIDES.* Annual Review of Materials Research, 2003. **33**(1): p. 333-359.
27. Duval, S.B.C., et al., *Electrical conductivity of the proton conductor BaZr0.9Y0.1O3−δ obtained by high temperature annealing.* Solid State Ionics, 2007. **178**(25–26): p. 1437-1441.
28. P. Babilo, T.U., and S. M. Haile, *Processing of Yttrium-Doped Barium Zirconate for High Proton Conductivity.* Journal of Materials Research, 2007. **22**(5): p. 15.
29. Aleshin, E. and R. Roy, *Crystal Chemistry of Pyrochlore.* Journal of the American Ceramic Society, 1962. **45**(1): p. 18-25.
30. Chang, L.L.Y. and B. Phillips, *Samarium and Lanthanum Tungstates of the 3R2O3.WO3 Type.* Inorganic Chemistry, 1964. **3**(12): p. 1792-1794.
31. Diot, N., et al., *Rare-earth and tungsten oxynitrides with a defect fluorite-type structure as new pigments.* Journal of Alloys and Compounds, 2001. **323–324**(0): p. 45-48.
32. G.J. McCarthy, R.D.F., G.G. Johnson Jr., C.E. Gooden, *Proceedings of the 5th Materials Research Symposium.* Solid State Chemistry, 1972: p. 397.
33. Magraso, A., et al., *New crystal structure and characterization of lanthanum tungstate "La6WO12" prepared by freeze-drying synthesis.* Dalton Trans, 2009(46): p. 10273-83.
34. Hancke, R., et al., *Hydration of lanthanum tungstate (La/W = 5.6 and 5.3) studied by TG and simultaneous TG–DSC.* Solid State Ionics, 2013. **231**(0): p. 25-29.
35. *NorECs AS. Webside.* http://www.norecs.com/probostat.htm. May 2013.
36. Løken, A., *Thermodynamics and transport of defects in Sc-doped CaSnO3 and CaZrO3.* 2011: Department of Chemistry, Faculty of Mathematics and Natural Sciences, University of Oslo.
37. *Simultaneous Thermal Analysis Method, Tchnique, Applications, NETZSCH, 2012.*
38. Herve, C., *Unpublished.*
39. Magraso, A., *unpublished.*

40. Boukamp, B.A., *Equivalent circuit for Windows, version 1.2.* 2008: University of Twente.
41. Yoo, H.I., et al., *Hydration and oxidation kinetics of a proton conductor oxide, SrCe(0.95)Yb(0.05)O(2.975).* Phys Chem Chem Phys, 2008. **10**(7): p. 974-82.
42. Yoo, H.-I., J.I. Yeon, and J.-K. Kim, *Mass relaxation vs. electrical conductivity relaxation of a proton conducting oxide upon hydration and dehydration.* Solid State Ionics, 2009. **180**(28–31): p. 1443-1447.

9. Appendix

This appendix summarizes the defect equilibrium used to model the water uptake from TG and the conductivity as a function of temperature under oxidizing condition.

For the water uptake modeling, oxygen vacancies are hydrated through reaction Eq.(2.13). The electroneutrality condition is assumed:

$$\left[Acc^{/}\right] = \frac{52}{56}\left[OH_{\frac{54}{56}O}^{\frac{52}{56}\bullet}\right] + \frac{108}{56}\left[v_{\frac{54}{56}O}^{\frac{108}{56}\bullet}\right] \tag{9.1}$$

Here $Acc^{/}$ means an effective acceptor level.

And the hydration constant can be given as:

$$K_{hydr} = \frac{\left[OH_{\frac{54}{56}O}^{\frac{52}{56}\bullet}\right]^2}{\left[O_{\frac{54}{56}O}^{\frac{4}{56}/}\right]\left[v_{\frac{54}{56}O}^{\frac{108}{56}\bullet}\right]p_{H_2O}} = exp\left(\frac{\Delta S_{hydr}^0}{R}\right)exp\left(-\frac{\Delta H_{hydr}^0}{RT}\right) \tag{9.2}$$

Combing these expressions, the concentration of proton can be given as

$$\left[OH_{\frac{54}{56}O}^{\frac{52}{56}\bullet}\right] = \frac{13}{56}K_{hydr}\left[O_{\frac{54}{56}O}^{\frac{4}{56}/}\right]P_{H_2O}\left(-1+\sqrt{1+\frac{1512[Acc^{/}]}{169K_{hydr}\left[O_{\frac{54}{56}O}^{\frac{4}{56}/}\right]P_{H_2O}}}\right) \tag{9.3}$$

For the conductivity modeling, the partial conductivity of each species i reads:

$$\sigma_i = z_i e c_i \mu_i \tag{9.4}$$

where z_i is the number of charges on the species, e is the elementary charge and c_i is the concentration of charge carriers (cm^{-3}). However, the concentration of charge carriers could also be given in molar fraction, then, the conductivity can be given as:

$$\sigma_i = z_i e c_i \mu_i F \rho_m \tag{9.5}$$

where F is Faraday's constant and ρ_m is the molar density of the material (mol cm^{-3}).

The mobility of a charge carrier can be given as

$$\mu_i = \mu_{0,i}\frac{1}{T}\exp\left(-\frac{\Delta H_{m,i}}{RT}\right) \tag{9.5}$$

The concentration of oxygen vacancies can be evaluated to give the following expression:

$$\left[OH_{\frac{54}{56}O}^{\frac{52}{56}\bullet}\right] = \frac{56}{52}\left[Acc'\right] - \frac{108}{52}\left[v_{\frac{54}{56}O}^{\frac{108}{56}\bullet}\right] \tag{9.6}$$

Under oxidizing condition, the concentration of electron holes can be given through the equilibrium coefficient of oxidation reaction, Eq.(2.8)

$$P = \left(\frac{1}{27}K_O\right)^{\frac{1}{2}}\left[v_{\frac{54}{56}O}^{\frac{108}{56}\bullet}\right]^{\frac{1}{2}} {p_{O_2}}^{\frac{1}{4}} \tag{9.7}$$

The total conductivity as a function of temperature under oxidizing condition includes the contribution from protons, oxygen vacancies and electron holes. The transport parameters can be obtained from modeling the total conductivity. For proton, they are ΔS_{hydr}^0, ΔH_{hydr}^0, $u_{OH_O^\bullet}^0$ and $\Delta H_{OH_O^\bullet}$. For oxygen vacancies, they are $u_{v_O^{\bullet\bullet}}^0$ and $\Delta H_{v_O^{\bullet\bullet}}$. For electron holes, thery are A=$K_o^{1/2}u_{h^\bullet}^0$ and $E_{a,h^\bullet}$.